

Superparamagnetic iron-oxide based nanoparticles for the separation and recovery of precious metals from solution

Eugene Marlin Lakay



A thesis submitted to the

University of Stellenbosch

in fulfillment of the requirements for the degree of

Master of Science

Supervisor: Professor Klaus R. Koch

March 2009

Declaration

By submitting this dissertation electronically, I declare that the entirety of the work contained therein is my own, original work, that I am the owner of the copyright thereof (unless to the extent explicitly otherwise stated) and that I have not previously in its entirety or in part submitted it for obtaining any qualification.

Date: 4 March 2009

Copyright © 2009 Stellenbosch University

All rights reserved

*“Challenges are what makes life interesting, overcoming them is what makes
life meaningful”*

- Joshua J. Marine-

Acknowledgements:

I would sincerely like to thank:

- First of all I am indebted to my supervisor and mentor, Professor Klaus Koch for his guidance and support throughout this project and for believing in me.
- Drs Kathy Sole and Laura Vatta from Anglo American Research for their interest and input in my work.
- The staff of the Central Analytical Facility. To Riana Rossouw thank you for all your help and advice on ICP measurements. To Madelaine Frazenburg for help with SEM-EDX analysis and Matt Gordon for Elemental analysis.
- Mrs. Hanlie Botha for surface area analysis
- Mr. Mohammed Jaffer from UCT for stimulating discussions and TEM analysis
- For technical assistance and support thanks to Shafiek, Deidre, Lisinda and Roger
- The PGM research group members, thank you for creating a friendly environment to work in.
- Thanks to Liezel Retief and Dr. Astrid Buica for editing some parts of this thesis.
- To my parents, my sisters and brother for their invaluable support and prayers.
- The University of Stellenbosch, Anglo American Research and the NRF for financial assistance.

Abstract

The demand for gold, platinum and palladium continues to stimulate the development of cost effective and more efficient methods to recover these precious metals from aqueous acidic solutions. Towards this goal, we have successfully synthesized superparamagnetic magnetite nanoparticles (SPMNs) by co-precipitation of ferrous and ferric salts with ammonium hydroxide and coated them with tetraethyl orthosilicate to form well dispersed silica-coated SPMNs. Subsequently, the silica-coated SPMNs were then functionalized with amine methoxysilane ligands to yield magnetic ion-exchange materials with **(1)** monoamine and **(2)** ethylenediamine functionality. The superparamagnetic behavior of the SPMNs was confirmed by vibrating sample magnetometry and as such could be separated from the aqueous phase (phase separation) at room temperature under the influence of an external magnetic field (~ 0.35 T). X-ray diffraction patterns indicate that the SPMNs are of relatively high purity with an inverse spinel structure. The average sizes of the uncoated SPMNs and silica-coated SPMNs determined by transmission electron microscopy were found to be in the range of 4 – 15 nm and 60 – 80 nm, respectively. The surface area determined by BET analysis was found to be 160.28 ± 0.77 m²/g and 183 ± 0.53 m²/g for the uncoated SPMNs and the silica-coated SPMNs, respectively. With the aid of elemental analysis, the amount of amine methoxysilane ligands immobilized onto **(1)** and **(2)** was found to be 0.75 mmol/g and 0.87 mmol/g, respectively.

The removal of $[\text{AuCl}_4]^-$, $[\text{PdCl}_4]^{2-}$ and $[\text{PtCl}_4]^{2-}$ from aqueous solutions with materials **(1)** and **(2)** was investigated as a function of HCl concentration (0.01 M HCl – 0.5 M HCl), mass of material (10 – 50 mg), ionic strength (0 – 1.5 mol L⁻¹) and contact time. The amount of $[\text{AuCl}_4]^-$, $[\text{PdCl}_4]^{2-}$ and $[\text{PtCl}_4]^{2-}$ removal was found to increase with decreasing HCl concentration, decreasing ionic strength and increasing mass. As expected, it was found that **(2)** had a higher loading capacity than **(1)**. For materials **(1)** and **(2)** the maximum loading capacity of $[\text{AuCl}_4]^-$ was found to be 0.072 mmol/g (14.182 mg/g) and 0.111 mmol/g (21.863 mg/g), respectively. The adsorption data have been fitted with a non-competitive Langmuir isotherm model. It was found that the experimental data was in reasonable good agreement with the Langmuir model, suggesting monolayer $[\text{AuCl}_4]^-$ coverage. The rate of $[\text{AuCl}_4]^-$, $[\text{PdCl}_4]^{2-}$ and $[\text{PtCl}_4]^{2-}$ removal from 0.5 M HCl solutions by **(1)** and **(2)** was found to be very slow, but counter intuitively with a higher selectivity for $[\text{AuCl}_4]^-$. Eventually, 55% of $[\text{AuCl}_4]^-$ could be removed from solution by **(1)** and 96 % $[\text{AuCl}_4]^-$ by **(2)**. In addition, the affinity of $[\text{PdCl}_4]^{2-}$ and $[\text{PtCl}_4]^{2-}$ for **(1)** and **(2)** was low with only 11.9 % $[\text{PdCl}_4]^{2-}$ and 10.0 % $[\text{PtCl}_4]^{2-}$ removed from 0.5 M HCl solutions. However, the rate of $[\text{AuCl}_4]^-$, $[\text{PdCl}_4]^{2-}$ and $[\text{PtCl}_4]^{2-}$ removal was improved when conducting the

experiments in 0.01 M HCl solutions. It was found that the adsorption maxima was reached in less than 30 minutes and that 76.8 % $[\text{AuCl}_4]^-$, 95.9 % $[\text{PtCl}_4]^{2-}$ and 98.8 % $[\text{PdCl}_4]^{2-}$ could be removed from 0.01M HCl solutions. The differences in the rate of removal and the efficiency could be explained in terms of the competition between the anionic metal complexes and the counter chloride ions for the available protonated sites on the ion-exchangers **(1)** and **(2)**.

In contrast to the slow kinetics of adsorption for $[\text{AuCl}_4]^-$ using **(1)** and **(2)**, uncoated SPMNs exhibit high $[\text{AuCl}_4]^-$ removal efficiency with a relatively good rate of removal. It was found that $[\text{AuCl}_4]^-$ could be quantitatively adsorbed by the uncoated SPMNs. Furthermore, it was found that $[\text{PdCl}_4]^{2-}$ and $[\text{PtCl}_4]^{2-}$ removal from aqueous solutions using the SPMNs strongly depends on the molarity of the solutions, showing improved adsorption efficiency with increasing HCl concentration from 0.01 M to 0.5 M HCl. The difference in recovery behavior of $[\text{AuCl}_4]^-$ as compared to $[\text{PdCl}_4]^{2-}$ and $[\text{PtCl}_4]^{2-}$ using uncoated SPMNs, suggested that two different mechanisms are responsible for the removal of the precious metal species from solution and adsorption onto the SPMNs. We report that $[\text{PdCl}_4]^{2-}$ and $[\text{PtCl}_4]^{2-}$ was removed from the aqueous solutions by the SPMNs *via* electrostatic interaction and that $[\text{AuCl}_4]^-$ was removed from the aqueous solutions *via* a reduction-adsorption mechanism.

Uittreksel

Die aanvraag op goud, platinum en palladium gaan voort om die ontwikkeling van meer ekonomiese en effektiewe metodes om hierdie waardevolle metale te herwin uit suur oplossings. In hierdie konteks, het ons superparamagnetiese magnetiet nanoparticles (SPMNs) suksesvol gesintetiseer deur ko-presipitasie van Fe(II) and Fe(III) soute met ammonium hidrosied en toe bedek met tetraetiel ortosilikaat om silika-bedekte SPMNs te vorm. Vervolgens, die silika-bedekte SPMNs was toe gefunksionaliseer met amien metoksiesilaan ligande om magnetiese ioon-uitruiler materiale met **(1)** monoamien en **(2)** diamien funksionaliteit op te lewer. Die superparamagnetiese gedrag van die SPMNs was bevestig met vibrasie material magnetometrie en as sulks kon dit geskei word van die vloeistof fase (fase skeiding) by kamertemperatuur onder die invloed van 'n eksterne magnetiese veld (~ 0.35 T). X-straal diffraksie patrone dui aan SPMNs van relatief hoe suiwerheid met 'n inverse spinel struktuur. Die gemiddelde groottes van die ongefunksionaliseerde SPMNs en silika-bedekte SPMNs bepaal deur transmissie elektron mikroskopie was in die grens 4 – 15 nm en 60 – 80 nm, onderskeidelik. Die oppervlak areas soos bepaal deur BET analiese was 160.28 ± 0.77 m²/g en 183 ± 0.53 m²/g vir die ongefunksionaliseerde SPMNs en die silika-bedekte SPMNs, onderskeidelik. Met behulp van element analiese was die hoeveelheid amien metoksiesilaan ligande geïmobiliseer op **(1)** en **(2)** gevind as 0.75 mmol/g en 0.87 mmol/g, onderskeidelik.

Die verwydering van $[\text{AuCl}_4]^-$, $[\text{PdCl}_4]^{2-}$ en $[\text{PtCl}_4]^{2-}$ uit oplossings met materiale **(1)** en **(2)** was ondersoek as 'n funksie van HCl konsentrasie (0.01 M HCl – 0.5 M HCl), massa van material (10 – 50 mg), ioniese sterkte (0 – 1.5 mol L⁻¹) en kontak tyd. Daar was gevind dat die hoeveelheid $[\text{AuCl}_4]^-$, $[\text{PdCl}_4]^{2-}$ and $[\text{PtCl}_4]^{2-}$ verwyder uit oplossing toeneem met afnemende HCl konsentrasie, afnemende ioniese sterkte en toenemende massas. Soos verwag, was daar bevind dat **(2)** 'n hoer laai kapasiteit het as **(1)**. Vir materiale **(1)** en **(2)** is die maksimum laai kapasiteit van $[\text{AuCl}_4]^-$ 0.072 mmol/g (14.182 mg/g) en 0.111 mmol/g (21.863 mg/g), onderskeidelik. Die adsorpsie data was gepas met 'n Langmuir isoterm model. Daar is gevind dat die eksperimentele data goed ooreenstem met die Langmuir model, wat monoloaag $[\text{AuCl}_4]^-$ dekking voorstel. Die tempo van $[\text{AuCl}_4]^-$, $[\text{PdCl}_4]^{2-}$ and $[\text{PtCl}_4]^{2-}$ verwydering uit 0.5 M HCl oplossing met **(1)** en **(2)** was baie stadig. Uiteindelik was 55% van $[\text{AuCl}_4]^-$ verwyder uit oplossing met **(1)** en 96 % $[\text{AuCl}_4]^-$ met **(2)**. Verder, die affiniteit van $[\text{PdCl}_4]^{2-}$ and $[\text{PtCl}_4]^{2-}$ vir **(1)** and **(2)** was laag met slegs 11.9 % $[\text{PdCl}_4]^{2-}$ en 10.0 % $[\text{PtCl}_4]^{2-}$ verwyder uit 0.5 M HCl oplossings. Die tempo van $[\text{AuCl}_4]^-$, $[\text{PdCl}_4]^{2-}$ and $[\text{PtCl}_4]^{2-}$ verwydering was verbeter met experimente uitgevoer in 0.01 M HCl. Daar was gevind dat die adsorpsie maxima bereik was in minder as 30 minute en dat 76.8 %

$[\text{AuCl}_4]^-$, 95.9 % $[\text{PtCl}_4]^{2-}$ en 98.8 % $[\text{PdCl}_4]^{2-}$ verwyder kon word uit 0.01M HCl oplossings. Die verskil in die tempo van verwydering en die effektiwiteit kan verstaan word in terme van die kompetisie wat heers tussen die anioniese metaal komplekse en die toeskouer chloried ione vir die beskikbare geprotoneerde posisies op die ioon-uitruilers **(1)** en **(2)**.

In teenstelling met die stadige kinetika van adsorpsie vir $[\text{AuCl}_4]^-$ met **(1)** en **(2)**, ongefunktionaliseerde SPMNs toon hoe $[\text{AuCl}_4]^-$ effektiwiteit van verwydering met 'n relatiewe hoe tempo van verwydering. Daar is gevind dat $[\text{AuCl}_4]^-$ kwantitatief geadsorbeer word met die ongefunktionaliseerde SPMNs. Verder, is daar gevind dat die verwydering van $[\text{PdCl}_4]^{2-}$ en $[\text{PtCl}_4]^{2-}$ uit oplossing sterk afhanklik is van die molariteit van die oplossings indien ongefunktionaliseerde SPMNs gebruik word. Die verskil in verwydering gedrag van $[\text{AuCl}_4]^-$ in vergelyking met $[\text{PdCl}_4]^{2-}$ en $[\text{PtCl}_4]^{2-}$ met ongefunktionaliseerde SPMNs, dui dat twee verskillende meganismes verantwoordelik is vir die verwydering van die waardevolle metaal spesies uit oplossing en adsorpsie op die SPMNs. Ons rapporteer dat $[\text{PdCl}_4]^{2-}$ en $[\text{PtCl}_4]^{2-}$ effektief verwyder uit oplossing deur die SPMNs *via* elektrostatiese interaksie en dat $[\text{AuCl}_4]^-$ verwyder is uit oplossing *via* 'n reduksie-adsorpsie meganisme.

List of Equations, Figures, Tables, Schemes and Abbreviations.

Equations

Equation 1.	Anion exchange mechanism	5
Equation 2.	Formation of magnetite (SPMNs)	14
Equation 3.	Oxidation of Fe^{2+} to Fe^{3+} ions	15
Equation 4.	Formation of iron hydroxide	15
Equation 5.	Overall reaction of the formation of iron hydroxide	15
Equation 6.	Formation of maghemite	15
Equation 7.	Mass balance equation (mmol/g)	28
Equation 8.	Mass balance equation (%)	29
Equation 9.	Distribution coefficient equation	29
Equation 10.	Debye Scherrer equation	32
Equation 11.	Relationship between N_2 adsorbed and the relative vapour pressure	46
Equation 12.	Relationship between BET constant and volume	46
Equation 13.	Relationship between particle size and surface area	47
Equation 14.	Equation for the diameter of SPMN cores	50
Equation 15.	Standard deviation σ_M around the SPMN cores	50
Equation 16.	Langmuir isotherm model	61
Equation 17.	Linearized Langmuir model equation	61
Equation 18.	Freundlich isotherm model	61
Equation 19.	Linearized Freundlich model equation	61
Equation 20.	Transformation of Fe_3O_4 into $\gamma\text{-Fe}_2\text{O}_3$	80
Equation 21.	Reduction of Au(III) to Au(I) species	81

Equation 22.	Reduction of Au(I) to colloidal gold, Au(0) species	81
Equation 23.	Overall reduction reaction of Au(III) to Au(0) species	81

Figures

Figure 1.	Inverse spinel structure of SPMNs	8
Figure 2.	Different types of magnetisms of paramagnetic materials	9
Figure 3.	Aggregate formation caused by inter-particle magnetic coupling forces	10
Figure 4.	Magnetic domains within SPMN materials	11
Figure 5.	Hysteresis associated with superparamagnetic materials	12
Figure 6.	X-ray patterns of (a) uncoated Fe ₃ O ₄ and (b) FeSi nanomaterials	31
Figure 7.	TEM micrographs of SPMNs	34
Figure 8.	Corresponding size-distribution histograms of SPMNs	35
Figure 9.	TEM image of silica-coated SPMNs illustrating cluster formation	36
Figure 10.	EDX analysis images of modified SPMNs	39
Figure 11.	Monoamine and diamine functionalized silica-coated SPMNs	40
Figure 12.	TGA curves of SPMNs and modified SPMNs	42
Figure 13.	FT-IR spectra of SPMNs and modified SPMNs	44
Figure 14.	N ₂ adsorption-desorption isotherms of SPMNs	48
Figure 15.	N ₂ adsorption-desorption isotherms of silica-coated SPMNs	49
Figure 16.	Magnetization curves of SPMNs	51
Figure 17.	Effect of contact time on Pd(II) and Pt(II) adsorption by FeSiAPTS	55
Figure 18.	Effect of contact time on Pd(II) and Pt(II) adsorption by FeSiAPTS	56
Figure 19.	Effect of contact time on Au(III) adsorption by FeSiAPTS and FeSiED	58
Figure 20.	Effect of contact time on Au(III) adsorption by FeSiAPTS	59
Figure 21.	Adsorption data fitted to Langmuir and Freundlich isotherm models	63

Figure 22.	Effect of chloride ion concentration on Au(III) adsorption	65
Figure 23.	Adsorption of Au(III), Pd(II) and Pt(II) from 0.1 M HCl	68
Figure 24.	Effect of contact time on Au(III) adsorption from 0.5 M HCl by SPMNs	70
Figure 25.	Effect of contact time on Au(III) adsorption from 0.01 M HCl SPMNs	72
Figure 26.	Adsorption data fitted to Langmuir isotherm models	74
Figure 27.	Effect of contact time on Pd(II) and Pt(II) adsorption by SPMNs	75
Figure 28.	Effect of contact time on Pd(II) and Pt(II) adsorption by SPMNs	76
Figure 29.	Effect of HCl concentration on Pd(II) and Pt(II) adsorption by SPMNs	77
Figure 30.	Effect of free iron species in solution on gold loading onto SPMNs	83
Figure 31.	UV/Vis absorption spectrum of $[\text{AuCl}_4]^-$ in 0.01 M HCl	85
Figure 32.	UV/Vis absorption spectra of $[\text{AuCl}_4]^-$ after various contact times	86
Figure 33.	Gold and iron species left in solution as function of contact time	86
Figure 34.	UV/Vis absorption spectrum of $[\text{AuCl}_4]^-$ in 0.05 M HCl	88
Figure 35.	UV/Vis absorption spectrum of FeCl_3 stock solution in 0.5 M HCl	89
Figure 36.	UV/Vis absorption spectra absorption spectra of formed of iron species	89
Figure 37.	TEM image of gold-enriched SPMNs	90
Figure 38.	EDX image of gold-enriched SPMNs	91
Figure 39.	The amount of iron dissolution as a function of solution pH	104

Tables

Table 1.	ICP-AES operating conditions	27
Table 2.	Elemental analysis results of FeSiAPTS	41
Table 3.	Elemental analysis results of FeSiED	41
Table 4.	FT-IR absorption frequencies for the bare and silica coated SPMNs	45
Table 5.	Summary of fundamental properties of synthesized SPMN nanomaterials	52

Table 6.	Langmuir and Freundlich isotherm parameters for FeSiAPTS and FeSiED	64
Table 7.	R_L values of Au(III) based on the Langmuir isotherm model	64
Table 8.	Adsorption data of Au(III) removal from 0.5 M HCl using SPMNs	71
Table 9.	Adsorption data of Au(III) removal from 0.5 M HCl using SPMNs	73

Schemes

Scheme 1.	Conventional refining method for the separation of precious metals	2
Scheme 2.	Modern refining method for the separation of precious metals	3
Scheme 3.	Superparamagnetism of a Fe_3O_4 based ferrofluid	13
Scheme 4.	Magnetic separation of solid phase from aqueous phase	19
Scheme 5.	Silica coating procedure onto surface of SPMN material	23
Scheme 6.	Amine surface functionalization of silica-coated SPMNs	24
Scheme 7.	Steric repulsion of individual SPMNs in liquid media	33
Scheme 8.	Simplified representation of the silica-coating of SPMNs	38
Scheme 9.	Illustration of the loss of absorbed H_2O from the SPMN surface	43
Scheme 10.	Mechanism of $[AuCl_4]^-$, $[PdCl_4]^{2-}$ and $[PtCl_4]^{2-}$ removal from solution	66
Scheme 11.	Mechanism of $[AuCl_4]^-$, $[PdCl_4]^{2-}$ and $[PtCl_4]^{2-}$ removal from solution	67
Scheme 12.	$[AuCl_4]^-$, $[PdCl_4]^{2-}$ and $[PtCl_4]^{2-}$ interaction with SPMNs surface sites	78
Scheme 13.	Mechanism responsible for the adsorption of $[AuCl_4]^-$ by SPMNs	82
Scheme 14.	Amount of iron dissolution of SPMNs in various acidic solutions	104

Abbreviations

Fe_3O_4	magnetite
$\gamma\text{-Fe}_2\text{O}_3$	maghemite
$\alpha\text{-Fe}_2\text{O}_3$	hematite
SPMNs	superparamagnetic magnetite nanoparticles
FeSi	silica coated SPMNs
FeSiAPTS	monoamine functionalized FeSi
FeSiED	ethylenediamine functionalized FeSi
PGMs	platinum group metals (Ru, Rh, Pd, Os, Ir, and Pt)
ppm	parts per million
TEM	Transmittance electron microscopy
XRD	X-ray powder diffraction
EDX	Energy dispersive
FT-IR	Fourier-Transform Infrared spectroscopy
TGA	Thermogravimetric analysis
VSM	Vibrating Sample Magnetometry
BET	Bennet, Emmet and Teller surface area analysis
ICP-AES	Inductively Coupled Plasma-Atomic Emission Spectroscopy

List of chemicals

$\text{FeCl}_3 \cdot 6\text{H}_2\text{O}$	Ferric chloride hexahydrate
$\text{FeSO}_4 \cdot 7\text{H}_2\text{O}$	Ferrous sulphate heptahydrate
NH_4OH	Ammonium hydroxide
$\text{C}_2\text{H}_5\text{OH}$	Absolute ethanol
CA	Citric acid
TMA	Tetramethyl ammonium hydroxide
TEOS	tetraethyl orthosilicate
HCl	Hydrochloric acid
NaCl	Sodium chloride
$\text{HAuCl}_4 \cdot x\text{H}_2\text{O}$	Gold (III) chloride salt
K_2PdCl_4	Palladium (II) chloride salt
K_2PtCl_4	Platinum (II) chloride salt

Chapter One

Introduction and Background

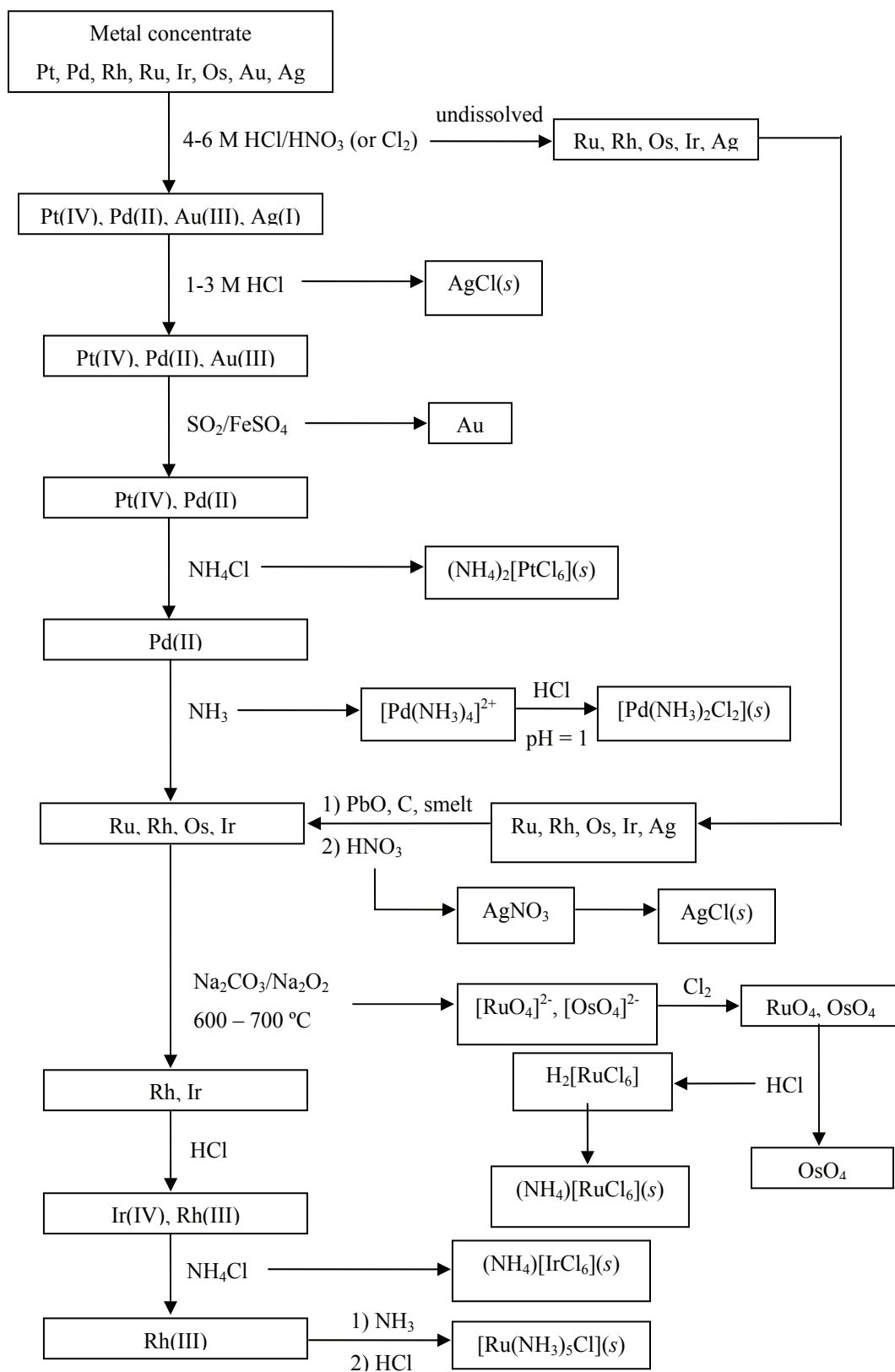
The fundamental properties of iron oxide-based nanoparticles are presented in this chapter, including relevant basic concepts, such as the classification of different types of magnetic behaviors observed in these materials. An application which involves magnetic separation of the precious metals using their novel characteristics will be then examined. In this context, the separation and recovery of precious metals from aqueous solutions will be briefly reviewed to give an overview of the research carried out in this work.

1.1 Overview of separation and recovery of precious metals from solution

Precious metals such as gold, platinum, and palladium are used extensively not only for jewellery, but also as in a variety of advanced applications such as electric and electronic devices, catalysts and medical instruments as a result of their specific physical and chemical properties.^[1] Furthermore, applications for these metals can be found in catalytic converters, gas sensors, and even in healthcare as anti-cancer drugs.^[2,3,4] The Platinum Group Metals (PGMs) are also vital in their industrial role as used in fiberglass production and petroleum refining.^[5] The precious metals have been historically important as currency and remain important as investment commodities.^[6] These metals constitute limited resources.^[7] Because of the value and scarcity of these precious metals, they must be effectively and economically recovered from waste aqueous solutions such as industrial process effluents.

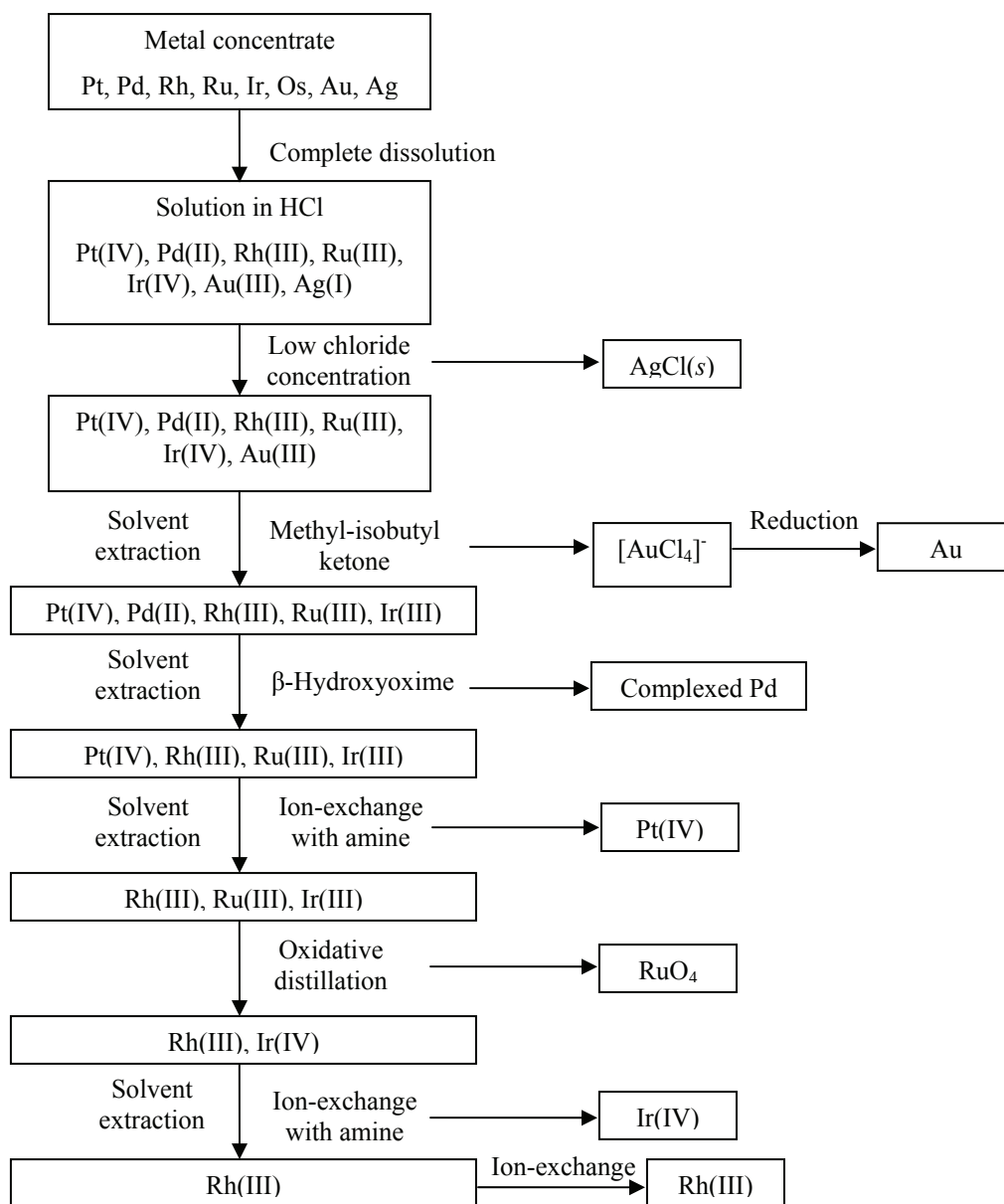
1.1.1 Conventional and modern refining processes

The conventional processes used for the separation and refining of precious metals (*i.e.* PGMs, gold and silver) consists of a series of steps involving dissolution using *aqua-regia* (a HCl/HNO₃ 3/1 molar solution), conditioning, and then precipitation.^[8,9] These processes are ineffective considering the final degree of purification, selectivity, yield, operational complexity, energy consumption, and labor costs. A summary of this conventional method is illustrated in *Scheme 1*.



Scheme 1. Conventional refining method for the separation of precious metals.^[8,9]

Attempts have been made in recent years to develop new processes. These processes consist of total leaching (complete dissolution) in hydrochloric acid containing chlorine gas or hypochlorite, followed by solvent extraction and ion-exchange.^[8,10] Such techniques have been employed by some refineries in South Africa.^[11] A summary of a more modern refining method of precious metal separation, based on a refining method used by Matthey Rustenburg Refiners on South African ores, is illustrated in *Scheme 2*.^[8]



Scheme 2. Modern refining method incorporating solvent extraction/ion-exchange for the separation of precious metals.^[8]

In the modern processes, relatively high separation selectivity and high final metal purity is obtained, and more complete removal of metals is also possible through the use of multi-stage extraction. This has effectively resulted in shortened refining times and lowered production costs.

However, research and development in the field of precious metal refining will always be fuelled by potential economic gains, which arise from new, faster, simpler and more efficient refining methods. In this context, some new materials for precious metals recovery have been developed mostly utilizing ion-exchange technology, and some of these have been employed for commercial purposes.^[12-16] Furthermore, besides the conventional ion-exchangers, chelating resins have been developed to take advantage of the intrinsic selectivity provided by functional groups. In conformity with the hard and soft acids and bases theory (HSAB), functional groups containing S and N donor atoms interact strongly with the soft acids like the precious metals.^[17,18] This led to the development of resins containing chelating groups containing S or N atoms. In particular, a great effort has been made in the modification of different polymeric matrices with such chelating groups. The chelating groups are either impregnated into the pores of the solid polymeric matrix of the resin or covalently bonded to the polymeric surface. Among those groups, thiol,^[19,20] thiosemicarbazide,^[21] dithiocarbamate,^[22] dithizone^[23,24] and tributylphosphine sulfide^[25] are of particular interest. There is a large body of literature on this topic that has recently been reviewed by Qu.^[26] Previous research in our group has focused on the immobilization of specific organic functional groups with metal binding ability onto silica-based surfaces to produce silica-based ion-exchanger materials.^[12,27,28] Some of these new materials have been successfully used for the recovery of PGMs from industrial metal refinery effluents.

In general, the refining processes suffer from some drawbacks ranging from large amounts of secondary waste solutions, to significant chemical additives, solvent losses and complex equipment. These shortcomings translate to an inability to effectively remove low concentrations of hazardous and precious metals in effluents at acceptable costs. The need for environmentally-friendly processes is of increasing importance. Mining and metallurgical waste waters are considered to be the major source of metal contamination to the environment, and the need for economic and effective methods for the removal of metals from waste solutions and for precious metals recovery has resulted in the development of new separation technologies.^[10]

In this research work focus is on the recovery of precious metals including gold, platinum and palladium from dilute aqueous acidic media using novel superparamagnetic materials. Under the experimental conditions used in this work, these precious metal species are mainly present in the aqueous chloride-rich solutions as stable anionic complexes. Therefore, it will suffice to only consider anion exchange as a fundamental means for recovery processes and mechanisms.

1.1.2 Ion-exchange

The separation and removal of precious metal complex anions from solution is, with increasing frequency, being carried out using ion exchange processes. Ion-exchange is a powerful method to selectively recover small amounts of metal ions from very dilute solutions. Ion-exchange is a reversible stoichiometric process, different to sorption in the sense that every ion removed from the solution is replaced by an equivalent number of another ionic species of the same sign.^[29,30] An ion-exchange material is usually an insoluble, three-dimensional network consisting of ionizable groups that are chemically bound to this framework. The material can have either cation or anion exchange groups. The structure of the network determines the physical properties of the ion-exchanger and the nature of the functional groups largely control the selectivity of the exchange reaction.^[30,31] There are two major classes of ion-exchangers: cation exchangers, whose functional groups can remove the cations of a surrounding solution; and anion exchangers, whose functional groups can undergo reactions with the anions of a surrounding solution.^[31] When an ion exchanger is brought into contact with an aqueous solution containing a counter-ion different from that initially bound to the material, an exchange of ions occurs until equilibrium is reached, as illustrated by equation (1) for an anion exchange process:



where R represents the fixed functional groups in the insoluble network of the ion-exchange material, A⁻ the complex metal anion and X⁻ the counter ion that takes part in the exchange reaction. Quantitative descriptions of this exchange process involve physico-chemical phenomena that fall essentially into two categories.^[31,32] One considers the exchange process as an adsorption phenomenon, while the other categorizes it as the interaction of coulombic forces in electrolytes, such as described by the mass-action law. As will be discussed in this thesis, we postulate that both these process are involved in the removal of the precious metals from aqueous solutions.

1.1.3 Removal of metals species from solution using iron oxide based materials

There is extensive literature concerning the use of iron oxide based materials as scavengers for metal ions. Iron oxides such as hematite ($\alpha\text{-Fe}_2\text{O}_3$) and magnetite (Fe_3O_4) have been used to study the extent of Co(II) ions adsorption.^[33-35] The results indicated that different structures of iron oxides showed different sorption capacity. Todorovic *et al.* reported that $\alpha\text{-Fe}_2\text{O}_3$ was a better sorbent than Fe_3O_4 , a fact that can be attributed to differences in their crystal structures.^[36]

In our group, Vatta *et al.* have studied the extraction of Co(II) ions from an aqueous cobalt sulfate/potassium thiocyanate solution using magnetite nanoparticles and magnetite based magnetic liquid.^[37] It was found that both unfunctionalized magnetite and the magnetic liquid were capable of extracting from solution the formed $\text{Co}(\text{SCN})_4^{2-}$ complexes with rapid extraction kinetics. Vatta *et al.* also studied the percentage of Cu(II) extracted in the form of $[\text{Cu}(\text{H}_2\text{O})_6]^{2+}$ using Fe_3O_4 nanoparticles, silica-coated Fe_3O_4 (FeSi) and diethylenetriamine functionalized silica-coated Fe_3O_4 nanoparticles (FeSiDETA).^[38] The order of $[\text{Cu}(\text{H}_2\text{O})_6]^{2+}$ extractability was found to be FeSiDETA > Fe_3O_4 > FeSi. It was reported that using FeSiDETA, extraction occurs through a complexation (chelating) ion mechanism, where coordination to $[\text{Cu}(\text{H}_2\text{O})_6]^{2+}$ readily takes place *via* the lone pairs of the amine groups. For Fe_3O_4 and FeSi nanoparticles, it was reported that $[\text{Cu}(\text{H}_2\text{O})_6]^{2+}$ extraction is dependant on their surface charge. Furthermore, Vatta *et al.* have also examined the potential use of diethylenetriamine functionalized silica-coated Fe_3O_4 nanoparticles for the selective removal of $[\text{PdCl}_4]^{2-}$ from aqueous solutions.^[38] It was found that from a mixed metal solution, FeSiDETA could quantitatively and selectively remove $[\text{PdCl}_4]^{2-}$ over $[\text{Cu}(\text{H}_2\text{O})_6]^{2+}$ ions.

Hu *et al.* examined the removal of CrO_4^{2-} from wastewater also using Fe_3O_4 nanoparticles.^[39] They found that adsorption of CrO_4^{2-} by Fe_3O_4 followed the Freundlich isotherm model and was pH and temperature dependant.

The deposition of $[\text{AuCl}_4]^-$ on iron oxides as well as on other mineral surfaces, *i.e.* quartz (SiO_2), pyrite (FeS_2) and galena (PbS), was studied by Bancroft *et al.*^[40] It was found that gold ions are adsorbed onto these materials *via* a reductive mechanism. It was proposed that the quadridentate Au complex $[\text{AuCl}_4]^-$ is chemically adsorbed to the surface prior to its reduction to the metal. An intermediate of Au(I) was proposed.

In a similar study, the adsorption of $[\text{AuCl}_4]^-$ by goethite (FeOOH) was studied by Machesky *et al.*^[41], who reported that the $[\text{AuCl}_4]^-$ species were adsorbed in an inner-sphere, by a bidentate mechanism at low surface coverage, while the loading capacity of $[\text{AuCl}_4]^-$ was determined to be

0.2 mmol g⁻¹ at pH 4. An overview of the basic concepts of the nanoparticles is presented in section 1.2 in order to give the reader background information.

1.2 Overview of iron oxide based nanoparticles

Nanotechnology is nowadays considered as an important new advancement in science and technology. It is related to the manipulation of materials at the nanometer scale. Interest in nanoscale materials has increased in the last decade due to their unique characteristics resulting from their finite size, for example their high surface area, high surface reactivity, a large number of active sites on the surface, high catalytic efficiency, and strong adsorption ability. Significantly at this scale, materials exhibit *new* properties for novel applications.^[42-46]

Nanoparticles are small particles with dimensions characteristically less than 100 nm, and are usually crystalline.^[42] In particular, iron oxide nanoparticles are nowadays well known and have been investigated intensively in many areas of research and potential applications in industry.^[42,44] Most importantly, iron oxide nanoparticles are often magnetic by nature, which means that they obey Coulomb's law, and can be manipulated by an external magnetic field gradient.^[42,47,48] As a result of their unique properties, the iron oxide based nanoparticles are used in various applications such as magnetic recording media,^[49] magnetic refrigeration,^[50] electronics,^[51] optics^[52] and ferrofluids.^[51-54] Moreover, research applications using related iron oxide based nano-materials are also found in biotechnology and medically-related fields such as targeted drug delivery,^[55] magnetic resonance image contrast enhancement agents,^[56] cell isolation^[57] and hyperthermia.^[58] In particular, these applications are possible mainly as a result of the unique size distribution of the nanoparticles. Nanoparticles have sizes that are smaller or comparable to that of a cell (10 – 100 μm), virus (20 – 500 nm), a protein (5 – 50 nm) or a gene (2 nm wide and 10 – 100 nm long).^[59,60] This means that they can interact in a unique manner with a biological entity of interest. Most biological applications require the nanoparticles to be embedded in a non-magnetic matrix to avoid aggregation and/or sedimentation, as well as to endow the surface with particular properties for the desired applications. For example, the nanoparticles can be coated with biological molecules to make them interact with or bind to a biological entity, thereby providing controllable means of 'tagging' biomolecules in order to take advantage of magnetic properties of the nanoparticles.^[61] Magnetic separation has been successfully applied to many aspects of biomedical and biological research.^[62] No attempt will be made here to review the extended literature concerning these biological applications.

1.2.1 Crystal structure of iron oxide based nanoparticles - magnetite

Among all iron oxide nanoparticles, magnetite (Fe_3O_4) presents the most interesting properties due to its unique magnetic structure as a result of the presence of iron cations in two valence states, Fe^{2+} and Fe^{3+} in the crystal structure. For that reason, only magnetite and related materials was studied. Magnetite is found in abundance in nature and can also be readily synthesized.^[42,63]

Magnetite is a cubic mineral with an inverse spinel structure as shown in *Figure 1*. The inverse spinel structure of magnetite has the general formula $\text{Fe}_3\text{O}_4 = (\text{Fe}^{3+})_A (\text{Fe}^{3+}\text{Fe}^{2+})_B \text{O}_4$, where A and B symbolize the iron cations which are distributed on tetrahedral and octahedral interstitial sites, respectively. The Fe^{2+} ions and half the Fe^{3+} ions occupy octahedral sites; the other half of the Fe^{3+} ions occupies tetrahedral sites. As illustrated in *Figure 1*, a unit cell consists of four A and four B sites with lattice constants of $a = 8.396 \text{ \AA}$. The three-fold axis of rotation is along the diagonal $[111]$ of the cubic cell. The inverse spinel structure of Fe_3O_4 consists of oxide ions in a face-centered cubic (fcc) close packed arrangement in which 1/3 of tetrahedral interstices and 2/3 of octahedral interstices coordinate with oxide ions.^[42,63]

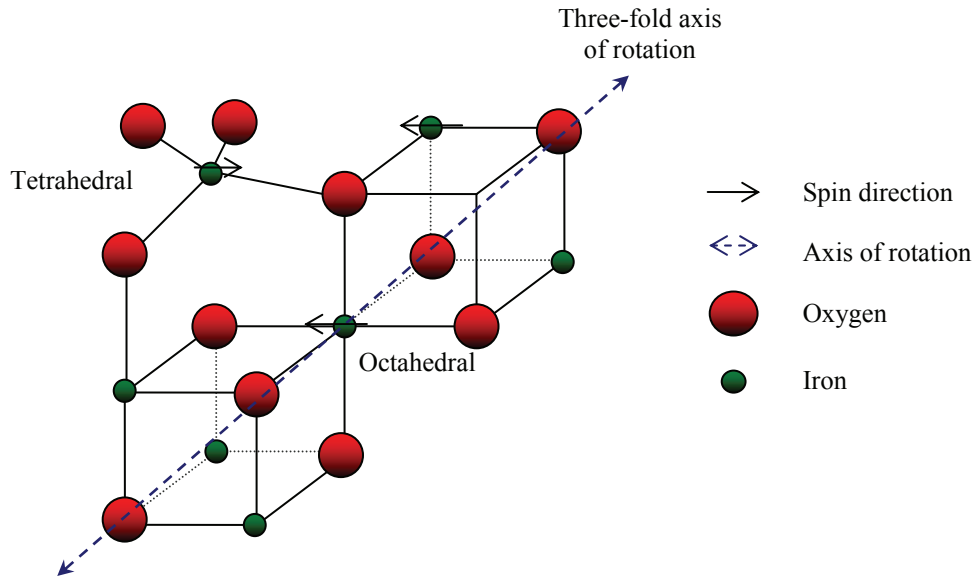


Figure 1. A portion of the inverse spinel structure of Fe_3O_4 , where iron(II) and iron(III) ions are indicated as small (green) dots and the larger oxide anions are indicated as red dots.^[42]

Furthermore, as illustrated in *Figure 1*, the electron spins of Fe^{3+} ions in octahedral interstices are aligned antiparallel to those in tetrahedral interstices, and hence no net magnetization is observed from these ions. The Fe^{2+} ions tend to align their spins parallel to those of Fe^{3+} ions in adjacent octahedral sites leading to a net magnetization.

1.2.2 Magnetic properties of iron oxide based nanoparticles - magnetite

Iron oxide nanoparticles such as Fe_3O_4 often possess magnetic properties resulting in their response to an applied magnetic field. The magnetic properties of iron oxide nanoparticles arise from electrons in motion.^[42] Electrons spinning and revolving in orbits around atomic nuclei generate magnetic dipoles. The magnetic dipoles can either align in opposite directions, causing cancellation, or can align in the same direction as the applied external magnetic field, producing bulk magnetism.^[64,65,66] There are various forms of magnetism characteristic to iron oxide nanoparticles that can arise depending on how their magnetic dipoles interact with each other. Any atom or ion of such nanomaterial that has one or more unpaired electrons is said to be paramagnetic.^[42,65] This means that it, or any other material in which it is found, will be attracted into a magnetic field. It should be emphasized that these materials will possess a stable magnetic moment only in the presence of an applied external magnetic field. In cases where paramagnetic atoms or ions are very close together and each one is strongly influenced by the orientation of the magnetic dipoles of its neighbours, more complicated forms of magnetisms can arise (as shown in *Figure 2*). Examples of such magnetism may include ferromagnetism, antiferromagnetism, and ferrimagnetism.^[42,64,65] Briefly, in ferromagnetism the interaction is such as to cause all magnetic dipoles to point in the same direction of the external magnetic field. Antiferromagnetism occurs when the nature of the interaction between neighbouring paramagnetic atoms or ions favours opposite orientations of their magnetic dipoles, thus causing partial cancellation. Ferrimagnetism is associated with materials in which the magnetic dipoles of the atoms on different sub-lattices are opposed. This happens when the sub-lattices of the material consists of different ions, such as metal ions with different valences.^[42]

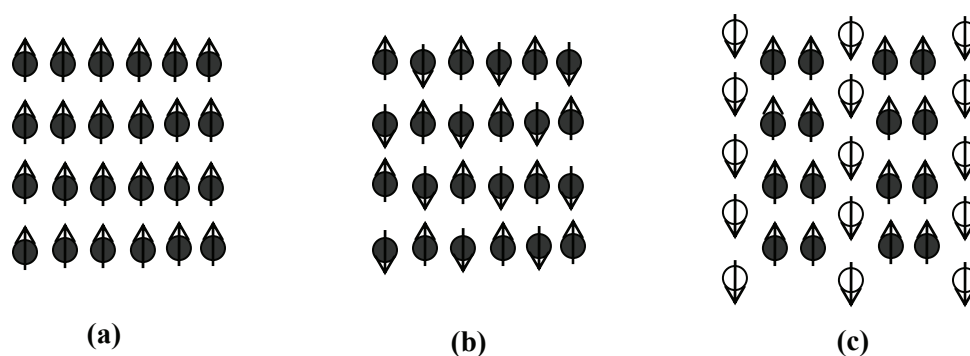


Figure 2. Different types of magnetisms of paramagnetic materials associated with iron oxide based nanoparticles: (a) ferromagnetism; (b) antiferromagnetism; and (c) ferrimagnetism. Atoms or ions consisting of different valences are shown as ● and ○ with spin direction of magnetic dipoles indicated by the arrows.

1.2.3 Superparamagnetism associated with Fe_3O_4 nanoparticles

The problem with nano-sized Fe_3O_4 materials is that the individual nanoparticles possess high surface energies, because of their large ratio of surface area to volume.^[67] For this reason, they have the tendency to interact with each other forming large aggregates in order to minimize their total surface energy. Moreover, because the Fe_3O_4 nanoparticles are magnetic by nature, there is an additional contribution from strong, short range inter-particle magnetic dipole-dipole forces that further facilitates aggregate formation as illustrated in *Figure 3*.

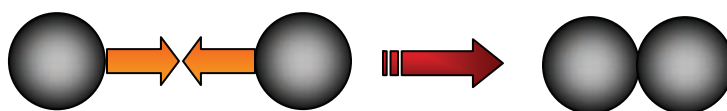


Figure 3. Illustration of aggregate formation caused by inter-particle magnetic coupling forces.

However, when the diameter of the Fe_3O_4 nanoparticles is reduced to below a certain critical value (usually less than 35 nm), they lose their bulk ferromagnetism and are said to become superparamagnetic.^[68,69] Superparamagnetism is associated with finite size and surface effects that dominate the magnetic behavior of individual nanoparticles.^[42,64] This phenomenon of superparamagnetism arises when the thermal energy within magnetic domains is sufficient to overcome the magnetic coupling forces between the nanoparticles, causing their atomic magnetic dipoles to fluctuate randomly. When an external magnetic field is applied, the nanoparticles acquire a certain magnetization, but because of the high thermal energy, the long range order is lost when the field is removed and the nanoparticles have no remanent magnetization.^[64-66]

The superparamagnetic properties of Fe_3O_4 nanoparticles are unusual because they represent single magnetic domains as illustrated in *Figure 4*. The ordering of electron spins characteristic of magnetic nanoparticles leads to the formation of regions of magnetic alignment called the domains.^[42,64] Thus a magnetic domain describes a region within a material which has uniform magnetization. The nanoparticles can become magnetized when the magnetic domains within the material are magnetized and aligned. This can be done by applying a moderate external magnetic field or by passing an electrical current through the bulk material, so that individual magnetic domains tend to align in the same direction as the external field. Some or all of the domains can be aligned. The more domains that are aligned the stronger the resultant magnetization of the material. When all of the domains are aligned, the material is said to be magnetically saturated.

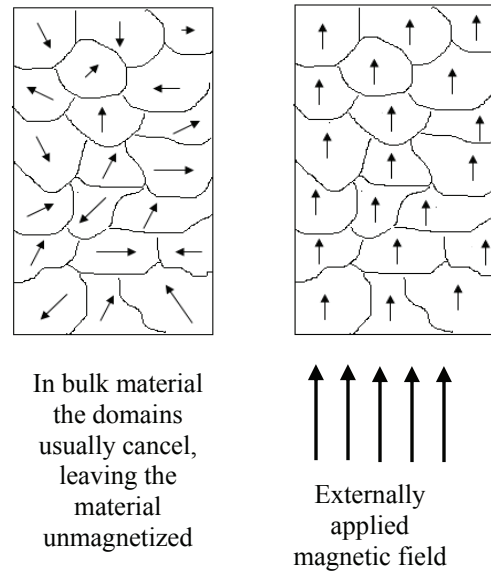


Figure 4. Illustration of magnetic domains within superparamagnetic Fe_3O_4 material.

For simplicity, throughout the rest of this thesis, superparamagnetic (Fe_3O_4) nanoparticles will be referred to as SPMNs.

1.2.4 SPMNs in ferrofluids and magnetic properties

Due to their small size, superparamagnetic Fe_3O_4 nanoparticles (SPMNs) can be dispersed in an appropriate carrier liquid (aqueous or non-aqueous) to form stable colloidal suspensions called ferrofluids or magnetic liquids. Such dispersions are stable for years, contrary to the so-called magnetorheological fluids, which are dispersions of micron-sized particles.^[65] Ferrofluids do not settle with time, not even when a magnetic field is applied. As alluded to previously, this stability can be attributed to thermal energy that is sufficient to overcome the magnetic coupling forces between the nanoparticles. Therefore, ferrofluids display the phenomenon of superparamagnetism. That is to say they exhibit no net magnetization in the absence of an external magnetic field, but they exhibit relatively large saturation magnetizations (~ 20 kA/m) in the presence of moderate (200 kA/m) applied fields.^[42,66] This superparamagnetic behavior is a feature that is in accordance with what should be expected from their finite nanoparticle size. Magnetic properties of SPMNs can be studied *via* a magnetization curve. To induce magnetization, the nanoparticle sample is exposed to an external magnetic field, \mathbf{H} , and the magnetization, \mathbf{J} , is recorded with a

magnetometer. During this process, the magnetic material traces out a magnetization curve commonly known as a hysteresis loop similar to the one shown in *Figure 5*.

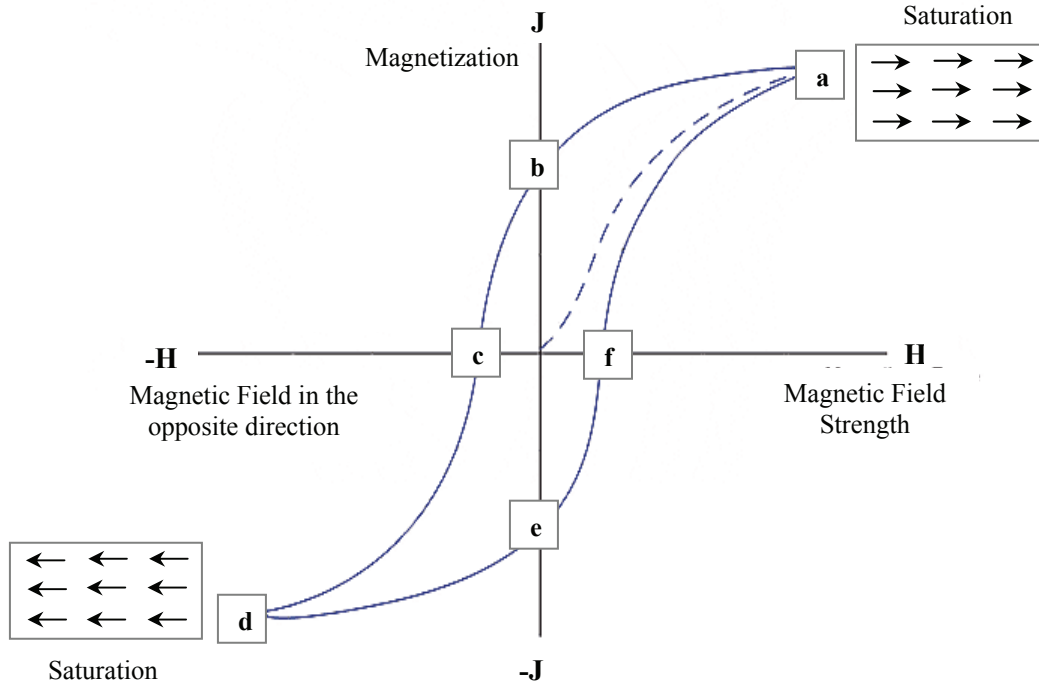
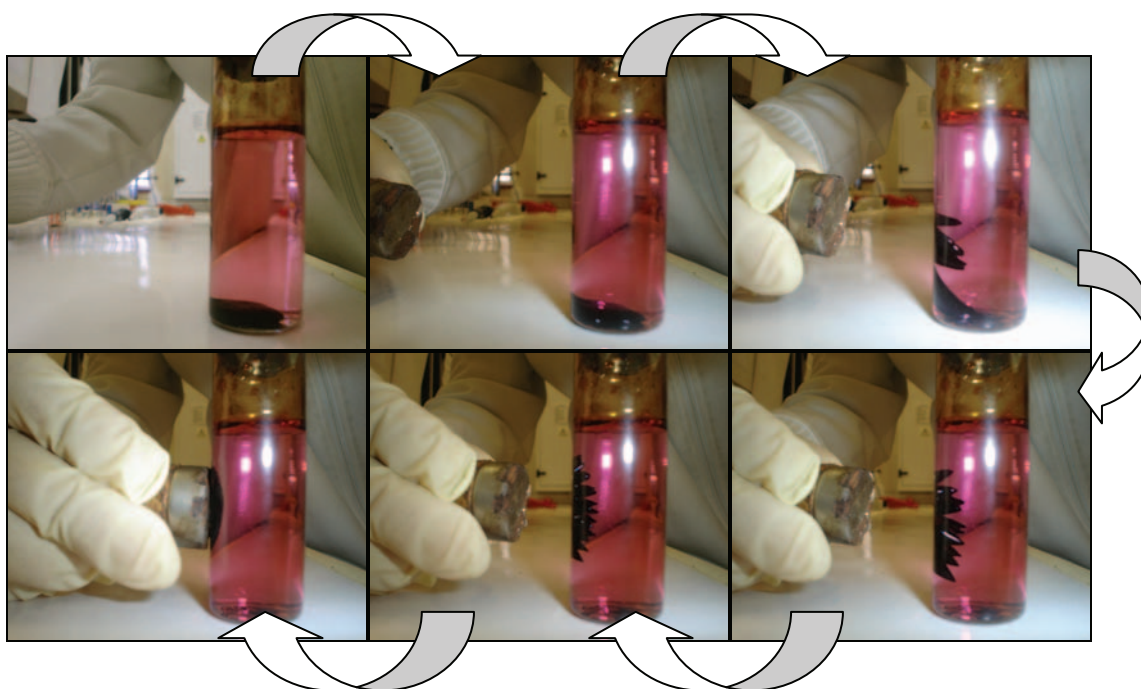


Figure 5. Illustration of hysteresis associated with superparamagnetic materials.

As can be seen from *Figure 5*, with increasing magnetic field, the magnetization, \mathbf{J} , of the material increases up to point **a** where magnetic saturation is reached. At this point, an additional increase in \mathbf{H} will produce very little increase in \mathbf{J} . Furthermore, at this point all the magnetic dipoles of the material are oriented parallel to one another. When the magnetic domains within the material are magnetized, the material will not relax back to zero magnetization when the applied magnetic field is removed. Thus, when \mathbf{H} is reduced to zero, the curve will follow the path from **a** to **b**. The reason for this is that some of the magnetic domains remain aligned after the magnetic field is removed. The amount of magnetization that the material retains after the magnetic field is removed (zero applied field) is called the remanance (labeled **b** and **e** in *Figure 5*). As the magnetic field is reversed, the curve follows the path from **b** to **c**. The force needed to remove the remanance, *i.e.* the residual magnetism, is called the coercivity of the material. Upon increasing the magnetic field further in the negative direction, the material will again become magnetically saturated (point **d**). Continuing applying the magnetic field but in the opposite direction, the curve will follow the path back to **a** and eventually complete the hysteresis loop.

It is important to point out that zero coercivity and zero remanance (*i.e.* no hysteresis effect) on the magnetization curve indicate that the material is superparamagnetic in nature as indicated by the dotted lines in *Figure 5*. Shown in *Scheme 3* is an illustration of the superparamagnetic behavior (characteristic “spiking”) of organic-based ferrofluid suspended in an aqueous phase. The ferrofluid was obtained by coating and thus sterically stabilizing synthesized SPMNs with surfactant molecules (oleic acid). Kerosene was used as an organic medium. The external magnetic field source used to manipulate the superparamagnetic ferrofluid is a small ferrite magnet.



Scheme 3. Superparamagnetism of a Fe_3O_4 based ferrofluid suspended in an aqueous phase.

With the advancements of material science especially in the area of nano-materials, efforts have been made to alter the nanoparticle properties for specific applications. Recently, various approaches have been reported for the fabrication of SPMNs. Since SPMNs, silica coated SPMNs and also modified silica coated SPMNs were synthesized for our application, it is essential to give the reader background information regarding these synthetic procedures.

1.2.5 General discussion on the preparation of superparamagnetic nanomaterials

1.2.5.1 Synthesis of SPMNs

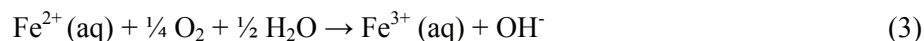
The synthesis of SPMNs and nanocomposite materials of a controlled size has long been of scientific and technological interest.^[42] The reduction of iron oxide nanoparticle size leads to *new* and unusual magnetic properties of which superparamagnetism is the most important. Various synthetic methods have been reported in the literature for the preparation of SPMNs which include ball milling,^[70] chemical precipitation,^[71-74] thermal decomposition,^[75] and sonochemical methods of preparation.^[76] Chemical precipitation is the most common and successful approach. Synthesis of SPMNs through chemical precipitation includes: (1) coprecipitation of Fe³⁺ and Fe²⁺, (2) partial reduction of Fe³⁺, and (3) partial oxidation of Fe²⁺, followed by coprecipitation. Aqueous coprecipitation of Fe³⁺ and Fe²⁺ at a ratio of 2:1 to prepare the SPMNs is usually carried out in the presence of a base at pH 9 – 12 under anaerobic conditions.^[71-74] Important factors that will have a direct influence on the nanoparticle size and morphology are agitation time, reagent concentrations and pH of the solution. It has been demonstrated by Alivisatos *et al.*^[77] and Tegus *et al.*^[78] that, at nanoscale, it is possible to tune the physical, chemical, electronic and magnetic properties by modifying the nanoparticles size and shape, which in turn was critically dependant on the experimental conditions.

The co-precipitation technique is the most versatile and convenient of all the above mentioned methods, not only for laboratory purpose but also potentially on larger scale for industrial purposes.^[63] Moreover, this technique is cost effective, which further facilitate large scale synthesis. For these reasons the co-precipitation techniques have been used for the synthesis of SPMNs in the presented work. Even though co-precipitation technique has been used extensively for the synthesis of SPMNs for the last few decades, the exact mechanisms to control the final nanoparticle size and distribution are still not clear. In this regard, an understanding of the process of nanoparticle growth is a prerequisite to tailor nanoparticles of the desired size, shape and properties. This is still the subject of much research.^[78,79]

The overall deceptively simple chemical reaction for precipitation of SPMNs *via* co-precipitation from aqueous alkaline solutions can be expressed by a simplified mass balance equation as follows^[42,63,67,80]



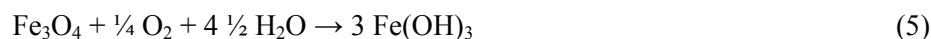
According to reaction equation 2, an initial molar ratio of $\text{Fe}^{3+} : \text{Fe}^{2+} = 2 : 1$ is required for the production of mixed oxidation state Fe_3O_4 small enough to behave as SPMNs. It is known that Fe^{2+} could readily be oxidized by dissolved or atmospheric molecular O_2 in solution, according to equation (3) below



This in turn leads to favorable conditions for the production of extremely insoluble $\text{Fe}(\text{OH})_3$



Overall this oxidation can be represented as follows



As a result of dissolved O_2 , another possibility is the formation of *maghemite* ($\gamma\text{-Fe}_2\text{O}_3$) as illustrated by equation (6)



Usually when Fe_3O_4 nanoparticles (SPMNs) are precipitated, the $\gamma\text{-Fe}_2\text{O}_3$ phase is likely to be present in the batch sample to a certain degree depending on the amount of Fe^{2+} oxidation that occurred. The formation of *hematite* ($\alpha\text{-Fe}_2\text{O}_3$) is more difficult to obtain than that of the $\gamma\text{-Fe}_2\text{O}_3$ phase, occurring only under thermal dehydration conditions.^[42,63]

Another important prerequisite for SPMNs formation during the synthesis is control of pH of the aqueous solution.^[81] A complete precipitation of Fe_3O_4 is expected between $\text{pH} = 7.5 - 14$, while maintaining a molar ratio of $\text{Fe}^{3+} : \text{Fe}^{2+} = 2 : 1$.^[80] Furthermore, rapid addition of the base with vigorous stirring of the aqueous suspension is essential, since it facilitates the formation of excess number of nuclei and prevents coagulation of particles. Synthesis under vigorous non-magnetic mechanical stirring (use of a mechanical agitator) is also important since it results in the formation of small particles (which is desirable) by reducing their tendency to agglomerate.^[42,63]

1.2.5.2 Synthesis of silica-coated SPMNs

As mentioned previously, SPMNs are not stable in aqueous dispersions and have a tendency to agglomerate. To circumvent this problem, the SPMNs could be coated with surfactant molecules to enhance their stability in solution.^[82-84] However, in some cases even when the SPMN surfaces are coated with surfactant molecules, agglomeration still occurs. This aggregate formation could then be attributed to insufficient coating of the surfactant molecules or as a result of inter-particle dipole-dipole forces being strong enough to overcome the repulsive forces or the steric hindrances provided by the surfactant molecules. It has been reported that the formation of an outer protective layer on the surfaces of nanoparticles could help prevent their agglomeration in aqueous media.^[83] In this regard, many types of organic and inorganic materials have been employed to prepare coated nanocomposite materials.^[61,85-87] High mechanical rigidity, resistance to aqueous solutions of acidic content and long shelf life make inorganic materials ideal for nanoparticle surface protection agents. The encapsulation of the SPMNs within an inert silica shell, which could further prevent direct contact between nanoparticles, is of particular interest. The silica layer formed on the surfaces of SPMNs could screen the magnetic dipolar attraction between SPMNs, which favors the dispersion of these SPMNs in liquid media and also protects them from leaching in an acidic environment.^[87,88] Another advantage of the silica shell is that the inert silica coating on the nanoparticles improves chemical stability and will protect the SPMN core(s) from oxidation in aqueous media. Finally and most importantly, the silica surface is terminated by abundant silanol groups which can react with various coupling agents to covalently attach specific ligands to their surfaces.^[38,87,89-91]

There have been numerous reports in the literature that describe the various routes of the formation of silica-coated magnetic nanocomposite materials.^[82,87,88,92-96] However, only the four major ones will be briefly mentioned here. The first method, as reported by Vestal *et al.*, is based on an *in situ* formation of magnetic nanoparticles in the pores of pre-synthesized silica using metal compounds as the source of magnetic phase.^[92] The second method was reported by Chow *et al.*^[93]. In this method, silica-coated magnetic nanoparticles were prepared by the aerosol pyrolysis of a precursor mixture composed of silicon alkoxides and metal compounds in a flame environment. Tartaj *et al.*^[94] demonstrated the use of this technique for the synthesis of mesoscale silica beads containing magnetic nanoparticles. The third method, as reported by Zhang *et al.*^[95], is based on a micro emulsion method. The fourth major method, commonly known as the Stober sol-gel method,^[82,96] is the most widely used method for coating nanoparticles with silica. This method relies on the use of silicon alkoxides as the source of silica matrix. The silica phase is

normally formed on colloidal magnetic nanoparticles *via* hydrolysis and poly-condensation of tetraethyl orthosilicate (TEOS) in basic alcohol/water mixture. The silanol groups (Si-OH) are transformed to siloxane bonds (Si-O-Si) *via* condensation reactions and the silica coating forms on the particles surfaces. Stober *et al.*^[96] have reported synthesis of spherical silica particles from tetraethoxysilane (silica precursor) using ammonia as catalyst.

The sol-gel route was preferred in the preparation of the silica coated SPMN nanocomposite materials for our study.

Factors that affect the silica composite nanoparticle size and size-distribution include pH, temperature, type of alcohol, amount of silica precursor (TEOS) added and amount of catalyst used during the coating procedure.^[84,97-99] In the silica composite synthesis, ammonia is normally used as the catalyst to promote the condensation of the hydrolyzed alkoxide without destabilization of the dispersion. A silica layer on the surface of magnetic nanoparticles may be desirable not only because it can create a functional surface to tailor dispersibility of the nanoparticles but can also be used to form an insulating layer to control electron tunneling between particles, which may be important in charge transport or magneto-optics. In addition, the silica coating can also provide better protection against toxicity in biological systems.^[100]

1.2.5.3 Synthesis of modified silica-coated SPMNs

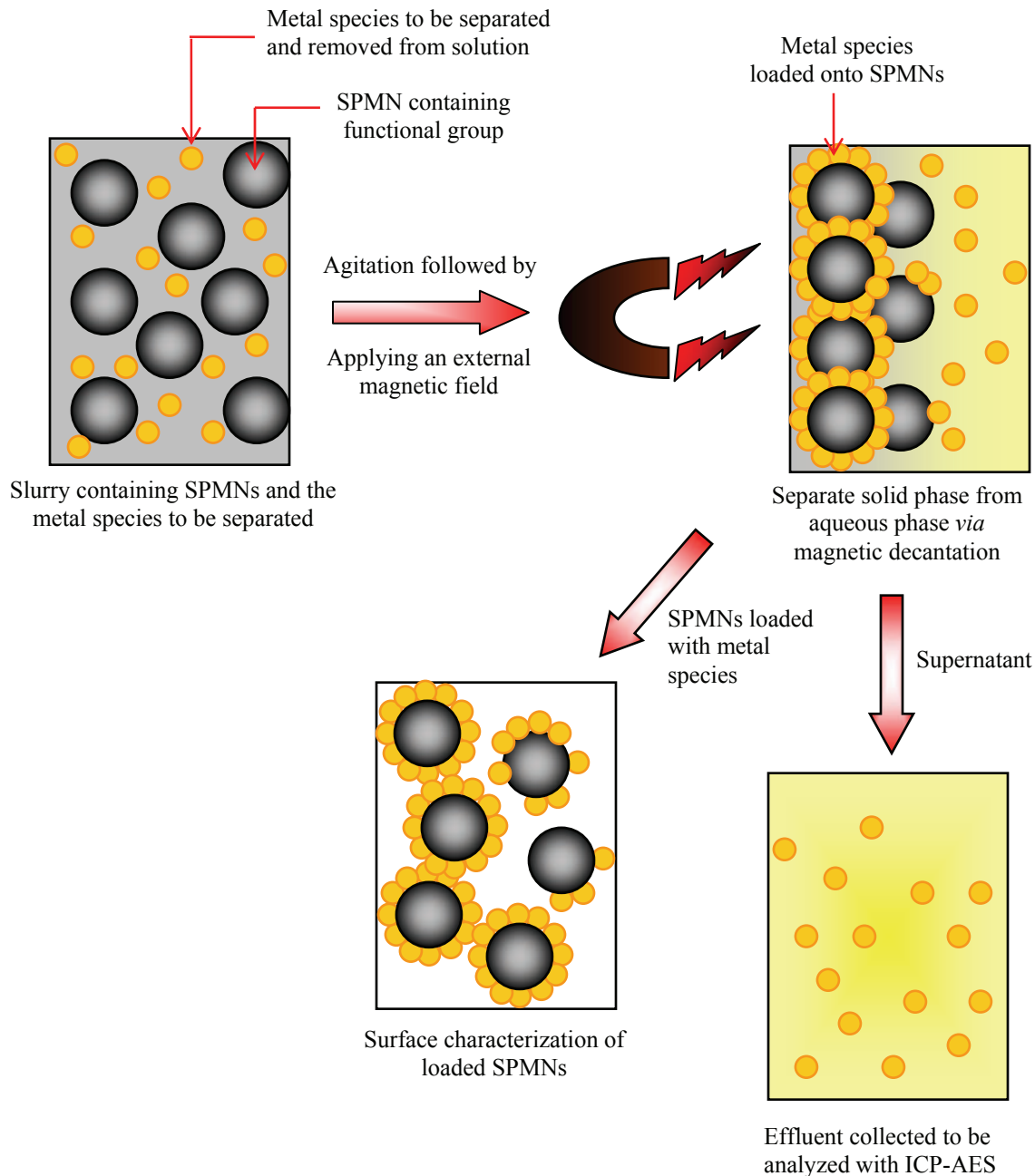
The outer silica surface of the silica-coated SPMNs prepared by the Stober sol-gel method^[82] have extensive hydroxyl groups on the surface and can be functionalized using a variety of surface chemistry.^[89-91] Immobilization of organic functional groups on siliceous surfaces have been successfully employed to produce a variety of modified silica surfaces. Kramer *et al.* has shown that amine alkoxy silane ligands with metal chelating ability can be immobilized onto silica-gel.^[101] Similar studies were done by Vatta *et al.*, in which case amine alkoxy silane ligands were immobilized onto silica-coated magnetite nanoparticles.^[38] In other studies, Mikhaylova^[74] and Ma^[90] synthesized iron oxide nanoparticles using the coprecipitation method and reported a procedure for modifying the bare nanoparticle surface with amino-terminated silanes making use of the abundant silanol groups offered by nanoparticle surface.^[89] Therefore, surface modification *via* functional group immobilization is being pursued with great interest since it can provide unique opportunity to engineer the interfacial properties of solid substrates while retaining their basic geometry. The process of surface modification involves silanization reactions which are very complex. The reaction between an alkoxy silane and a solid material does not involve a

single mechanism, and many different intermediates are possible.^[102] The alkoxy silanes can bind to the silica-coated surface by adsorption or covalent bonding. Thus modified, a nanoparticle is able to react with biomolecules, drugs and metals through the active functional group in its structure.^[38,89,101]

1.3 Magnetic separation

In this work, SPMNs have been synthesized, modified and tested for $[\text{AuCl}_4]^-$, $[\text{PdCl}_4]^{2-}$ and $[\text{PtCl}_4]^{2-}$ removal and adsorption. The aqueous solutions containing the precious metals were put in contact with the synthesized nano-adsorbent and ion exchanger materials (solid phase) through a batch method. In the batch method, the contact of the solid phase and aqueous phase are made by agitating or shaking to form a slurry. After a certain time interval, the solid phase is separated from the aqueous phase by magnetic sedimentation, and the collected supernatant is analyzed with ICP-AES for metal ion content. Due to their superparamagnetic behavior, the large surface area and high surface reactivity, these materials are excellent candidates for combining metal adsorption properties with ease of phase separation.

Magnetic separation using the solid phases, SPMNs and amine-functionalized silica coated SPMNs involves a two step process: (i) interaction or tagging of the metal species with the surface functional groups on the superparamagnetic materials through electrostatic interaction *via* an ion exchange mechanism, and (ii) the separation of these tagged entities *via* magnetic separation utilizing a strong external magnetic field. This process is illustrated in *Scheme 4*. The black spheres represent unfunctionalized SPMNs or modified SPMNs used as adsorbent or ion exchanger materials, respectively. The yellow circles represent the precious metal species in solution. The process can be summarized as follows: Initially, aqueous phase containing metal species are put in contact with the solid phase through the batch method. At this stage there is interaction between the metal species and the protonated surface sites on the solid materials causing them to adsorb onto these materials. Applying an external magnetic field, the solid phase containing the adsorbed metal species is separated from the aqueous phase. The obtained effluent is then analyzed for residual metal species left in solution with ICP-AES. Using mass balance equations, the amount of metal adsorbed onto the solid phase can be determined.



Scheme 4. Illustration of magnetic separation of solid phase containing the adsorbed metal species from the aqueous phase.

1.4 Aims of research

In this project, a more economical and efficient process for recovering $[\text{AuCl}_4]^-$, $[\text{PdCl}_4]^{2-}$ and $[\text{PtCl}_4]^{2-}$ from aqueous acidic chloride-rich solutions, particularly those aqueous solutions having low concentrations of the metals is explored. In this regard, the objective of this study is to investigate the role and effectiveness of synthesized SPMNs and amine-functionalized silica-coated SPMNs for the removal of $[\text{AuCl}_4]^-$, $[\text{PdCl}_4]^{2-}$ and $[\text{PtCl}_4]^{2-}$ from aqueous acidic solutions. Possible mechanisms that could be responsible for the removal of these precious metals species by the synthesized materials are also discussed but not examined in detail as part of this work. Due to the superparamagnetic properties of these materials, they can be easily manipulated by applying an external magnetic field (~ 0.35 T). This characteristic potentially presents us with a novel, convenient technology to separate the precious metals more easily as compared to conventional ion-exchange processes for which columns or filtration is required to recover these metals from solution.

To the best of my knowledge, no work on the adsorption behavior of $[\text{AuCl}_4]^-$ by SPMNs has been reported.

Therefore, the specific objectives were:

- (a) Synthesis and characterization of SPMNs.
- (b) Modification of SPMNs including silica coating and surface functionalization with amine methoxysilane ligands.
- (c) Testing these unmodified SPMNs and modified SPMNs as nano-adsorbents and superparamagnetic ion exchangers for the potentially selective recovery of $[\text{AuCl}_4]^-$, $[\text{PdCl}_4]^{2-}$ and $[\text{PtCl}_4]^{2-}$ from aqueous acidic solutions.

Chapter Two

Materials and Methods

This chapter describes the synthesis of superparamagnetic magnetite nanoparticles (SPMNs) and corresponding silica coated SPMN nanocomposite particles. Two different routes for the preparation of SPMNs based on chemical co-precipitation methods are reported. The surface modification of the silica coated SPMNs was done with inorganic tetraethyl orthosilicate (TEOS) and subsequently functionalized with free amine trimethoxysilane ligands, 3-(trimethoxysilyl) propylamine and N-[3-(trimethoxysilyl) propyl] ethylene-diamine.

2.1 Chemicals and reagents

All the chemicals were purchased from Aldrich and used without further purification. High purity deionized water (Milli Q, 18 M Ω cm) was deoxygenated by bubbling with pure N₂ gas for 40 min prior to use. Analytical grade ferric chloride hexahydrate (FeCl₃·6H₂O > 99%) and ferrous sulphate heptahydrate (FeSO₄·7H₂O > 99%), ammonium hydroxide (NH₄OH, 25 % in water) was used for magnetite nanoparticle synthesis. Citric acid, absolute ethanol (C₂H₅OH, 99.5%), tetramethyl ammonium hydroxide (TMA, 95%) tetraethyl orthosilicate (TEOS, 99.9%) were used for the coating of magnetite with silica based on the method by van Ewijk.^[82] Hydrochloric acid (HCl, 37 %) and sodium chloride were used without further purification.

2.2 Synthetic procedures

2.2.1 Synthesis of SPMNs

The SPMNs were prepared using the method already described in *Chapter One*, based on the chemical co-precipitation of Fe²⁺_(aq) and Fe³⁺_(aq) by addition of a concentrated solution of ammonium hydroxide (25 % NH₄OH) to a mixture of iron salts with a molar ratio of Fe²⁺ : Fe³⁺ = 1 : 2. Various published routes were explored for the synthesis of SPMNs using the conventional co-precipitation methodology with some modifications to select the best method.^[63,67,80,96,103-108] However, only the two experimental procedures (route A and B) that yielded the best results are reported here (*section 2.2.1.1 and 2.2.1.2*).

2.2.1.1 Route A – synthesis of SPMNs under anaerobic conditions

All the synthesis steps were carried out by passing N₂ gas through the solution medium to prevent possible oxidation during the operations. A typical preparation was as follows: A 25 mL of 25 % NH₄OH solution was added to a suspension containing 8.4 g FeCl₃.6H₂O and 3.07 g FeSO₄.7H₂O dissolved in 400 mL deoxygenated deionized water (Milli Q, 18 MΩ cm) with vigorous stirring at 35 °C for 30 minutes under nitrogen. The color of the mixture turned from orange to black immediately, suggesting the formation of SPMNs. The black precipitated powder was readily isolated by applying an external magnetic field (~0.35 T), and the supernatant was removed from the precipitate by decantation. Deoxygenated de-ionized water was used to wash the powder several times (four times at least) *via* magnetic decantation.

2.2.1.2 Route B – synthesis of SPMNs under aerobic conditions

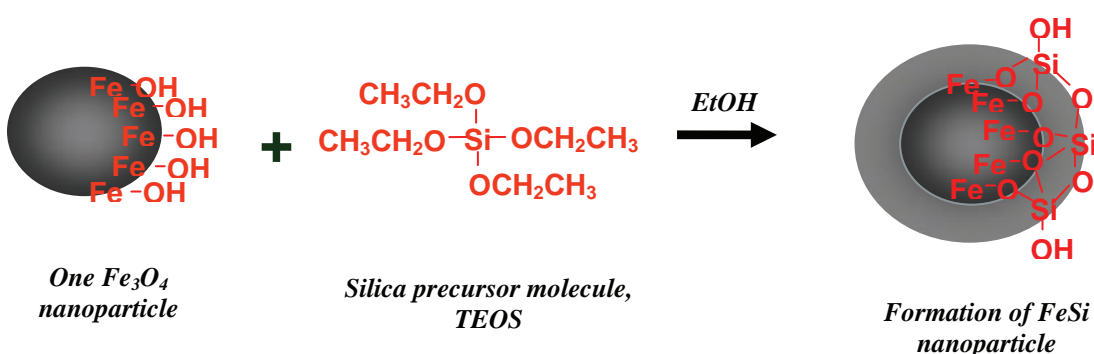
An alternative route for synthesis of SPMNs was investigated in which nitrogen gas was not passed through the reaction medium during any time of the synthesis. The same methodology was used, based on the addition of 25 % NH₄OH solution to an aqueous mixture of ferric and ferrous salts at a fixed temperature. A typical preparation was as follows: A 5 mL of 25 % NH₄OH solution was added to a suspension containing 1.05 g FeCl₃.6H₂O and 0.54 g FeSO₄.7H₂O which were dissolved in 25 mL deoxygenated deionized water (Milli Q, 18 MΩ cm) under nitrogen and vigorously stirred at 35 °C for 30 minutes. As was done in route A, the resulting black precipitate was washed several times with deoxygenated de-ionized water and separated *via* magnetic decantation. The full characterization of these materials is presented in *Chapter Three*.

2.2.2 Synthesis of silica-coated SPMNs

The Stober sol-gel silica composite synthesis method used to coat the SPMNs was based on the method by van Ewijk.^[38,82] After the washing procedure of the SPMNs, 500 mL 0.01 M citric acid solution was added to the SPMNs suspension and 2 – 3 mL tetramethyl ammonium hydroxide (TMA) solution added to increase the pH to approximately 7. No phase separation was observed on exposing the suspension to a strong magnet for 90 minutes indicating that a stable aqueous-based ferrofluid was obtained. The concentration of the SPMNs suspension was approximately 1.8 g L⁻¹. An aliquot was collected for electron microscopy analysis. 160 mL of the SPMN suspension was added to 268 ml ethanol, 72 mL MQ water and 18 mL 25 % NH₄OH

solution. 0.4 mL tetraethyl orthosilicate (TEOS) was added to this mixture and stirred with a mechanical agitator. After 24 h, a further 0.7 mL was added to the suspension and stirred for a further 2h. The silica-coated particles obtained were then washed with an 80 % ethanol-water (v/v) solution and the excess liquid removed while retaining the SPMNs *via* magnetic decantation. The silica-coated SPMNs were dried by evaporation of the solvent at room temperature.

For simplicity, the silica-coated SPMNs will be referred to as FeSi nanoparticles. A simplified representation of the formation of silica-coated SPMNs is illustrated in *Scheme 5*.



Scheme 5. Illustration of silica coating procedure onto surface of SPMN.

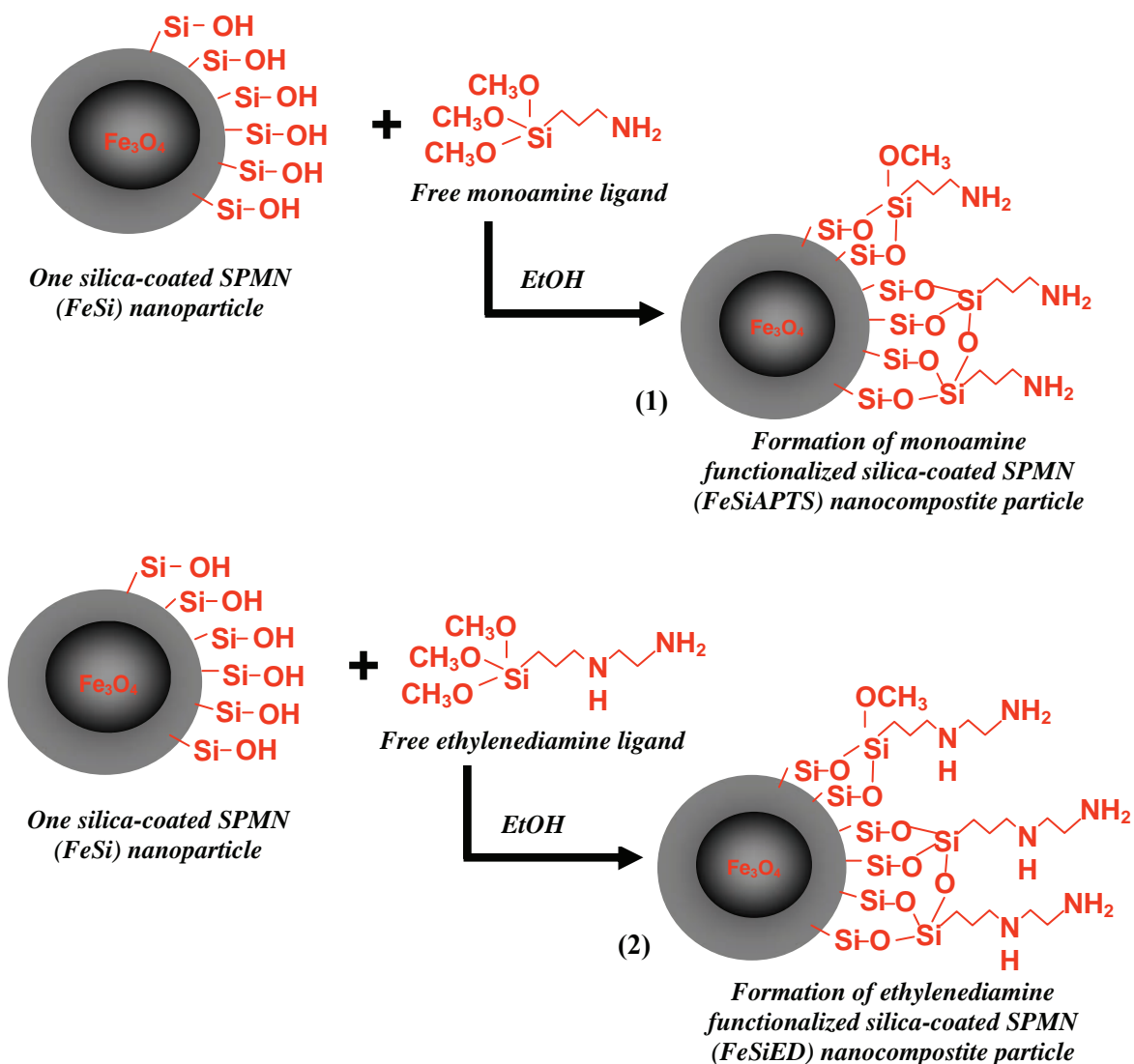
In the sol-gel process reported above, the hydrolysis of the silica precursor (TEOS) in the presence of a base produces silanol (Si-OH) entities, which on further condensation produces a sol.^[84,89] Hydrolysis and condensation are simultaneous processes. In these basic conditions, condensation is accelerated relative to hydrolysis reactions and siloxane linkages (Si-O-Si) are formed. Thus, a highly branched silica network with ring structure was formed. For the purpose of our work, SPMNs were coated with silica to prevent them from agglomeration but also to avoid possible slow dissolution when SPMNs are exposed to acidic solutions.

2.2.3 Surface functionalization of silica-coated SPMNs with trimethoxysilyl alkylamines

The silica surface of silica-coated SPMNs (FeSi) was functionalized with amine trimethoxysilane ligands *via* a methanolysis reaction (*Scheme 6*).^[12,28,38] The ligand immobilization procedure was typically as follows: 60 mg of FeSi particles were re-suspended in 600 μ L ethanol (5 – 10 mL solvent/g FeSi) followed by addition of the suspension 1.7 mmol free amine ligand per gram FeSi particles. The amine trimethoxysilane ligands used in this study for surface functionalization were

3-(trimethoxysilyl) propylamine (APTS) to yield monoamine silica-coated SPMN nanocomposite material; N-[3-(trimethoxysilyl) propyl] ethylenediamine (ED) to yield diamine silica-coated SPMN nanocomposite material, respectively. After stirring for 48 h, the residual reagents were removed by washing the mixture with an 80 % ethanol-water (v/v) solution *via* magnetic decantation and the material dried by evaporation of the solvent at ambient temperature.

The amine-functionalized silica-coated SPMN nanocomposite materials will be referred to as **(1)** FeSiAPTS and **(2)** FeSiED, to denote the monoamine functionalized and the diamine functionalized silica-coated SPMNs, respectively. The summary of the surface functionalization to yield **(1)** FeSiAPTS and **(2)** FeSiED nanocomposite materials is shown in *Scheme 6* below.



Scheme 6. Immobilization of free amine-containing ligands onto silica-coated SPMNs.

The materials (1) FeSiAPTS and (2) FeSiED were fully characterized and results are presented in *Chapter 3*. Also, they were tested as potential magnetic ion-exchangers for precious metal removal from acidic solutions. The results of these investigations are presented in *Chapter 4*.

2.3 Analysis and measurements

2.3.1 Transmission Electron Microscopy

Particle size and morphology was determined by Transmission Electron Microscopy (TEM), using a JEM 1200EXII model (JEOL, Japan) microscope. In general, an accelerating voltage of 120 kV was used throughout. A drop of sample was placed on a carbon-coated 200 mesh copper grid, followed by drying at ambient conditions before it was attached to the sample holder on the microscope. The mean diameter size-distribution was determined by measuring more than 150 particles from TEM images using *Image J*, a public domain image processing program.^[109]

2.3.2 Powder X-Ray diffraction

Structural properties of SPMN powders obtained were investigated by XRD with a Siemens D8 Advance diffractometer using Cu K α radiation ($\lambda = 1.540 \text{ \AA}$) operated at 40 kV and 30 mA. XRD patterns were recorded in the range $10 - 80^\circ (2\theta)$ with a scan step of 0.02° . The average crystallite size ($\langle D \rangle$, \AA) was calculated from line broadening analysis using the Debye-Scherrer formula.^[42,110] For sample preparation, a portion of the SPMN (superparamagnetic Fe $_3$ O $_4$ nanoparticles) was allowed to completely dry at room temperature before analysis.

2.3.3 Vibrating Sample Magnetometry

The magnetization measurements were directly performed on a predetermined volume of SPMNs stabilized in an organic based, oleic acid/kerosene ferrofluid system using a LDJ 9600 Vibrating Sample Magnetometer (VSM) operating at room temperature. A known volume of the sample (determined by weighing the sample holder before and after insertion of the sample and using the density of the fluid) was placed into the VSM sample holder. A maximum field of approximately 1.3 kA/m was used. Densities of the samples were determined using an Anton Paar AP DMA 38 density meter where the ferrofluid is injected into a U-shaped tube housed in a chamber for temperature regulation. The density is determined at 20°C . The U-shaped tube vibrates at a certain frequency. Depending on the density of the inserted sample, this induces frequency changes from which the density may be calculated.

2.3.4 Surface area measurements

The specific surface area (SSA) of SPMNs and the FeSi samples degassed at 300°C for approximately 24 h, was determined by the BET method^[111,112] with a Micrometrics ASAP 2010 (Accelerated Surface Area and Porosity System) using nitrogen as an adsorbent. Each degassed sample (0.1 – 0.4 g) was weighed accurately to four decimal places and placed in a sample tube. Analysis was performed using an automatic multi-point adsorption programme, measuring the volume of nitrogen adsorbed by the sample at a range of N₂ pressures.

2.3.5 Fourier Transform Infrared Spectroscopy

FTIR spectra of the nanoparticles were collected on a NEXUS 870 Fourier Transform spectrometer (Thermo Nicolet Corp.). A transmittance mode using at least 20 acquisitions per sample were used. Prior to compacting, all samples and KBr were dried at 95 °C for 48 h. Each sample was thoroughly mixed and crushed with KBr using a mortar and pestle. The mixture was pressed into pellets using 8 tons/cm² of pressure for 3 minutes (three times) to form the KBr pellet. The FT-IR spectra were collected after 64 scans of the region between 400 and 4000 cm⁻¹.

2.3.6 Thermogravimetric analysis

Thermogravimetric analysis (TGA) was carried out with a Q500 TA instrument in the temperature range 0 – 590 °C, using Pt crucibles with typically 3-5 mg dried samples, under dynamic N₂ atmosphere (50 mL/min) and heating rate of 10 °C min⁻¹. Samples were weighed in a sample compartment that was dried and flushed with nitrogen.

2.3.7 Elemental composition analysis

Phase compositions were quantified by using a Leo® 1430VP Scanning Electron Microscope (SEM) equipped with an Oxford Instruments® 133KeV detector and Oxford INCA software. With the attachment of an energy dispersive X-ray spectrometer (EDS), the chemical or elemental composition of the materials was obtained. The samples were mounted on a small stub with double sided carbon tape so that it could be handled easily. The sample on the stub was then coated with a thin layer of gold and mounted on the SEM stage in a chamber under high vacuum. The beam conditions during the quantitative analyses were 20 KV and approximately 1.5 nA, with a working distance of 13 mm and a specimen beam current of -3.92 nA.

2.3.8 Inductively coupled plasma – atomic emission spectroscopy

A Varian Liberty Series II spectrometer was used to measure the concentrations of Au, Pd, Pt and Fe in solutions using the general ICP conditions listed in *Table 1*. Standards (traceable to NIST) were matrix matched to acid concentrations of the samples. After calibration and quality check analysis to verify accuracy of standards, samples were analyzed, without dilution. Only samples in excess of 100 ppm were diluted to approximately similar matrix composition as the standards.

Table 1. ICP-AES operating conditions for the determination of solution-phase Au, Pd, Pt and Fe in influents and effluents

Parameter	Setting
Generator power	1300 W
View mode	Radial
View height	15 mm
Plasma	Argon
Shear gas	Argon
Gas flow: plasma	15 ml min ⁻¹
Gas flow: auxiliary	1.5 ml min ⁻¹
Gas flow: nebulizer	1.5 ml min ⁻¹
Sample aspiration rate	2 ml min ⁻¹
Detector	PMT
Emission line: Au	242.795
Emission line: Pt	214.423
Emission line: Pd	340.458
Emission line: Fe	259.94
Rinse delay	15 s
Read	Peak area
Replicate read time	2 s
Number of replicates	3

2.4 Metal adsorption experiments

The removal of single-metal $[\text{AuCl}_4]^-$, $[\text{PdCl}_4]^{2-}$ and $[\text{PtCl}_4]^{2-}$ species from chloride-rich acidic solutions was investigated. These precious metal species readily form $[\text{MCl}_4]^{n-x}$ ($\text{M} = \text{Au}, \text{Pd}, \text{Pt}$) anionic complexes in acidic chloride-rich solutions, where x is the number of chloride ions bound to the metal centre and n is the oxidation state of the metal ion.^[113,114] All the adsorption studies were carried out by batch sorption experiments at room temperature ($21 \pm 1^\circ\text{C}$) and steady state conditions for varying contact times.

2.4.1 Chemicals and reagents

Stock solutions of $[\text{AuCl}_4]^-$, $[\text{PdCl}_4]^{2-}$ and $[\text{PtCl}_4]^{2-}$ were prepared from the precious metal salts $\text{HAuCl}_4 \cdot x\text{H}_2\text{O}$, K_2PdCl_4 , K_2PtCl_4 , and the required amount of standardized HCl solution. Hydrochloric acid (HCl, 37%) and sodium chloride were purchased from Aldrich and used without further purification. High purity water with a resistivity of $18 \text{ M}\Omega \text{ cm}$ was used.

2.4.2 Batch sorption experiments

Adsorption experiments were performed by putting into contact known amounts (by mass) of the synthesized magnetic materials with aqueous solutions of $[\text{AuCl}_4]^-$, $[\text{PdCl}_4]^{2-}$ and $[\text{PtCl}_4]^{2-}$ in various concentrations of hydrochloric acid solutions using a Labcon horizontal rotary shaker (110 rpm) at room temperature ($21 \pm 1^\circ\text{C}$). After contact for a desired time, the aqueous phase was separated from the solid phase by applying a strong external magnetic field (magnetic settlement). The concentration of metal ions in the supernatant solution was determined by Inductively Coupled Plasma Atomic Emission Spectroscopy (ICP-AES) with a Liberty Series II spectrometer (Varian, Australia) using a linear calibration method. The iron content in the aqueous phase was also determined in order to investigate the influence of resin dissolution on metal adsorption.

The amount of adsorbed metal, q , was calculated by the mass balance of the metals before and after adsorption, as illustrated by equation 7.^[115]

$$q = (C_i - C_{\text{aq}}) \frac{V}{W} \quad [\text{mmol/g}] \quad (7)$$

and the equation

$$\text{metal ion adsorbed} = \frac{(C_i - C_{\text{aq}})}{C_i} \times 100 \quad [\%] \quad (8)$$

with the distribution coefficient (K_d) defined as

$$K_d = \frac{(C_i - C_{\text{aq}})}{C_{\text{aq}}} \times \frac{V}{W} \quad [\text{ml/g}] \quad (9)$$

Where C_i represents initial metal ion concentration (mmol/L), C_{aq} metal ion concentration in the aqueous solution (mmol/L), V volume of the aqueous phase (mL) and W weight of the oxide (g).

The effect of various aspects, such as contact time, the initial metal ion concentration, different masses of adsorbent, and the hydrochloric acid concentration, on the extent of precious metal removal was investigated. Furthermore, the effect of chloride ion concentration on the adsorption of metal ions was investigated by the addition of the required amount of sodium chloride to the aqueous phase at a known HCl concentration.

Chapter Three

Characterization of SPMNs and Nanocomposite Materials

This chapter focuses on the characterization of the SPMNs, the silica-coated SPMNs and the amine functionalized silica-coated SPMNs. The crystallinity and morphology were investigated by X-ray powder diffraction (XRD) and Transmission Electron Microscopy (TEM) analysis. The SPMN-silica interface was studied by Fourier-Transform Infrared spectrometry (FTIR) and Thermogravimetric analysis (TGA). The relative ligand concentrations immobilized onto the amine functionalized silica-coated SPMNs are determined by elemental analysis and the material compositions are confirmed by Energy Dispersive X-ray spectroscopy (EDX) analysis. The magnetic properties of the SPMNs were investigated by Vibrating Sample Magnetometry (VSM).

3.1 Results and Discussion

3.1.1 Structural characterization by X-ray diffraction

The crystallinity and phase purity of the synthesized materials were determined by powder X-ray diffraction (XRD). *Figure 6* shows the XRD diffractograms of the unfunctionalized SPMNs and of the silica-coated SPMN (FeSi) nanocomposite materials. The XRD shows that the resulting powders obtained are consistent with the expected composition of Fe_3O_4 . Shown in the inset is a XRD pattern from literature.^[116] The positions and relative intensities of the diffraction peaks for both patterns (*Figure 6 (a) and (b)*) were also matched with the standard XRD data for bulk Fe_3O_4 (JCPDS file No. 01-075-1372). It was found that these patterns were in good agreement with the database fingerprint pattern of Fe_3O_4 .

The XRD peaks of the two materials can be indexed into a spinel cubic lattice type with lattice parameter of 8.39 Å and 8.41 Å for Fe_3O_4 and FeSi nanomaterials, respectively. It is found that the particles consist mainly of magnetite (Fe_3O_4) with a small amount of maghemite ($\gamma\text{-Fe}_2\text{O}_3$) phase. It cannot be ascertained from the XRD patterns to what extent the further oxidized hematite ($\alpha\text{-Fe}_2\text{O}_3$) phase exist in the sample because of similar lattice type and lattice parameters.^[42]

Although it is clear that the bulk of the particles consist mainly of Fe_3O_4 phase, there is some evidence of other impurities in the samples, labeled as ‘*’ in the XRD pattern in Figure 6. The impurities can be attributed to the hematite ($\alpha\text{-Fe}_2\text{O}_3$) phase.

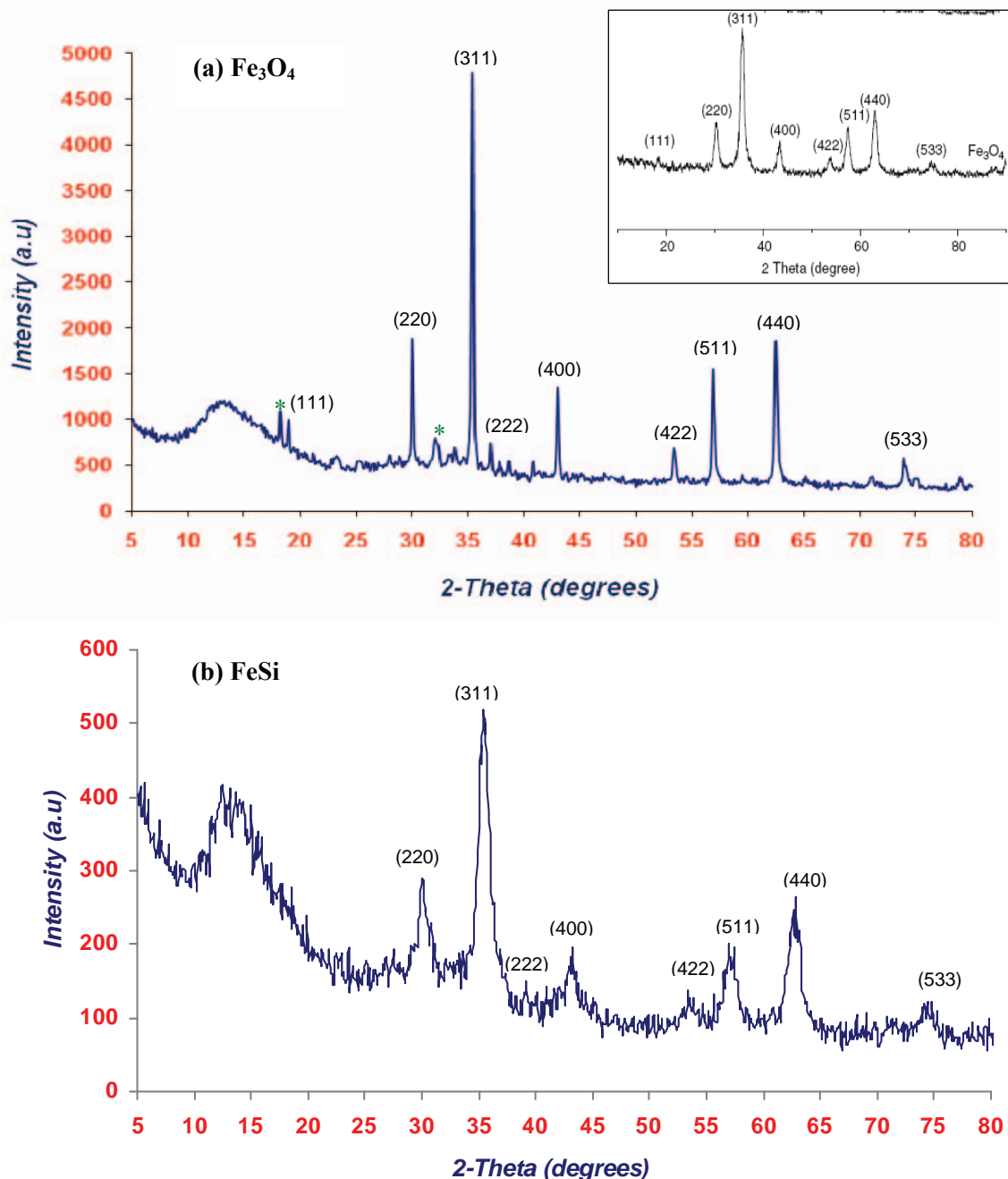


Figure 6. Indexed X-ray diffractograms of (a) uncoated Fe_3O_4 and (b) FeSi nanomaterials with different particle sizes. ‘*’ indicates lines from $\alpha\text{-Fe}_2\text{O}_3$ impurity phase(s). The relative intensity of the patterns is related to the degree of crystallinity of the materials. The obtained spectra were corrected for instrumental line broadening and refined with the XRD analysis program EVA.^[128] Shown in the inset is a reference XRD pattern.^[116]

The relative intensity of the patterns is related to the degree of crystallinity of the materials. The sharp peaks observed in *Figure 6 (a)* indicate a high degree of crystallinity for the SPMNs. Once the SPMNs have been coated with amorphous silica, the sample was found to be less crystalline, as indicated by the relative intensity in *Figure 6 (b)*. Also there is a higher signal-to-noise ratio arising from the lower crystallinity. The broadening of XRD peaks could be attributed to the decrease in crystallite size. Therefore, if the crystallites of the powdered materials are very small, the peaks of the XRD patterns will be relatively broad. Thus on inspection of the XRD diffractograms obtained, it was expected that the size of crystalline nanoparticle cores of the FeSi nanomaterials to be smaller than the crystalline nanoparticle cores of the uncoated SPMNs. This was indeed found to be the case. The reason for these occurrences is not well understood and needs further investigation, but it is assumed that the silica layer surrounding the SPMN cores prevents the determination of more accurate crystallite size. It is important to note that the size estimations made here is only based on the crystalline SPMN core and not the total diameter including the silica coating of FeSi nanomaterials.

The average crystallite size was calculated using the Debye-Scherrer equation,^[42,110]

$$\langle D \rangle = D_{hkl} = \frac{k\lambda}{\beta \cos \theta} \quad (10)$$

where $k = 0.8 - 1.39$ (usually close to 1, *e.g.* 0.9)

λ = wavelength of radiation, for $\lambda_{Cu} = 1.54056 \text{ \AA}$

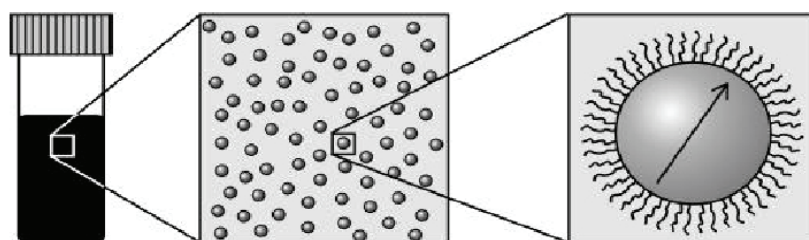
β = full width at half height (FWHM)

θ = the position of the maximum diffraction

The average crystallite size ($\langle D \rangle$, \AA) as calculated from line broadening analysis using the Debye-Scherrer formula (*equation 10*) was found to be $5.27 \pm 0.70 \text{ nm}$ and $3.88 \pm 1.32 \text{ nm}$ for the SPMNs and silica coated SPMNs nanocomposite materials, respectively.

3.1.2. Transmission electron microscopy analysis

Transmission electron microscopy (TEM) analysis was used to estimate the uncoated SPMN size, morphology, and state of agglomeration *in situ*. This was done by modifying the SPMNs with citric acid in order to stabilize them in liquid media and in the process produced aqueous based SPMN ferrofluid (refer to Chapter 2). TEM analysis of silica-coated SPMNs was also done to investigate the extent of silica coating on the SPMNs. The principle idea of TEM analysis of the uncoated SPMNs is shown in Scheme 7, where each SPMN is modified with surfactants.



Scheme 7. TEM analysis of SPMN samples illustrating the effect of the surfactant steric stabilizers modified onto the SPMNs to enhance their stability in liquid media.

3.1.2.1 Morphology and size of SPMNs

The TEM micrographs of the SPMNs prepared from co-precipitation methods under aerobic conditions (route B) and anaerobic conditions (route A) are shown in *Figure 7 (a) and (b)*, respectively. (see section 2.2.1 of Chapter 2). As can be seen in *Figure 7 (a)*, most of the particles prepared by route B appear approximately of spherical shape and are well dispersed. As can be seen in *Figure 7 (b)*, the particles prepared by route A consist almost of perfect single particles, though their morphology was somewhat irregular ranging from triangular to spherical in shape. In both images, each particle was separated from its neighbors by the surfactant (citric acid) adsorbed on the particle surfaces (as demonstrated by *Scheme 7*). It can be seen that the intervals of each neighboring SPMN was found to be uniform. However, in both micrographs (*Figure 7 (a) and (b)*), there is evidence of some degree of moderate agglomeration of the SPMNs. This agglomeration could be attributed to slight instability of the aqueous nanoparticle suspension. Although surfactant molecules enhance the stability of SPMNs in suspension, they could in principle still agglomerate as a result of (1) insufficient or improper surfactant coating on the SPMN surface, (2) when the interparticle forces between individual nanoparticles is high enough to overcome the steric repulsion provided by the surfactant molecules or (3) combination of both

the above mentioned factors. These images were collected 48 h after the suspension preparation, which could have resulted in the loss of SPMN suspension stability with time, thus causing the observed agglomeration.¹ Evidence of colloid instability was the sediment which formed in the vials consisting of the colloidal aqueous SPMN suspensions which were analyzed after 48 h.

The mean diameter and size distribution was determined by measuring more than 150 individual SPMNs from the TEM micrographs obtained using *Image J*, a public domain image processing program.^[109] The corresponding histograms of the respective size-distributions of each TEM micrograph is shown in *Figure 8 (a) and (b)*. Monodispersed SPMNs with an average particle diameter of 9.04 ± 1.23 nm for route B and 5.20 ± 0.66 nm for route A, respectively were obtained. The experimental results thus show that flowing nitrogen gas through the aqueous reaction medium as was done in route A, not only protects against critical oxidation of the SPMNs but also reduces the particle size when compared with route B, without removing the dissolved oxygen in the reaction medium. As was found in this study the SPMN size was reduced from approximately 9 nm (route B - aerobic conditions) to 5 nm (route A - anaerobic conditions) as shown by the size distribution histograms in *Figure 8 (a) and (b)*.

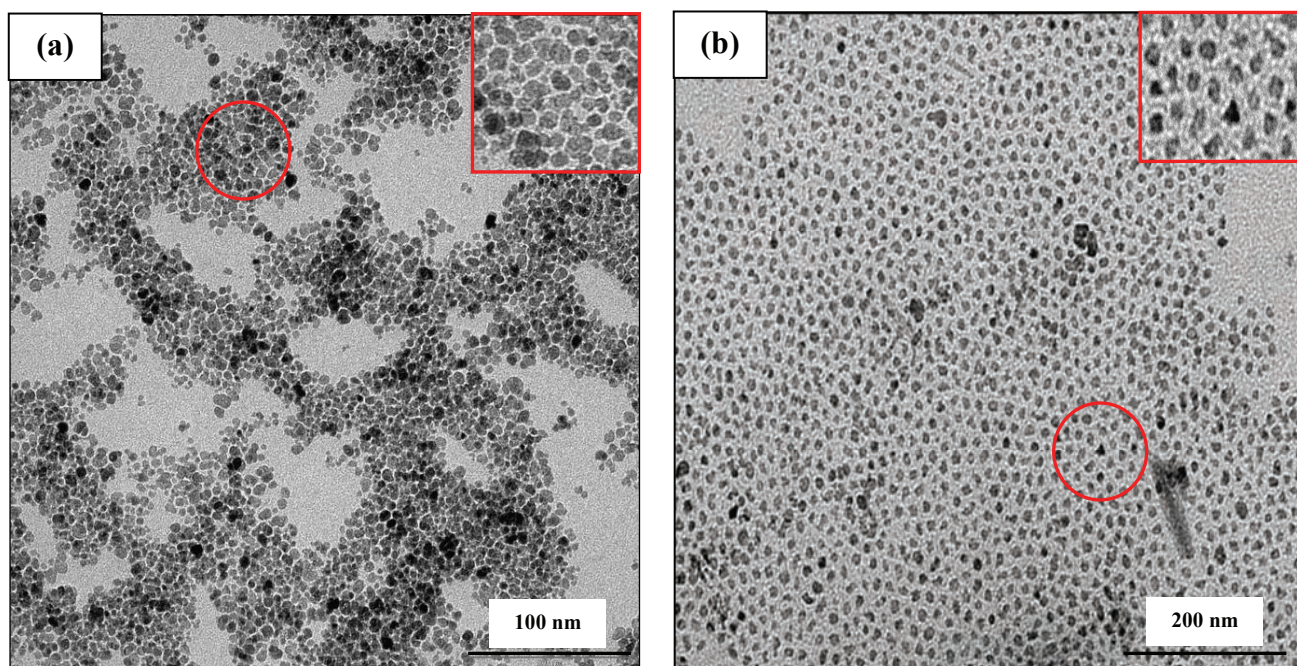


Figure 7. TEM micrographs of SPMNs prepared under (a) aerobic and (b) anaerobic conditions. The inset shown in each micrograph is a magnification illustrating the morphology of the SPMNs.

¹ These TEM analyses were not done at Stellenbosch University, so this delay was unavoidable.

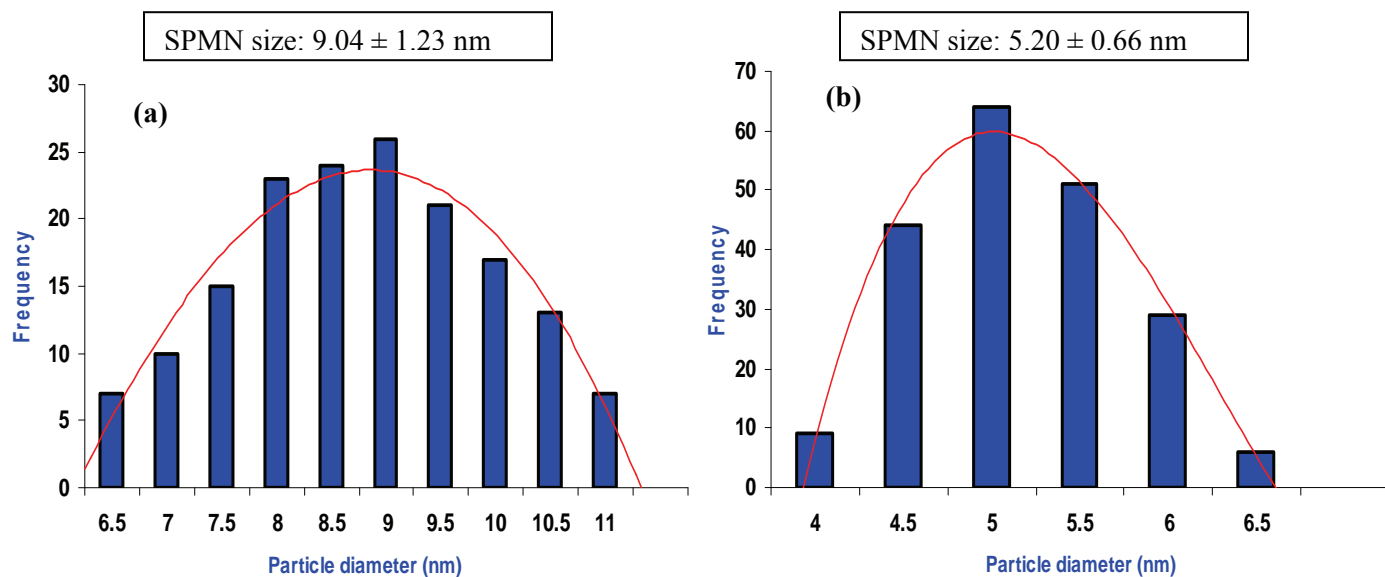


Figure 8. Size distribution histograms of SPMNs synthesized under (a) aerobic and (b) anaerobic conditions. The histograms correspond to the TEM micrographs shown in Fig. 7.

3.1.2.2 Morphology and size of silica-coated SPMNs

The silica coating around the SPMNs was also examined using TEM. The SPMNs used as seeds in the silica coating procedures were those obtained from the synthetic route B. The TEM micrographs of the silica-coated SPMNs (FeSi nanoparticles) prepared using different volumes of TEOS precursor are shown in Figure 9 (a – c). The TEM micrographs (Figure 9 (a – c)) were obtained using 0.4 mL, 0.6 mL, and 0.8 mL TEOS precursor, respectively as described in Chapter 2, section 2.2.2. According to the micrographs, the morphology of the obtained FeSi nanoparticles varied from spherical to irregular with clear evidence of SPMN aggregation and silica cluster formation as indicated by the red arrows in the micrographs. In Figure 9 (a) and (b), two regions with different electron densities can be distinguished for the FeSi nanoparticles: an electron dense region which presumably corresponds to SPMN core(s), and a less dense, more translucent region surrounding these cores, that is likely to be the silica coating shell. This might be described as SPMN-silica core-shell structures. Thus, Figure 9 (a) and (b) illustrates that a silica layer was formed around the small aggregates of several SPMNs. The formation of small aggregates of SPMNs resulted from the magnetic dipolar interaction among the individual SPMNs. Coating such aggregates with a silica layer could reduce the magnetic dipolar interaction and further promote the stability of SPMNs.^[96]

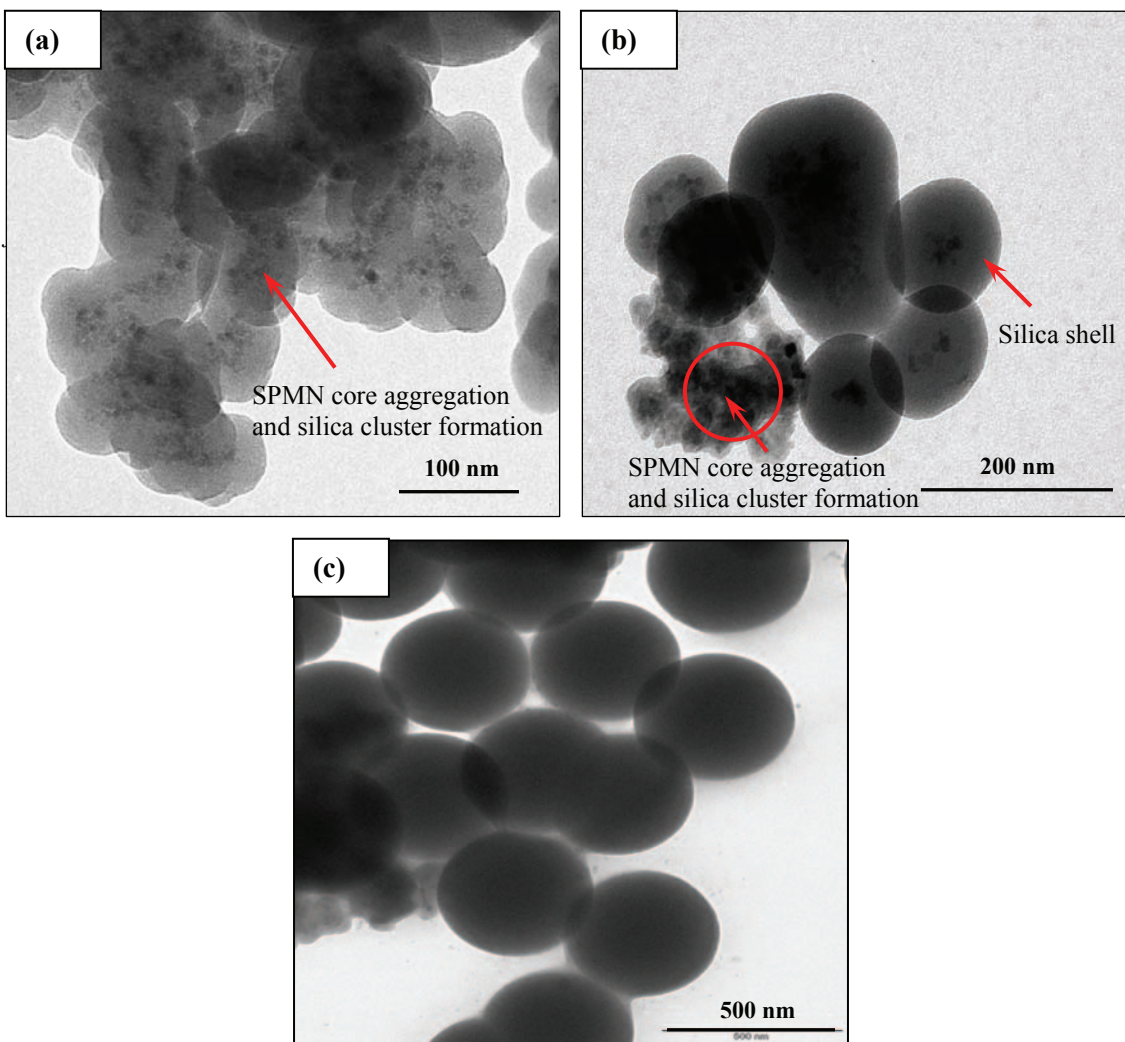


Figure 9. TEM micrographs of silica-coated SPMNs illustrating morphology, size, aggregation and cluster formation. Different volumes of TEOS precursor added: (a) 0.4 mL, (b) 0.6 mL, and (c) 0.8 mL.

It was very difficult to evaluate the thickness of the silica coated shell because of silica cluster formation and due to the poor contrast between this amorphous protective shell and the cores of the SPMNs. Therefore, it was not possible to construct a reliable size distribution histogram of the formed FeSi nanoparticles. However, *Figure 9 (a) and (b)* suggested that the silica coated shell was fairly homogeneous and the thickness was estimated to be in the range 80 – 120 nm.

As can be seen from *Figure 9 (a – c)*, there is a distinct difference in the size of the FeSi nanoparticles obtained. It was found that with increased volumes of the TEOS precursor used during the silica coating procedure from 0.4 mL to 0.8 mL, the thickness of the silica shell increased.

When the thickness of the silica coated shell increased, the FeSi nanoparticles changed from aggregates and clusters to discrete and much larger monodispersed particles. This can be seen by the TEM micrograph in *Figure 9 (c)*, which yielded almost micron sized, spherical FeSi nanoparticles. In *Figure 9 (c)*, the presence of SPMNs could not be seen as a result of relatively thick and much denser outer silica coated shell.

Important factors that might be responsible for the ill-defined FeSi nanoparticle structures in *Figure 9 (a – c)*, are:

- (i) The amount of TEOS silica precursor,
- (ii) The amount of catalyst (NH₄OH), and
- (iii) The polarity of the reaction media, used during the silica coating procedure.

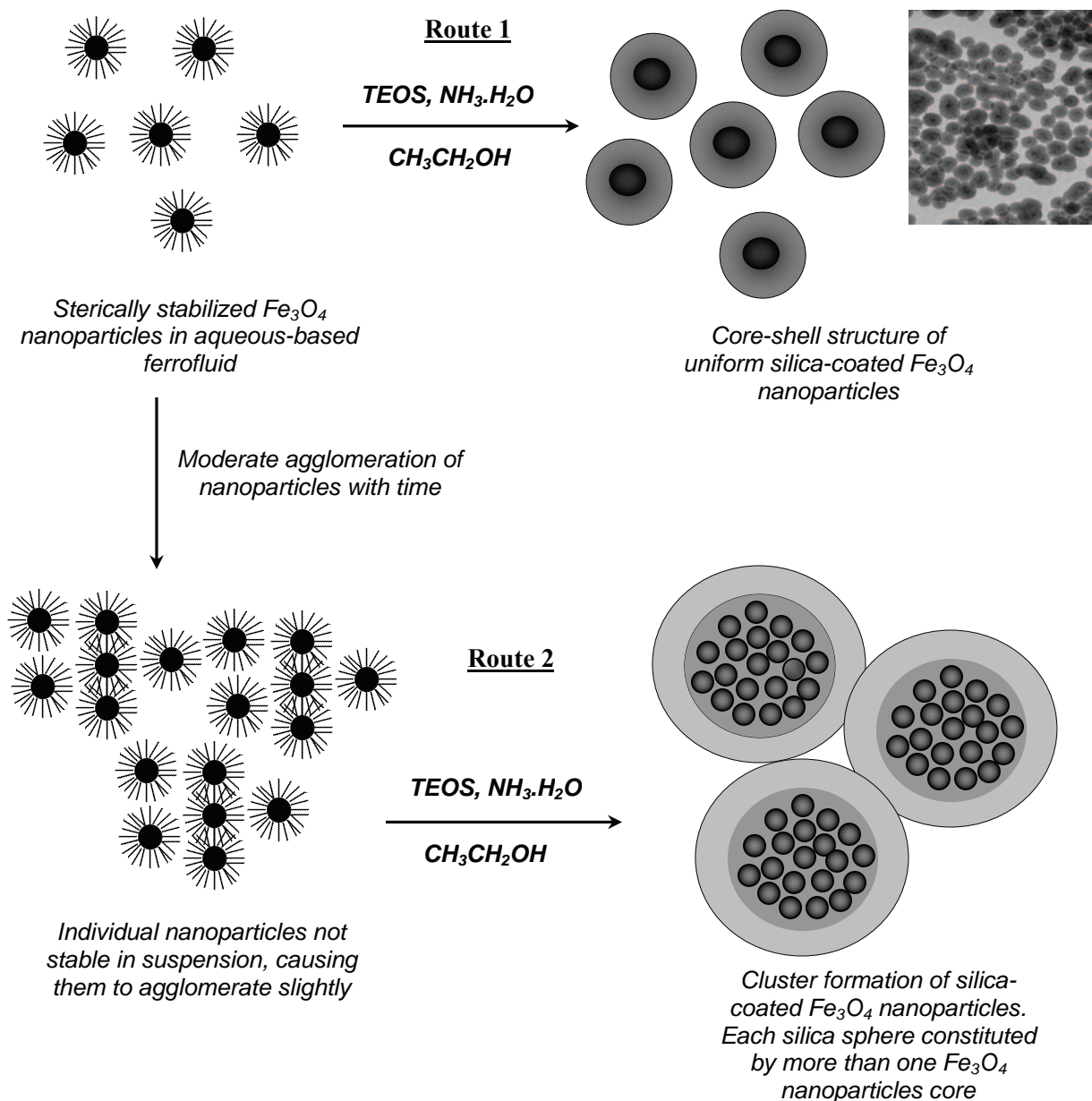
As shown by our results, with an increase in the amount of TEOS precursor used, the morphology of the FeSi nanoparticles varied and the size drastically increased as the relative concentration of TEOS precursor was increased. As has been reported by Lu *et al.*,^[84] the thickness of the silica shell could be controlled by varying the concentration of TEOS precursor. Thus, too much TEOS precursor could have resulted in the formation of the relatively thick silica coated shell and also contributed to the observed silica cluster formation.

The amount of catalyst (NH₄OH) used to promote the hydrolysis of TEOS precursor, could have an effect on aggregation and silica cluster formation. Too much NH₄OH or even too rapid addition might increase the hydrolysis rate and cause almost immediate cluster formation and dense silica coated shells (*Figure 9 (c)*). It would be more favorable if the silica is grown *via* slow hydrolysis of TEOS in order to increase the chances of obtaining properly dispersed FeSi nanoparticles with well-defined SPMN-silica core-shell structures.

According to a previous report, the polarity of the reaction media has an effect on the zeta potential of SPMNs.^[118] In that study they found the formation of ultrafine silica particles and attributed it to the relatively strong polarity of methanol used during the silica coating procedure. Therefore, SPMNs with a higher zeta potential would disperse more easily and stably, and is more favorable for preparation of silica-coated SPMNs with more regular morphology. In our study, we only used ethanol as the reaction media. As compared to the above literature, the morphology of the obtained FeSi nanoparticles was more irregular and even larger clusters of FeSi SPMNs were formed.

There are essentially two possible paths in the silica coating procedure of SPMNs that can lead to either (1) nicely separated, monodispersed silica coated SPMNs with core-shell structure or as was found in our case (2) SPMN agglomeration and silica cluster formation. Illustrated in

Scheme 8 is the two possible routes as mentioned above during silica coating formation. Route 1 illustrates the formation of nicely separated monodispersed FeSi nanocomposite materials with core-shell structure. Route 2 illustrates more or less what happened in our silica coating process, ill-defined and agglomerated SPMN-silica nanocomposite materials.



Scheme 8. Simplified representation of the silica-coating of the SPMNs illustrating the ideal (top route)^[27] and non-ideal (bottom route) situation during the coating procedure.

3.1.3 Elemental composition analysis

3.1.3.1 Energy dispersive X-ray spectroscopy

To confirm the presence of the main elements in the synthesized materials, an elemental composition analysis was done by energy dispersive X-ray spectroscopy (EDX). Using this technique, the elemental composition of the materials was obtained with high resolution. EDX analysis data confirms that the main components of the materials **(1)** and **(2)** are Fe, Si, O, N and C (*Figure 10*). The presence of silica in the samples confirmed the protective amorphous silica coating for the SPMNs and the presence of C and N in particular confirmed the functionalization of the silica-coated SPMN nanocomposite materials with the amine ligands.

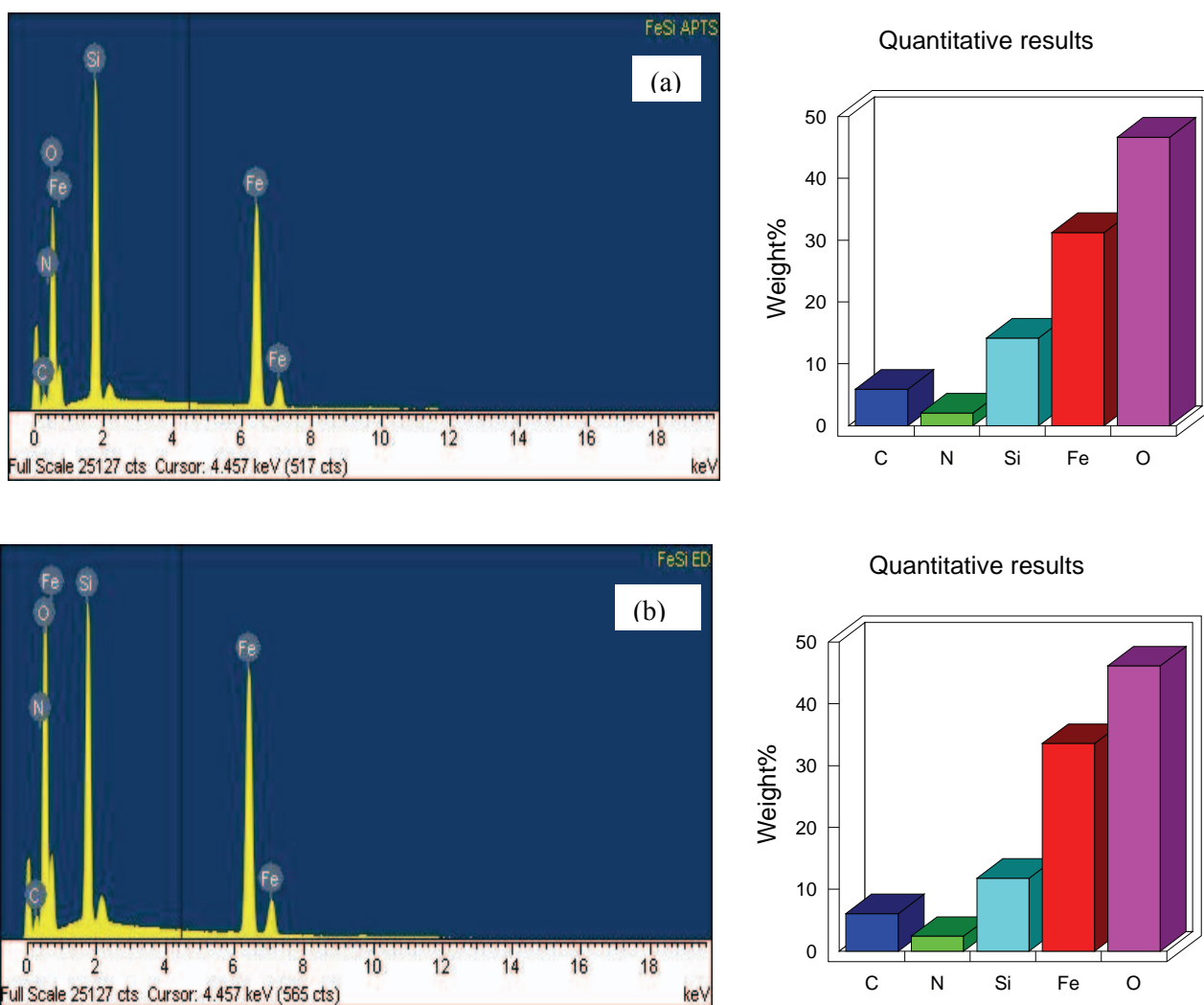


Figure 10. EDX analysis images of the amine-functionalized silica coated SPMN materials. (a) material **(1)** FeSiAPTS, and (b) material **(2)** FeSiED.

3.1.3.2 Elemental (C, H, and N) analysis

Surface modification of SPMNs and silica surfaces with organosilanes has been extensively studied as discussed in *Chapter 1, section 1.2.5.3*. Through hydrolysis of the alkoxy group (usually methoxy or ethoxy), the silane molecules are attached to the particles surfaces *via* covalent bonding and terminated with functional groups such as amines. In this work, silica-coated SPMNs (FeSi) were functionalized with amine trimethoxysilane ligands to produce magnetic ion-exchanger nanocomposite materials with **(1)** monoamine and **(2)** diamine functionality.^[12,28,38] These materials are presented below in *Figure 11*. For simplicity, these amine functionalized silica-coated SPMNs are referred to as **(1)** FeSiAPTS and **(2)** FeSiED. (*Refer to Chapter 2, section 2.2.3 for experimental procedures*).

Elemental analysis (C, H, and N) was done on these materials in order to determine the amount of amine ligand that was immobilized onto the surface of silica-coated SPMNs (FeSi). The ligand concentrations of materials **(1)** and **(2)** were calculated from the weight percentage of nitrogen, as is generally done while carbon and hydrogen percentages, which are based on this ligand concentration, are given in parentheses (*Tables 2 and 3*). (*Refer to supplementary section A1 for the calculations of the obtained values*). In each table are shown results that were obtained from three sets of analysis of different batches of the same material synthesized under similar experimental conditions. As was observed previously, the ligands are grafted on average, *via* two methoxy groups.^[12,28,101] This was confirmed by our results.

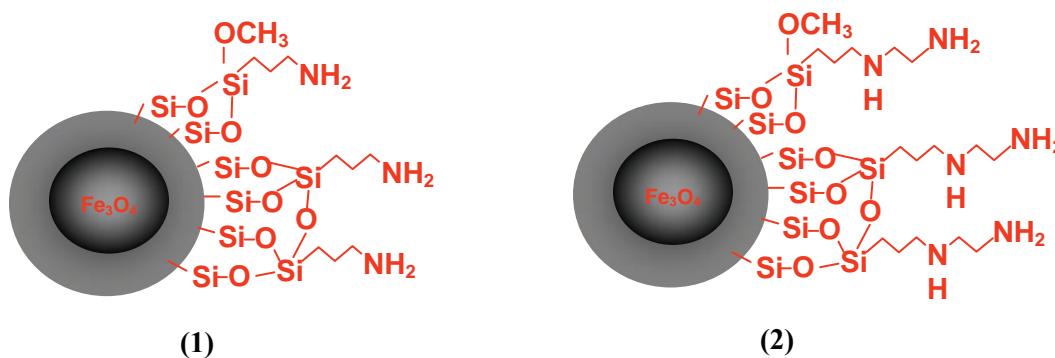


Figure 11. Illustration of the monoamine (1) FeSiAPTS, and ethylenediamine (2) FeSiED functionalized FeSi nanocomposite materials.

Table 2. Elemental analysis results obtained for material (1) FeSiAPTS

% C (calc ^[b])	% H (calc ^[b])	% N ^[a]	Ligand concentration (mmol/g) ^[a]
4.44 (3.53)	3.21 (0.82)	1.03	0.74
3.94 (3.57)	2.37 (0.82)	1.04	0.74
4.23 (3.64)	3.11 (0.84)	1.06	0.77

^[a]Ligand concentration were calculated based on the nitrogen content

^[b]Based on the results of the nitrogen content

Table 3. Elemental analysis results obtained for material (2) FeSiED

% C (calc ^[b])	% H (calc ^[b])	% N ^[a]	Ligand conc. (mmol/g) ^[a]
6.84 (6.71)	3.07 (1.50)	2.61	0.93
6.27 (5.94)	2.68 (1.82)	2.31	0.82
6.06 (6.12)	5.35 (1.37)	2.38	0.85

^[a]Ligand concentration were calculated based on the nitrogen content

^[b]Based on the results of the nitrogen content

From the results, it was observed that the ligand concentration increased with the number of nitrogen atoms in the backbone. An average ligand concentration of 0.75 mmol/g and 0.87 mmol/g for material (1) and (2), respectively, was calculated to be immobilized onto the FeSi materials surface. These values were in direct correlation to the amount of monoamine and diamine ligand that was grafted onto the FeSi surface. The values given in parentheses were the calculated values based on the nitrogen content in each sample. As can be seen, the experimental values obtained for C in each sample correlated well with the calculated values. However, there

were some discrepancies between the experimental and calculated values of the H percentage in each sample. These differences could be attributed to residual water in the samples.

From these results it could be concluded that the FeSi materials were successfully functionalized with the amine ligands and that the immobilization onto the surface occurred *via* two methoxy groups. However, the ligands could also be immobilized onto the FeSi surface *via* all three methoxy groups, depending on the experimental conditions used in this process.

3.1.4 Surface characterization

3.1.4.1 Thermogravimetric analysis

The percent weight loss as a function of temperature was studied by TGA for unfunctionalized SPMNs and for the functionalized silica-coated SPMN materials. The purpose of these studies was to investigate the decomposition of the materials, to gain some structural knowledge, and also to comparatively determine the amount of amine ligands grafted onto the surface of the silica-coated SPMNs. As can be observed from *Figure 12*, the TGA curve of the unfunctionalized SPMNs shows a weight loss over the range 90 – 280 °C of about 3 %. This loss can be attributed to the loss of adsorbed water and dehydroxylation of internal OH groups according the *Scheme 9*.

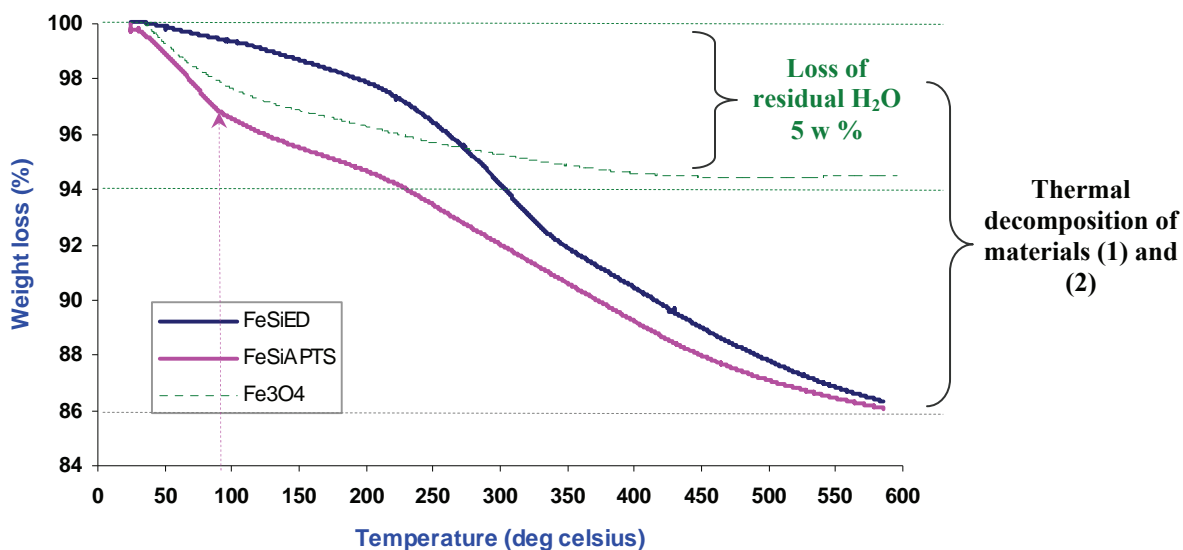
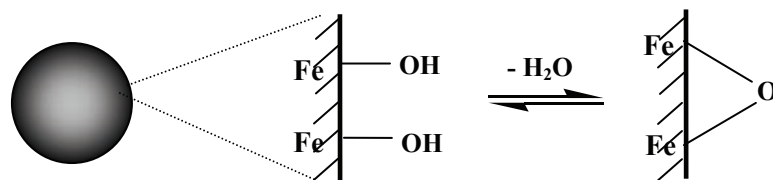


Figure 12. TGA curves of SPMNs, and of materials (1) FeSiAPTS and (2) FeSiED.



Scheme 9. Illustration of the loss of absorbed H_2O from the SPMN surface.

The TGA curves of **(1)** FeSiAPTS and **(2)** FeSiED show two weight loss steps. The first weight loss for **(1)** is over the range 100 – 225 °C which can be due to the loss of residual water (dehydration process) adsorbed physically in the material. For **(2)** there is a weight loss over the range 125 – 250 °C which is due to material decomposition, since there is no evidence of residual water losses (*Figure 12*). The second weight loss step for **(1)** is over the range 225 – 590 °C and for **(2)** over the range 250 – 590 °C. These losses can be ascribed to even further decomposition of the materials. The total weight losses are approximately 10 % and 14 % for **(1)** and **(2)**, respectively.

If assumed that the total weight loss is only due to the amount of amine ligands on the surface of **(1)** and **(2)**, then from the data obtained, the relative amount of monoamine and diamine methoxy silane ligands immobilized onto the surface of the silica-coated SPMN materials was calculated and found to be 0.56 and 0.63 mmol/g for **(1)** and **(2)**, respectively. From the TGA data obtained, we could estimate that the surface of **(1)** was approximately 27.45 % functionalized and that the surface of **(2)** was approximately 30.91 % functionalized with the ligands.

The average ligand concentration obtained from elemental analysis calculations was found to be 0.75 mmol/g and 0.87 mmol/g for **(1)** and **(2)**, respectively (see 3.1.3.2). These discrepancies between the ligand concentration values obtained from the different analysis methods could be due to the differences in pore sizes of the silica-coated SPMNs, ligands fit differently through the pores. As a result, the accessibility of amine groups decreases and accordingly, the ligand concentration. However, it should be pointed out that the results obtained from elemental analysis are much more reliable and therefore these values were accepted as the relative ligand concentrations on the surface of silica-coated SPMNs.

3.1.4.2 Fourier-transform infrared spectroscopy

Fourier transform infrared (FTIR) spectra were acquired to confirm the silica-coating of SPMNs and the subsequent functionalization of these materials with monoamine and diamine methoxysilane ligands. *Figure 13* shows the FT-IR spectra of (a) unfunctionalized SPMNs, (b) monoamine (FeSiAPTS), and (c) diamine (FeSiED) functionalized silica-coated SPMNs. The presence of SPMNs is indicated by the presence of the absorption bands at around 636 cm^{-1} and 474 cm^{-1} . It is known that the FTIR bands at wavenumbers less than 700 cm^{-1} can be assigned to the vibrations of Fe-O bonds of bulk Fe_3O_4 .^[42,119] Both the unfunctionalized SPMNs, FeSiAPTS and FeSiED showed the presence of Fe-O stretching vibrations at 474 and 636 cm^{-1} . Thus, these bands indicate and confirm the presence of SPMNs. Furthermore, the FTIR spectra of the SPMNs (*Figure 13 a*) show the presence of an O-H stretching vibration due to physisorbed water and potentially surface hydroxyls near 3420 cm^{-1} , and an O-H deformation vibration near 1640 cm^{-1} , respectively. The silica network is adsorbed on the SPMN surface by Fe-O-Si bonds. This absorption band cannot be seen in the FT-IR spectrum because it appears at around 584 cm^{-1} and therefore overlaps with the Fe-O vibration of SPMNs. The sharp absorption band at 1100 cm^{-1} is assigned to the stretching vibration of the Si-O-Si groups.^[120,121] The significant features observed for FeSiAPTS and FeSiED are the appearance of the peaks at 3480 and 1642 cm^{-1} . These could be ascribed to the NH_2 stretching vibration and N-H bending mode of free NH_2 groups, respectively. The presence of the anchored propyl groups of FeSiAPTS and FeSiED was confirmed by weak C-H stretching vibrations that appeared at 2880 and 2955 cm^{-1} .^[122]

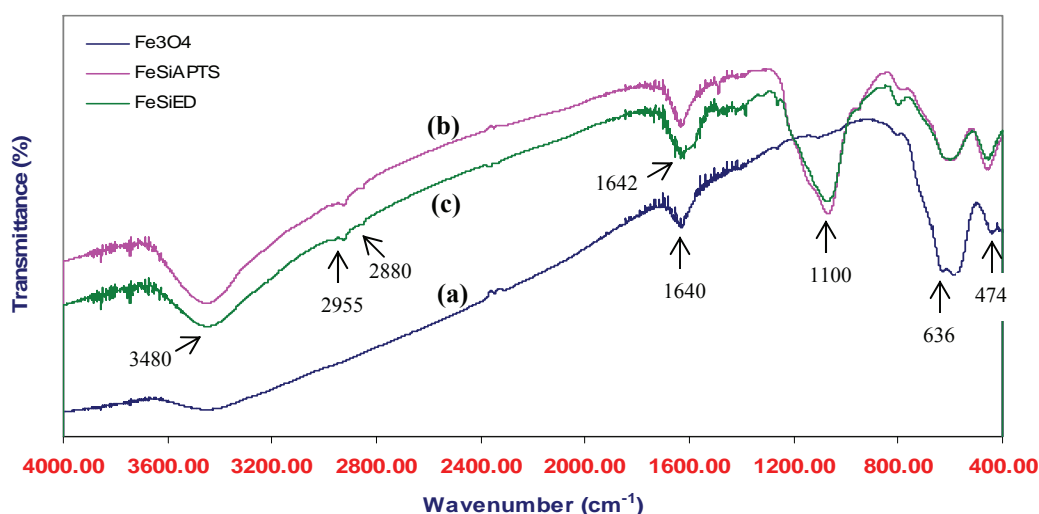


Figure 13. FTIR spectra of (a) unfunctionalized SPMNs, (b) monoamine (FeSiAPTS), and (c) diamine (FeSiED) functionalized silica-coated SPMNs

A summary of the corresponding FTIR absorption bands and assignment of SPMNs, FeSiAPTS, and FeSiED are given in *Table 4* and are assigned to various modes.^[42,119-122]

Table 4. FT-IR absorption frequencies for the bare and silica coated SPMNs ^[a]

unfunctionalized SPMNs	Functionalized SPMNs ^[b]	Assignment of absorption bands
3200 – 3600	3200 – 3600	ν (O-H) for H ₂ O (sample taking up H ₂ O) or ν (O-H) for H-bonded OH groups (from silanol groups)
–	3300 – 3500	ν (NH ₂) (stretching vibration)
–	~ 2880.2 and 2955.5	ν (C-H) (weak stretching vibrations of propyl groups)
1634.4 – 1655.6	1560 – 1660	ν (N-H) (bending mode) ν (C-O) for CO ₂ (from air) ν (O-H) (deformation vibration)
–	~ 1100	ν (Si-O) (stretching vibration)
474 and 636	~ 584	ν (Fe-O) (stretching vibrations of bulk Fe ₃ O ₄ in tetrahedral site) ν (Fe-O-Si) (stretching vibrations)
< 400	–	ν (Fe-O) (stretching vibrations of bulk Fe ₃ O ₄ in octahedral site)

^[a]Spectra are collected in the range 400 – 4000 cm⁻¹.

^[b]The functionalized column represents absorption bands of both monoamine (FeSiAPTS) and diamine (FeSiED) functionalized silica-coated SPMNs.

3.1.4.3 Surface area and porosity analysis

The surface of iron oxides such as SPMNs (Fe_3O_4) contains structural groups (sites) which could interact with gas and soluble species. The mechanisms for these interactions are not well understood, especially in the case of soluble species. However, using this concept, Brunauer, Emmet and Teller proposed a method that could be used to estimate the specific surface area (SSA) of solid materials.^[111,112]

The BET method was used to determine the surface areas of the uncoated SPMNs and, for comparison, of the unfunctionalized silica-coated SPMNs (FeSi). The specific surface area of a solid is defined as the surface area of a unit mass of material, usually expressed as $\text{m}^2 \text{g}^{-1}$. Applying the BET method, adsorption isotherms were obtained by measuring the amount of nitrogen gas that adsorbed at the boiling temperature of liquid N_2 (-77 K) on out-gassed SPMN and FeSi samples as a function of relative pressure, p/p_0 . Here p represents the partial pressure of the adsorbate and p_0 is the equilibrium vapour pressure.

The N_2 adsorption and desorption isotherms and corresponding BET plots are shown in *Figures 14* and *15* for SPMN and FeSi materials, respectively.

The following linear relationship exists between the amount of N_2 adsorbed, v ($\text{cm}^3 \text{g}^{-1}$) and the relative vapour pressure, p/p_0 .^[111,112]

$$\frac{p/p_0}{v(1-p/p_0)} = \frac{1}{v(p_0/p-1)} = \frac{1}{v_m c} + \frac{c-1}{v_m} \cdot \frac{p}{p_0} \quad (11)$$

where, v_m is the monolayer capacity of adsorption and c is the BET constant.

These values can be obtained from the linear BET plots (*Figures 14 b* and *15 b*), according *equation 11*. The BET constant and the value of v_m are related to the slope, s , and the intercept, i on the ordinate, as follows:

$$v_m = (s + i)^{-1} \text{ and } c = \frac{s}{i} + 1 \quad (12)$$

The surface area is then estimated from v_m and the area occupied by one molecule of adsorbate, which in the case of nitrogen is $0.162 \text{ nm}^2/\text{molecule}$.

As can be seen from the adsorption isotherms, the adsorption increases rapidly at low relative pressure, moderately at intermediate relative pressure, and then quite rapidly as the relative pressure approaches unity. Reversing the process by reducing the relative pressure leads to the formation of a hysteresis loop. This behaviour is typical of mesoporous and macroporous materials; *i.e.*, those that have pore sizes larger than 20 Å and 500 Å, respectively. Such pores are likely to have a wide range of sizes and shapes. The SPMNs surface area was estimated to be $160.28 \pm 0.77 \text{ m}^2/\text{g}$, with an average pore diameter of around 61.12 Å. The FeSi surface area was estimated to be $183.14 \pm 0.53 \text{ m}^2/\text{g}$, with an average pore diameter of approximately 97.16 Å. Therefore, it can be concluded that coating the SPMN surface with silica resulted in an increase in total surface area and pore diameter.

From the specific surface areas obtained from the BET – N₂ adsorption isotherms, it is possible to estimate relative particle sizes using the relation in *equation 13*.^[123]

$$\phi \text{ (nm)} = \frac{6000}{\mu S} \quad (13)$$

where, ϕ is the particle diameter, μ - density of the material and S - specific surface area.

Using *equation 13*, together with the values of SPMN density (1.006 g/cm^3) and the determined surface area, an estimate value of particle diameter for SPMN was calculated to be 6.21 nm. This value of SPMN size compares well with the values estimated from TEM and XRD analysis (*sections 3.1.1 and 3.1.2*). An accurate density measurement for the FeSi material could not be obtained, which meant the relative particle diameter of this material using *equation 13* could not be estimated.

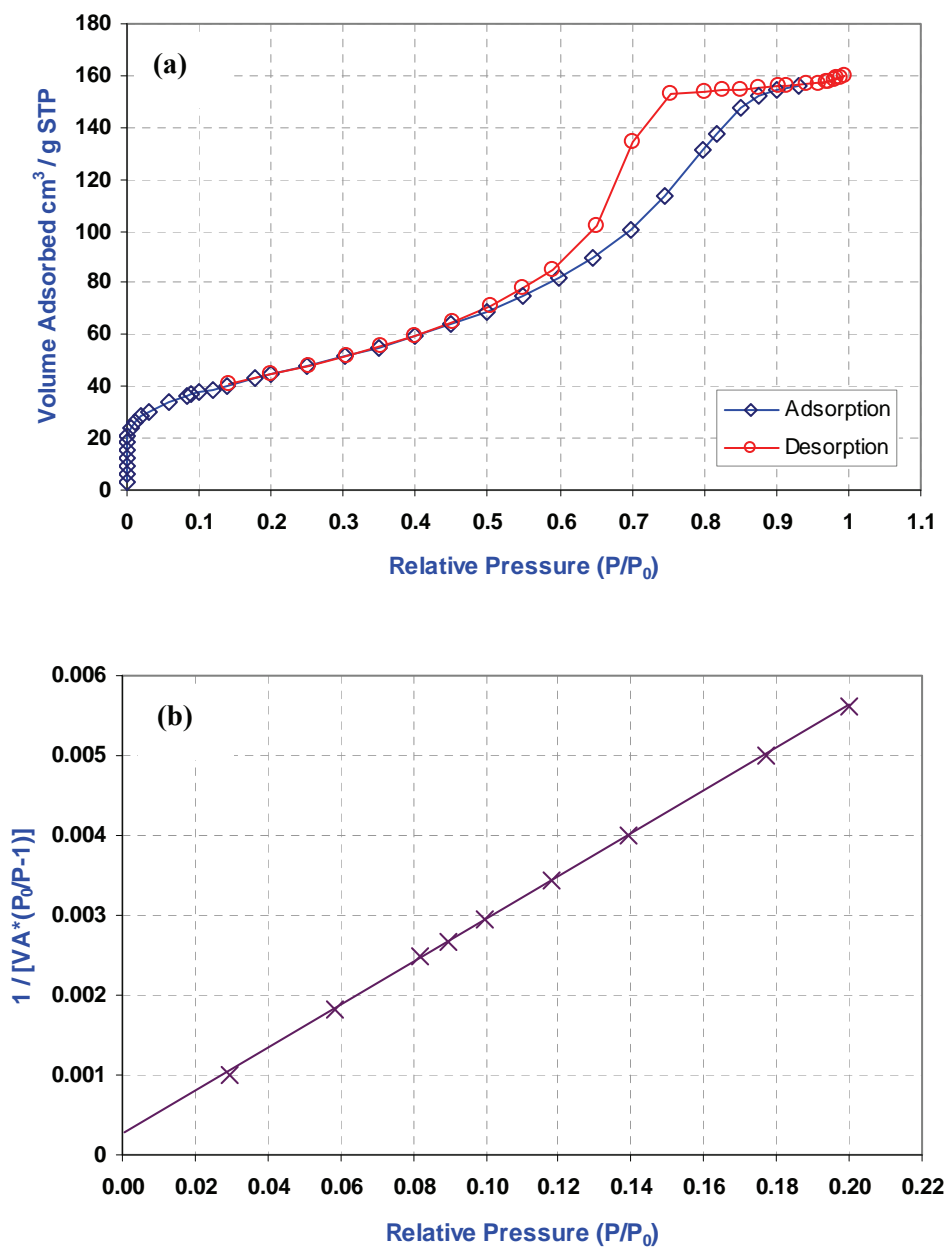


Figure 14. (a) N_2 adsorption-desorption isotherms of SPMN materials, and (b) corresponding BET plot. Surface area: $160 \pm 0.77 \text{ m}^2/\text{g}$; average pore diameter: 61.12 \AA

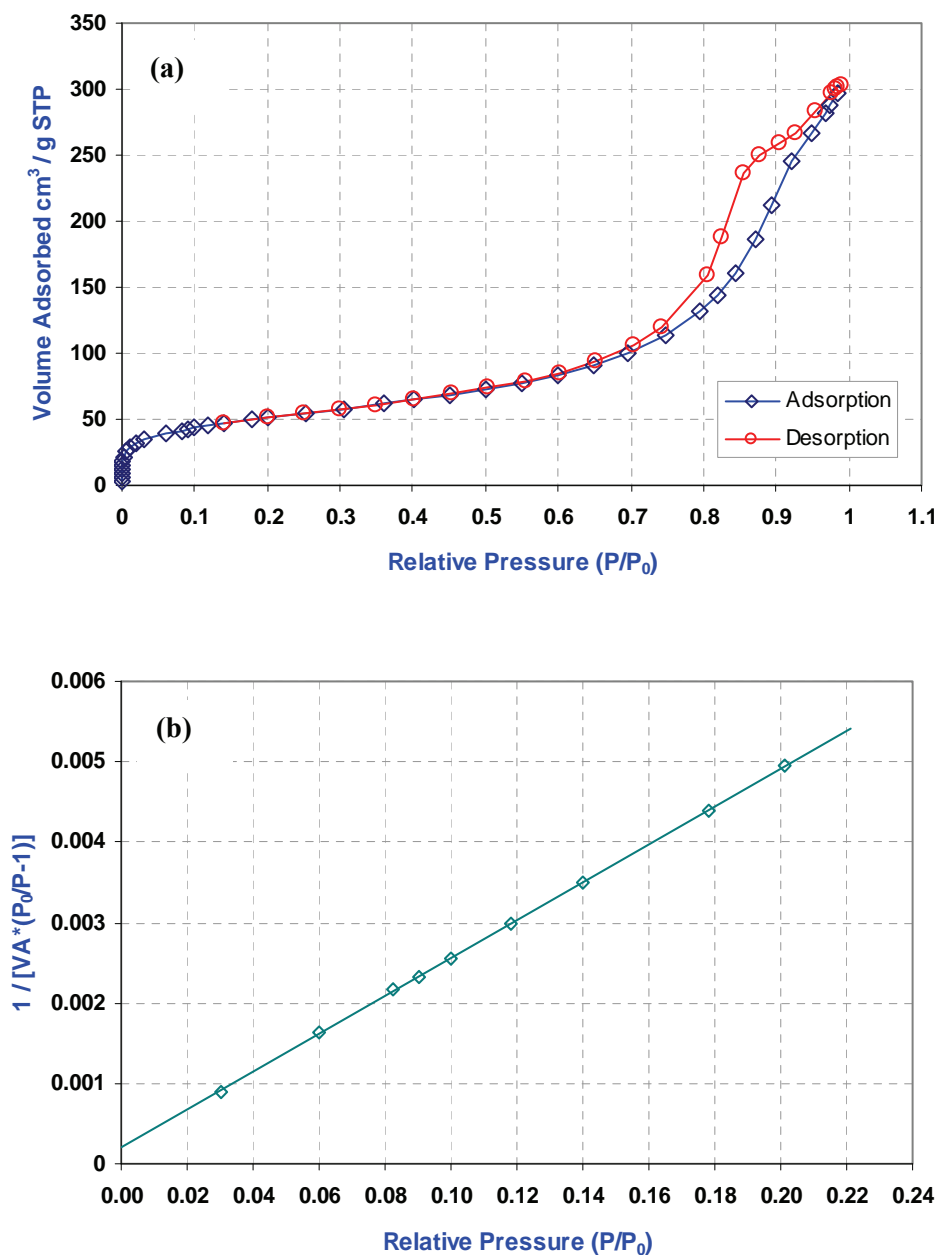


Figure 15. (a) N_2 adsorption-desorption isotherms of FeSi materials, and (b) corresponding BET plot. Surface area: $183 \pm 0.53 \text{ m}^2/\text{g}$; average pore diameter: 97.16 \AA

3.1.5 Magnetic characterization

The magnetic properties of the synthesized magnetite (Fe₃O₄) nanoparticles incorporated into a stable ferrofluid were analyzed by Vibrating Sample Magnetometry (VSM). This was done to determine the saturation magnetization of these materials and also to determine whether they are superparamagnetic.

The result of the magnetic measurements is shown in *Figure 16*. The magnetization curve indicates magnetization as a function of applied magnetic field as measured at room temperature (293 K). Typical characteristics of superparamagnetic behavior are observed showing zero coercivity and zero remanance above the blocking temperature.^[42,124] As previously indicated, the magnetization of the nanoparticles below the blocking temperature has a hysteretic feature (*Figure 5 in Chapter One*).

The diameter of the magnetic cores (D_M) could be calculated from data obtained during the magnetization measurements by assuming a lognormal distribution and using the following formula.^[125]

$$D_M = \left(\frac{18kT}{\pi M_s} \sqrt{\frac{\chi_i}{3M_s \cdot H_0}} \right)^{\frac{1}{3}} \quad (14)$$

which has a standard deviation σ_M around the magnetic core of

$$\sigma_M = \frac{1}{3} \left(\ln \frac{3\chi_i}{M_s \cdot 1/H_0} \right)^{\frac{1}{2}} \quad (15)$$

k is the Boltzmann constant, T is the absolute temperature, M_s is the saturation magnetization, χ_i is the initial magnetic susceptibility ($\chi_i = dM/dH_{H \rightarrow 0}$), and $1/H_0$ is the intercept on the $1/H$ for the high field extrapolation of the magnetization versus $1/H$.

Applying the above *equations 14 and 15*, the value of D_M was found to be 10.91 ± 0.49 nm. In addition, the saturation magnetization, M_s from the magnetization curve in *Figure 16* for the SPMNs was found to be 28×10^3 A/m at 293 K. These materials could be easily manipulated by applying an external magnetic field (using a ferrite bar magnet), which further confirmed superparamagnetic behavior of these Fe₃O₄ nanoparticles. This was illustrated in *Scheme 3*.

As discussed in *Chapter One, section 1.2.4*, zero coercivity and zero remanance (*i.e.* no hysteresis effect) on the magnetization curve shows that the material is superparamagnetic in nature. This was indicated by the dotted lines in *Figure 5*. The magnetization curve the of Fe_3O_4 nanoparticles obtained in this work, is shown in *Figure 16 (a)* and for comparison, a magnetization curve illustrating superparamagnetic behavior of Fe_3O_4 based nanoparticles from literature is shown in *Figure 16 b.*^[116]

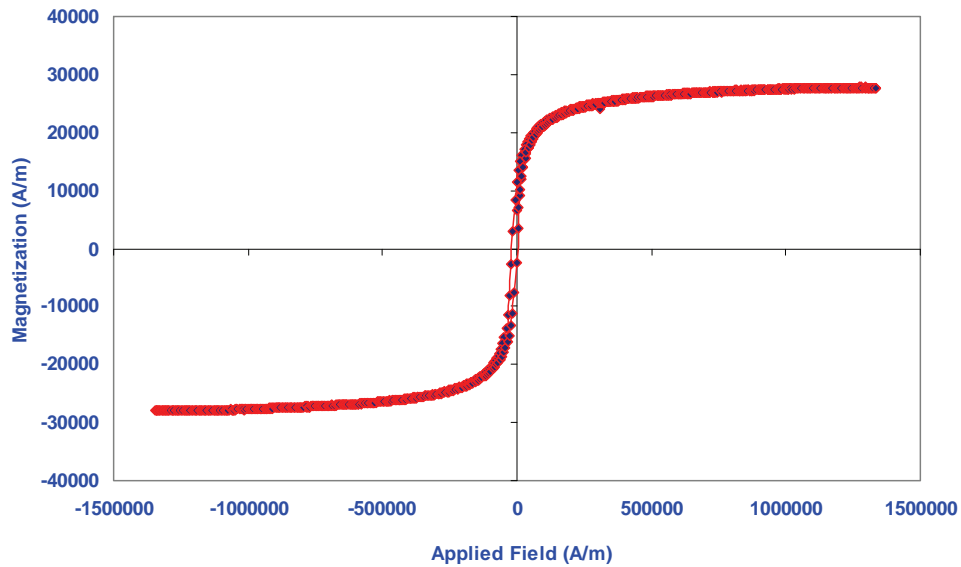


Figure 16 (a). Magnetization curve of Fe_3O_4 nanoparticles illustrating superparamagnetism.

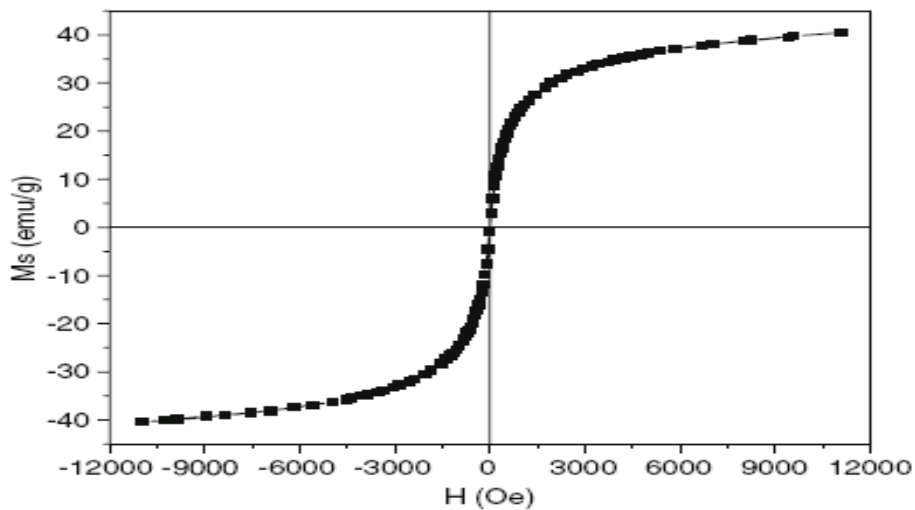


Figure 16 (b). Magnetization curve from literature of Fe_3O_4 nanoparticles illustrating superparamagnetism.^[116]

The magnetization curve (*Figure 16 a*) of Fe₃O₄ nanoparticles confirms their superparamagnetic behavior. The Fe₃O₄ nanoparticles that were synthesized *via* the co-precipitation method yielded nanoparticles having sizes in the range of 5 – 15 nm, a fact that supports the superparamagnetic nature of these materials. A summary of the fundamental values of the SPMNs, silica-coated SPMNs and amine-functionalized silica-coated is shown in *Table 5* below.

Table 5. Summary of characterization values obtained.

Adsorbent material	Loading capacity (mmol NH ₂ /g) ^[a]	BET surface area (m ² /g)	BET mean pore size (Å)	Particle diameter (nm)		
				XRD	TEM	VSM
SPMNs	-	160 (±0.8)	61.12	5.3 (± 0.7)	9.0 (±1.2) ^[c] 5.2 (±0.7) ^[d]	10.9 (±0.5)
FeSiAPTS	0.8 (±0.4)	183 (±0.5) ^[b]	97.16	-	80 – 120	-
FeSiED	0.9 (±0.3)	183 (±0.5) ^[b]	97.16	-	80 – 120	-

^[a] Values based on elemental (C, H, and N) analysis

^[b] Values based on silica coated SPMNs

^[c] Value obtained from SPMN synthesis under aerobic conditions

^[d] Value obtained from SPMN synthesis under anaerobic conditions

Chapter Four

Adsorption and potential removal of Au(III), Pd(II) and Pt(II) from acidic chloride-rich solutions using amine functionalized silica-coated SPMNs

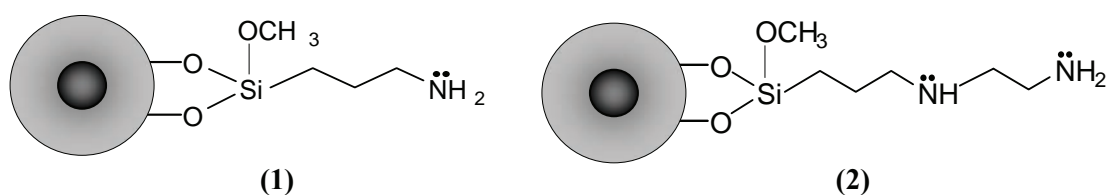
The removal of dissolved precious metals from aqueous solutions has long been an important issue. The industry is interested in recovering such metals from aqueous solutions. Dissolved precious metals such as gold, silver, palladium and platinum commonly end up in industrial waste water. As reviewed in *Chapter One*, there are conventional processes for removing precious metals from an aqueous solution. Such processes are expensive, require substantial quality control, and have their own recovery and disposal problems. Another conventional method for the recovery of precious metals from solutions is the use of electrodeposition processes, in which suspended or dissolved precious metals are deposited by electrolysis onto an electrode by electrolytic reduction. However, these processes become very inefficient and cease to be cost-effective when applied to aqueous solutions containing low concentrations of the precious metals. Even after the rigorous separation and refining processes as illustrated in *Chapter One*, there are trace amounts of precious metals left in the waste solutions of industrial process effluents. For this reason, a more economical and effective method for removal of $[\text{AuCl}_4]$, $[\text{PdCl}_4]^{2-}$ and $[\text{PtCl}_4]^{2-}$ from aqueous solutions is the subject of the current investigation.

In this chapter, the feasibility of using SPMNs and modified SPMNs as potential nano-adsorbent and anion exchanger materials for the removal of $[\text{AuCl}_4]$, $[\text{PdCl}_4]^{2-}$ and $[\text{PtCl}_4]^{2-}$ from dilute HCl solutions is demonstrated. The interest in using SPMNs for the removal of precious metals from aqueous solutions arises from the fact that these materials offer unique characteristics such as large surface area and high surface reactivity. This, along with the superparamagnetic behavior of the materials, makes them excellent candidates for combining metal adsorption ability with ease of magnetic phase separation. First, the results of the investigations will be presented and at the end of each section, mechanisms responsible for the removal of the precious metals under the studied experimental conditions will then be hypothesized.

4.1 Results and Discussions

4.1.1 Adsorption of complex anions using amine-functionalized silica-coated SPMNs

In this study, we focused on the adsorption of $[\text{PdCl}_4]^{2-}$, $[\text{PtCl}_4]^{2-}$ and $[\text{AuCl}_4]^-$ from dilute HCl solutions using two different amine-functionalized silica-coated SPMN nanocomposite materials, containing (1) monoamine and (2) diamine functionalities. A simplified two-dimensional representation of these magnetic potential anion-exchange materials also referred to as (1) FeSiAPTS and (2) FeSiED is shown below:



The small black sphere symbolizes the SPMN core, while the pale outer shell represents a layer of silica functionalized by amine methoxysilanes (for simplicity, only one amine ligand grafted onto silica surface is shown). It was found that the amine methoxysilane ligands are grafted on average onto the surface of the silica-coated SPMNs *via* two methoxy groups (*Chapter 3*).

In acidic solutions, the amine moieties of these ion-exchange materials are expected to be protonated. We investigated the possibility that the adsorption of the precious metal anionic complex was due to electrostatic interaction. In this regard, the effect of various experimental conditions and influences on the adsorption capacity was evaluated. All the experiments were carried out by batch sorption experiments at room temperature. Theoretically, in all the cases, the ligand : metal ion molar ratio should allow for complete adsorption of $[\text{PdCl}_4]^{2-}$, $[\text{PtCl}_4]^{2-}$ and $[\text{AuCl}_4]^-$ by materials (1) and (2).

4.1.1.1 Effect of contact time on $[\text{PdCl}_4]^{2-}$ and $[\text{PtCl}_4]^{2-}$ adsorption

The effect of contact time on the adsorption of $[\text{PdCl}_4]^{2-}$ and $[\text{PtCl}_4]^{2-}$ was investigated using only the monoamine functionalized material, (1) FeSiAPTS. These experiments were performed to determine the time required to attain equilibrium and to investigate whether (1) had an affinity for these metals under the studied experimental conditions. The time course profiles of sorption for $[\text{PdCl}_4]^{2-}$ and $[\text{PtCl}_4]^{2-}$ using (1) are shown in *Figure 17*. It should be noted that only 10 mg

samples were used in these batch sorption experiments as given by the experimental conditions in the figure caption. Each adsorption data point (*Figure 17*) was obtained by adding the particular quantity of material to a fixed aliquot of feed solution of known concentration and agitated for a certain amount of time as indicated in the figure. The solid phase was then separated from the aqueous phase and the effluents collected were analyzed for metal ion content *via* ICP-AES. Mass balancing was then used to determine amount of metal adsorbed.

The results indicate that, as the contact time increased from 3 to 15 minutes, steady state sorption for neither $[\text{PdCl}_4]^{2-}$ and $[\text{PtCl}_4]^{2-}$ species has been attained. After 30 minutes contact, the quantity of $[\text{PdCl}_4]^{2-}$ and $[\text{PtCl}_4]^{2-}$ adsorbed remained approximately constant. This indicates that equilibrium between these metal species and the available amine surface sites on **(1)** has been reached and that under the experimental conditions, **(1)** has a low affinity for these PGMs. As can be seen from *Figure 17*, a maximum adsorption of only 11.9 % for $[\text{PdCl}_4]^{2-}$ and 10.0 % for $[\text{PtCl}_4]^{2-}$ was obtained from the aqueous phase containing these metals in 0.5 M HCl solutions.

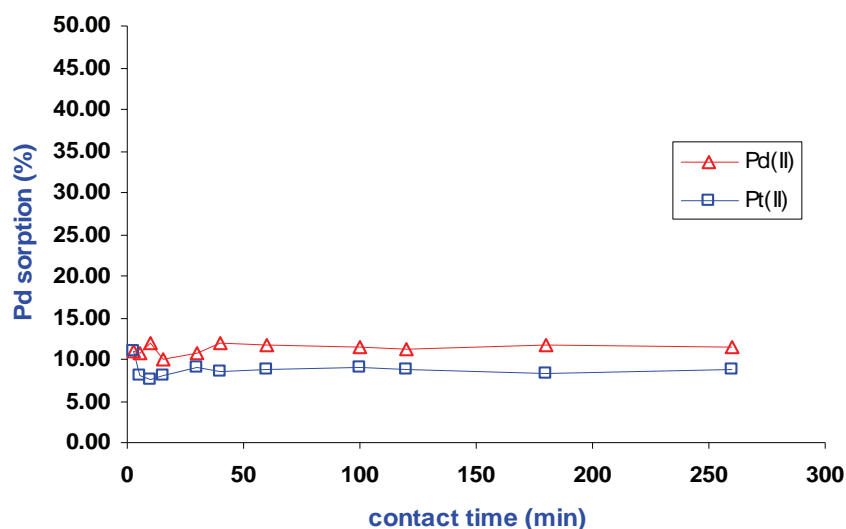


Figure 17. Effect of contact time on the adsorption of anionic Pd(II) and Pt(II) complexes from 0.5 M HCl onto FeSiAPTS. Experimental conditions: mass FeSiAPTS used: 10 mg; Pd(II) concentration used: 7.7 mg/L; Pt(II) concentration used: 10.0 mg/L. Total metal aqueous phase: 10 mL; pH: 0.26; Temperature: 21 ± 1 °C.

However, when the pH of the aqueous solution containing HCl is increased to 2.27 (HCl concentration 0.01M), significant improvement in adsorption efficiency of $[\text{PdCl}_4]^{2-}$ and $[\text{PtCl}_4]^{2-}$ using **(1)** is observed, as shown in *Figure 18*. Interestingly, the rate at which these precious metals were adsorbed is rapid with the adsorption equilibrium being reached in 35 minutes.

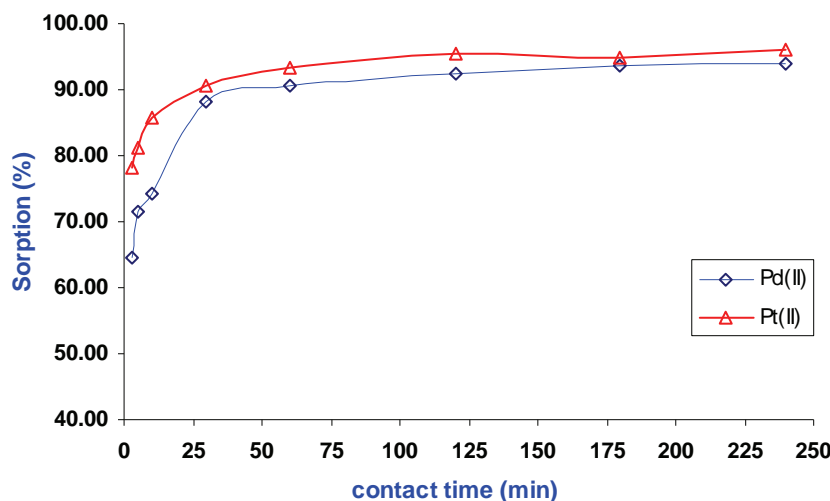


Figure 18. Effect of contact time on the adsorption of Pd(II) and Pt(II) onto FeSiAPTS. Single-metal solution experiments in 0.01 M HCl. Experimental conditions: mass FeSiAPTS used: 10 mg; Pd(II) concentration used: 7.8 mg/L; Pt(II) concentration used: 9.8 mg/L; Total metal aqueous phase: 10 mL; pH: 2.27; Temp: 21 ± 1 °C.

It is evident from the high initial slope and good adsorption efficiency that material **(1)** in fact has a high affinity for these precious metals. It was found that after only 3 minutes of contact, 78.2 % $[\text{PtCl}_4]^{2-}$ has been adsorbed whereas up to 64.6 % $[\text{PdCl}_4]^{2-}$ metal species has been adsorbed. Overall, at equilibrium a maximum adsorption of 95.9 % $[\text{PdCl}_4]^{2-}$ and 98.8 % $[\text{PtCl}_4]^{2-}$ was obtained. Thus, decreasing the molarity of the aqueous acidic solutions were accompanied by an improvement in the rate of $[\text{PdCl}_4]^{2-}$ and $[\text{PtCl}_4]^{2-}$ adsorption when compared to experiments conducted in 0.5 M HCl solutions (Figure 17). From these results, it could therefore be concluded that the solution pH and the concentration of free unbound Cl^- ions have an influence on the adsorption and removal of these metal species from the solutions using material **(1)**.

4.1.1.2 Effect of contact time on $[\text{AuCl}_4]^-$ adsorption

The effect of contact time on the adsorption of $[\text{AuCl}_4]^-$ was also investigated in order to determine the rate of sorption using different quantities of both materials **(1)** and **(2)**. The results obtained for the $[\text{AuCl}_4]^-$ single-metal solution experiments are presented in Figure 19. The experimental conditions that were used are given in the figure captions. It should be noted that in these particular experiments, a constant HCl solution concentration of 0.5 M was used ($\text{pH} < 1$).

The amount of gold adsorbed (as mass %) as a function of contact time is shown in Figures 19 (a) and (b) for different quantities (10, 30, and 50 mg) of **(1)** and **(2)**, respectively. It was

evident from the results that the rate of sorption is relatively slow, with equilibrium (or steady state) not being reached after 380 minutes of contact for either **(1)** or **(2)**, regardless of the quantity of material used. This suggests that under the studied experimental conditions, ion-exchange was likely not to be the mechanism responsible for the removal of $[\text{AuCl}_4]^-$ species from the aqueous solution, since ion-exchange is normally associated with fast sorption kinetics.^[29] It can be seen that the $[\text{AuCl}_4]^-$ adsorption characteristics for different masses of materials **(1)** and **(2)** differ, which would further suggest that under the studied experimental conditions, $[\text{AuCl}_4]^-$ was not adsorbed by ion-exchange. However, results that demonstrate otherwise, *i.e.* that ion-exchange is the mechanism for the removal of these precious metals from dilute HCl solution using **(1)** and **(2)**, will be discussed in *section 4.1.1.4* of this chapter.

The observed trend is that the rate of $[\text{AuCl}_4]^-$ adsorption is enhanced with increasing mass of both **(1)** and **(2)**. This indicates that the amount and rate of adsorption is dependant on the quantity of adsorbent used. As could have been predicted, the adsorption rates for **(2)**, containing diamine functionalities in the backbone, are found to be faster than those of **(1)** which contains monoamine functionalities. Material **(2)** therefore, has extra protonated sites in the backbone as compared to **(1)**, enabling this relatively faster rate of $[\text{AuCl}_4]^-$ adsorption.

The porosity of a solid material can influence the kinetics of adsorption. Diffusion in and out of pores is often considered responsible for slow adsorption processes when porous materials are used as adsorbents.^[125] Surface area analysis of the silica-coated SPMNs before amine functionalization, confirmed the presence of porosity (*Chapter Three*). Even after surface functionalization, it is still expected that **(1)** and **(2)** used in the adsorption studies to be porous, although to a lesser extent. In this case, the diffusion of $[\text{AuCl}_4]^-$ species into the materials **(1)** and **(2)** as a result of their porosity is possible, and subsequently has an effect on the adsorption rate. This could explain the slow sorption kinetics that can be seen in *Figure 19*. Also, after the adsorption process there was evidence of partial iron dissolution from the encapsulated SPMN cores. This further demonstrates the existence of porosity in these materials.

On closer investigation of *Figure 19*, it appears that $[\text{AuCl}_4]^-$ adsorption occurred in four stages. Between 0 – 60 minutes of contact solid – aqueous phase, the amount of $[\text{AuCl}_4]^-$ adsorbed was relatively low (less than 25 %), with $[\text{AuCl}_4]^-$ adsorption onto the 10 mg batch samples of either materials almost negligible. Between 60 – 80 minutes a large increase was observed, followed by a slower increase between 80 – 240 minutes. Finally, a significant difference was observed from 240 - 360 minutes of contact. These increases in $[\text{AuCl}_4]^-$ adsorption with contact time as well as

the dependence of the sorption kinetics on the quantity of (1) and (2), suggests that an additional mechanism (other than ion-exchange) is likely to be responsible for the adsorption of $[\text{AuCl}_4]^-$ onto the studied materials. It is evident though that $[\text{AuCl}_4]^-$ is not effectively absorbed by (1) and (2) under the studied experimental conditions.

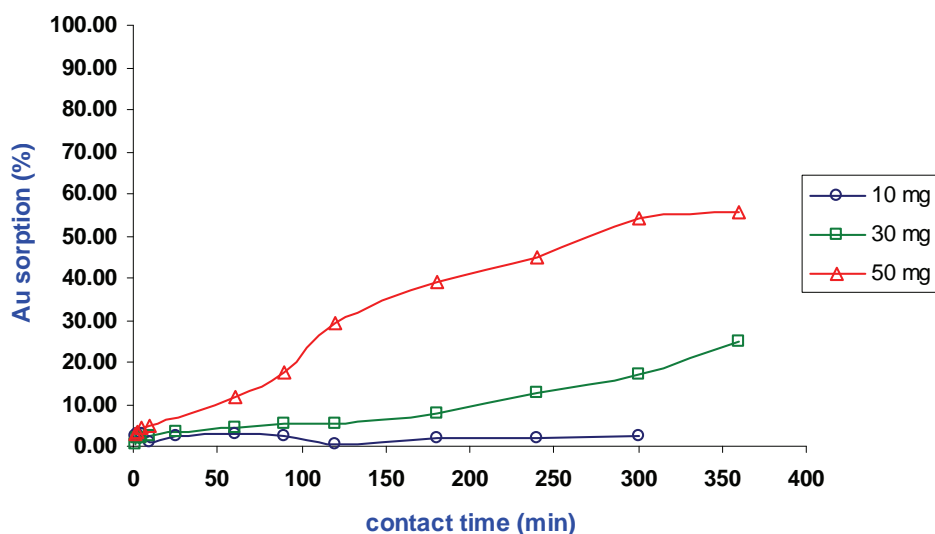


Figure 19 (a). Effect of contact time on the adsorption of Au(III) by (1) FeSiAPTS. Single-metal experiment done in 0.5 M HCl. Experimental conditions: masses material used: 10, 30, 50 mg; constant Au(III) concentration: 20 mg/L; Total metal aqueous phase: 10 mL; Temp: $21 \pm 1^\circ\text{C}$.

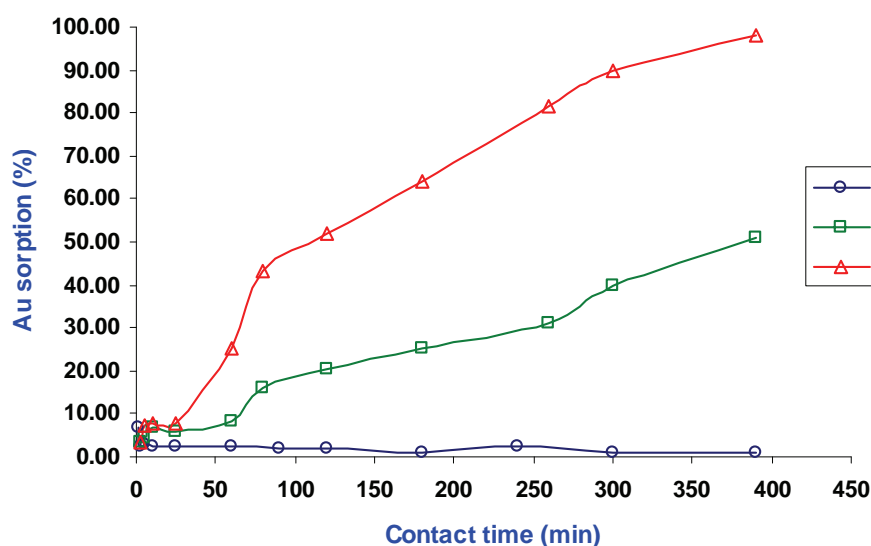


Figure 19 (b). Effect of contact time on the adsorption of Au(III) by (2) FeSiED. Single-metal experiment done in 0.5 M HCl. Experimental conditions: masses material used: 10, 30, 50 mg; constant Au(III) concentration: 20 mg/L; Total metal aqueous phase: 10 mL; Temp: $21 \pm 1^\circ\text{C}$.

As in the case of the PGM adsorption from solution (Figure 18) using material **(1)**, $[\text{AuCl}_4]^-$ adsorption efficiency improved with a decrease in the aqueous HCl concentrations from 0.5 M to 0.01M (Figure 20). The rate of adsorption was relatively fast. After only 3 minutes, almost 52 % of the $[\text{AuCl}_4]^-$ species in solution is adsorbed and in less than 30 minutes equilibrium adsorption is reached. At equilibrium, a maximum equilibrium adsorption of 76.8 % is observed. It is evident from the high initial slope and good adsorption efficiency that material **(1)** has a high affinity for $[\text{AuCl}_4]^-$ in 0.01 M HCl as compared to the adsorption from 0.5 M HCl.

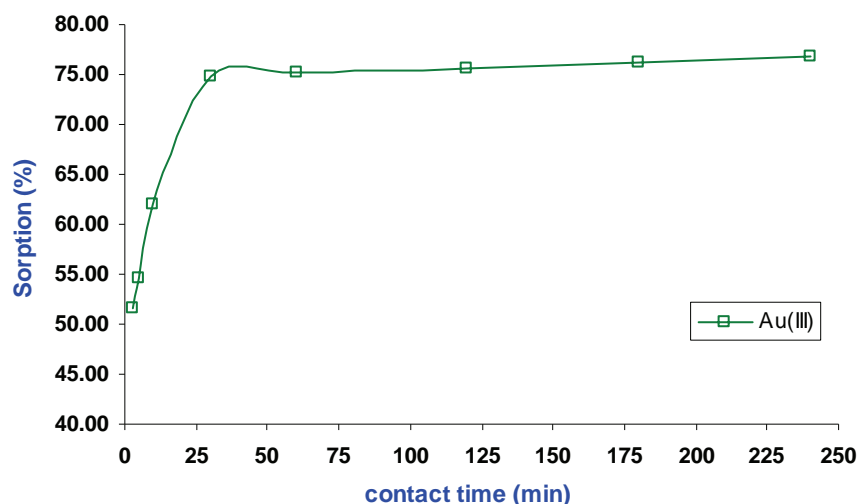


Figure 20. Effect of contact time on the adsorption of Au(III) onto FeSiAPTS. Single-metal solution experiments in 0.01 M HCl. Experimental conditions: mass FeSiAPTS used: 10 mg; Pd(II) concentration used: 7.8 mg/L; Pt(II) concentration used: 9.8 mg/L; Total metal aqueous phase: 10 mL; pH: 2.27; Temp: 21 ± 1 °C.

As already alluded to, in HCl media, platinum, palladium and gold readily form chloro-complexes, whose distribution strongly depends on solution pH and chloride concentration.^[126] It has been reported that in aqueous acidic solutions with chloride concentration above 5 mM, Pt(II), Pd(II) and Au(III) are present in solution only in the form of chloro-platinate, chloro-palladate, and chloro-auric complexes with anionic charges. In solutions with chloride concentrations between 0.7 – 5 mM, these complexes normally have neutral charges and in solutions with lower chloride concentrations (below 0.7 mM) they have cationic charges.^[127]

It is believed that the amine groups of **(1)** and **(2)** are protonated in HCl solutions, so that most of the metal adsorption can be explained by electrostatic attraction and ion-exchange of anionic metal complexes with these protonated amine groups. Although amine groups may contribute to metal chelation, in acidic solutions their protonation significantly reduces their ability to coordinate to the metal species.^[12,128]

In conclusion, the relatively low adsorption found for $[\text{AuCl}_4]^-$, $[\text{PdCl}_4]^{2-}$ and $[\text{PtCl}_4]^{2-}$ from 0.5 M HCl aqueous acidic solutions could be attributed to an excess of free chloride ions in solution resulting in competition for available protonated sites on **(1)** and **(2)**. The strong competition effect of chloride on sorption performance results in an electrostatic interaction *via* an ion-exchange mechanism being involved in the adsorption of these metal chloro-complexes onto the protonated amine functional groups. At higher pH (0.01 M HCl), the amount of chloride in the solution should be high enough to favour the formation of chloro-anionic species that will be attracted by the protonated amine groups in the backbone of **(1)** and **(2)**, but at the same time low enough not to interfere with the adsorption, therefore not hampering the adsorption rate and loading capacity. Thus, using the nano-sized materials **(1)** and **(2)**, a solution pH of approximately 2 was found to be optimum for specifically $[\text{PdCl}_4]^{2-}$ and $[\text{PtCl}_4]^{2-}$ metal species adsorption. Also, an increase in $[\text{AuCl}_4]^-$ adsorption was obtained with increased solution pH. It is believed that the porosity of **(1)** and **(2)** had an influence on the efficiency of precious metal removal. However, this is still the subject of much work.

4.1.1.3 Effect of initial $[\text{AuCl}_4]$ ion concentration

The effect of initial metal ion concentration on the sorption of $[\text{AuCl}_4]^-$ was studied in order to estimate the maximum loading capacity of materials **(1)** and **(2)**. From adsorption data describing the concentration change of $[\text{AuCl}_4]^-$ species in solution, the amount of $[\text{AuCl}_4]^-$ adsorbed by **(1)** and **(2)** could be determined per unit mass of adsorbing material. The experimental adsorption data of $[\text{AuCl}_4]^-$ on **(1)** and **(2)** were analyzed in terms of the *Langmuir*^[129] and *Freundlich*^[130] *isotherm models* and the results obtained were compared. These two models are the most frequently used equilibrium adsorption isotherm models in the literature.

The *Langmuir model* is based on monolayer adsorption on the active sites of the adsorbent. Furthermore, the *Langmuir model* assumes that there is no interaction between adsorbate species and that once a species occupies a site, no further sorption can take place at that site.

Theoretically therefore, a saturation value is reached, beyond which no further sorption can take place. The *Langmuir adsorption model* ^[129,131] is given by the following equation:

$$q_e = \frac{q_{\max} k_L C_e}{1 + k_L C_e} \quad (16)$$

which can be linearized and rearranged into

$$\frac{C_e}{q_e} = \frac{1}{q_{\max} k_L} + \frac{C_e}{q_{\max}} \quad (17)$$

where q_e is the equilibrium loading capacity (mmol/g), C_e is the equilibrium metal concentration in the aqueous phase (mmol/L), q_{\max} the maximum loading capacity (mmol/g), and k_L is the *Langmuir constant* (L/mmol). This constant can be calculated from the intercept and slope of the linear plot, with C_e/q_e versus C_e .

The *Freundlich model* ^[130] explains the adsorption on a heterogeneous (multiple layer) surface with uniform energy. The model can be represented as follows:

$$q_e = k_F C_e^{1/n} \quad (18)$$

which can be rearranged into

$$\ln q_e = \ln k_F + \frac{1}{n} \ln C_e \quad (19)$$

where q_e is the equilibrium loading capacity (mmol/g), C_e is the equilibrium metal concentration in the aqueous phase (mmol/L), k_F is the *Freundlich constant* (L/mmol), and n is the heterogeneity factor associated with the *Freundlich model*. These constants can be calculated from the slope and intercept of the linear plot, with $\ln q_e$ versus $\ln C_e$.

The experimental conditions in both sorption batch experiments were kept constant, *i.e.*, same amount used for (1) and (2), the contact time was 24 h for each, and $[\text{AuCl}_4]^-$ stock solutions containing known amounts of the metal were diluted with the same stock of HCl solution with concentrations of 0.5 M. The loading capacity as determined from elemental analysis

(Chapter Three) was found to be 0.75 mmol/g and 0.87 mmol/g for material **(1)** and **(2)**, respectively. The experimental loading capacity and the loading capacity predicted by both the Langmuir and Freundlich models are shown in *Figure 21*. The corresponding Langmuir and Freundlich parameters along with corresponding coefficients of correlation are listed in *Table 6*. The results presented in *Table 6* show that the maximum loading capacity obtained for $[\text{AuCl}_4]^-$ on **(2)** is higher than that of **(1)**. The difference in loading capacities can be attributed to the relative ligand concentrations. Elemental analysis indicated that the ligand concentration of **(2)** is higher than that of **(1)**, which means that **(2)** has relatively more binding sites available for interaction with $[\text{AuCl}_4]^-$ species in solution, which enhances the loading capacity. According to the coefficients of correlation obtained and the fits shown in *Figure 21*, the Freundlich isotherm is not adequate for modeling the adsorption of $[\text{AuCl}_4]^-$ onto materials **(1)** and **(2)**. In contrast, the Langmuir model represents a good fit of the experimental data, and therefore is adequate for modeling the sorption isotherm. This suggested that the adsorption process was dominated by a monolayer adsorption process rather than a multiple one. The values of k_L are related to the energy of adsorption of the $[\text{AuCl}_4]^-$ on the solid surfaces. From the results obtained, it can be deduced that $[\text{AuCl}_4]^-$ was more strongly adsorbed on **(1)** under the experimental conditions studied. This, however, needs to be confirmed with further experimental studies. From the Langmuir model (*equation 16*), the maximum $[\text{AuCl}_4]^-$ loading capacity was determined to be 0.072 mmol/g (14.182 mg/g) and 0.111 mmol/g (21.863 mg/g) for **(1)** and **(2)**, respectively.

The essential features of the *Langmuir isotherm* can be expressed in terms of the dimensionless equilibrium parameter R_L , which is defined as $R_L = 1 / (1 + k_L C_0)$, where k_L is the Langmuir constant and C_0 is the initial concentration of $[\text{AuCl}_4]^-$ in solution. According to Hall *et al.*^[132], R_L values within the range $0 < R_L < 1$, indicate favorable adsorption. The present adsorption system showed R_L values between 0 and 1 as can be seen in *Table 7*. This meant that the adsorption of $[\text{AuCl}_4]^-$ on **(1)** and **(2)** was favorable.

The sorption of $[\text{AuCl}_4]^-$ by materials containing nitrogen bearing ligands can take place according to the mechanism of ion-exchange when the nitrogen atoms in the backbone of the material is protonated as shown in the *Scheme 10 and 11*. The representation of **(1)** and **(2)** in this illustration is of course an oversimplification of the materials. It is expected that the surface of the silica based backbone of these materials to be completely functionalized with these amine ligands to form ion-exchangers.

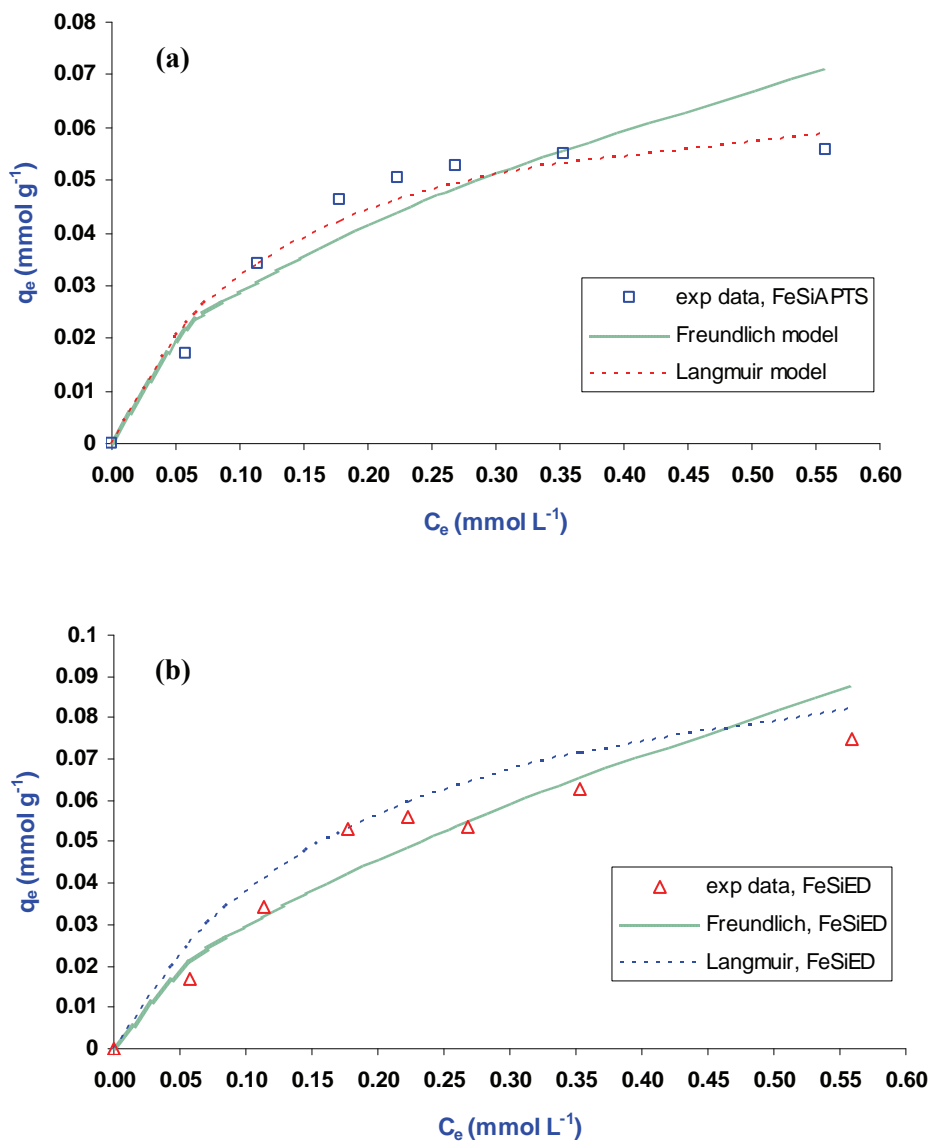


Figure 21. The relationship between the equilibrium loading capacity and the equilibrium gold concentration for (a) FeSiAPTS and (b) FeSiED. Experimental conditions: mass material used: 50 mg; contact time: 24 h, total metal aqueous phase: 15 mL, hydrochloric acid concentration: 0.5 M; temperature: $21 \pm 1^\circ\text{C}$.

Table 6. Langmuir and Freundlich isotherm parameters for materials (1) and (2)

	(1) FeSiAPTS	(2) FeSiED
<i>Langmuir</i>		
q_{\max} (mmol/g)	0.072	0.111
k_L (L/mmol)	7.93	5.16
R^2	0.9572	0.9410
<i>Freundlich</i>		
k_F (L/mmol)	0.097	0.127
n	1.90	1.57
R^2	0.8395	0.9059

Table 7. R_L values of $[AuCl_4]^-$ based on the Langmuir equation for materials (1) and (2)

C_0 (mg/L)	(1) FeSiAPTS	(2) FeSiED
11.33	0.0110	0.0168
22.51	0.0056	0.0085
34.98	0.0036	0.0055
43.97	0.0029	0.0044
52.90	0.0024	0.0037
69.41	0.0018	0.0028
109.98	0.0011	0.0018

4.1.1.4 Effect of chloride ion concentration

The effect of chloride ion concentration and the acidity of the metal aqueous solutions in the adsorption processes on both (1) and (2) were evaluated. The study was conducted using a constant $[AuCl_4]^-$ concentration (in 0.5 M HCl) of 26 mg/L. The additional chloride ions in solution were varied by addition of constant volumes of sodium chloride (NaCl) solutions of known concentrations to the fixed aqueous solutions already containing 0.5 M chloride ions. Therefore, the total chloride ion content in each individual sorption experiment (represented by

one data point) was 0.5 M plus the additional amounts added. It should be noted that only this additional amounts of chloride ions added is given on the x-axis in *Figure 22*. Recall from our previous study (*Figure 19*), adsorption equilibrium was not reached after 360 minutes. Therefore, a longer contact time of 24 h was utilized in these experiments, in order to ensure that equilibrium was approached.

The logarithm of the distribution coefficients and sorption capacity of $[\text{AuCl}_4]^-$ as a function of free chloride ions in solution is shown in *Figure 22*. As can be seen, *Figure 22* demonstrates that the chloride ions interfered with the $[\text{AuCl}_4]^-$ adsorption as shown by the decrease in sorption capacity and distribution coefficients K_d with increasing molar solutions of chloride ions. This decrease of $[\text{AuCl}_4]^-$ sorption with increasing concentration of counter ions (Cl^-) can be explained by the competition between the $[\text{AuCl}_4]^-$ chloro-complexes and the chloride anions, which may interact with the protonated amine groups of the adsorbent materials. This confirmed that the electrostatic attraction *via* ion-exchange was a likely mechanism responsible for the adsorption of $[\text{AuCl}_4]^-$ on protonated amine groups. Furthermore, as expected and as can be seen, the loading capacity of (2) FeSiED, was generally higher than that of resin (1) FeSiAPTS, due to the relatively higher degree of amine functionality and thus higher ligand concentration in the backbone of resin (2) (*refer to chapter 3*).

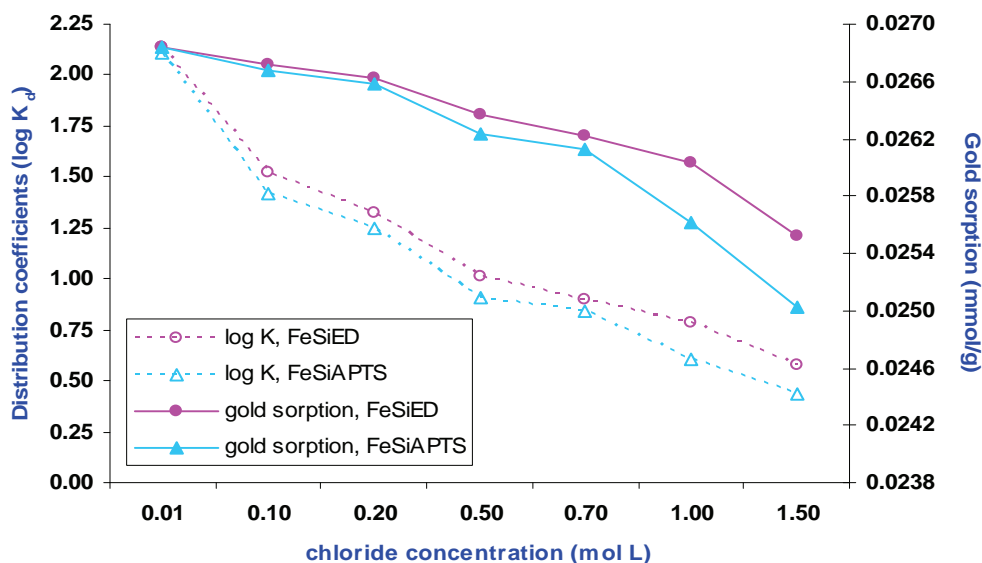
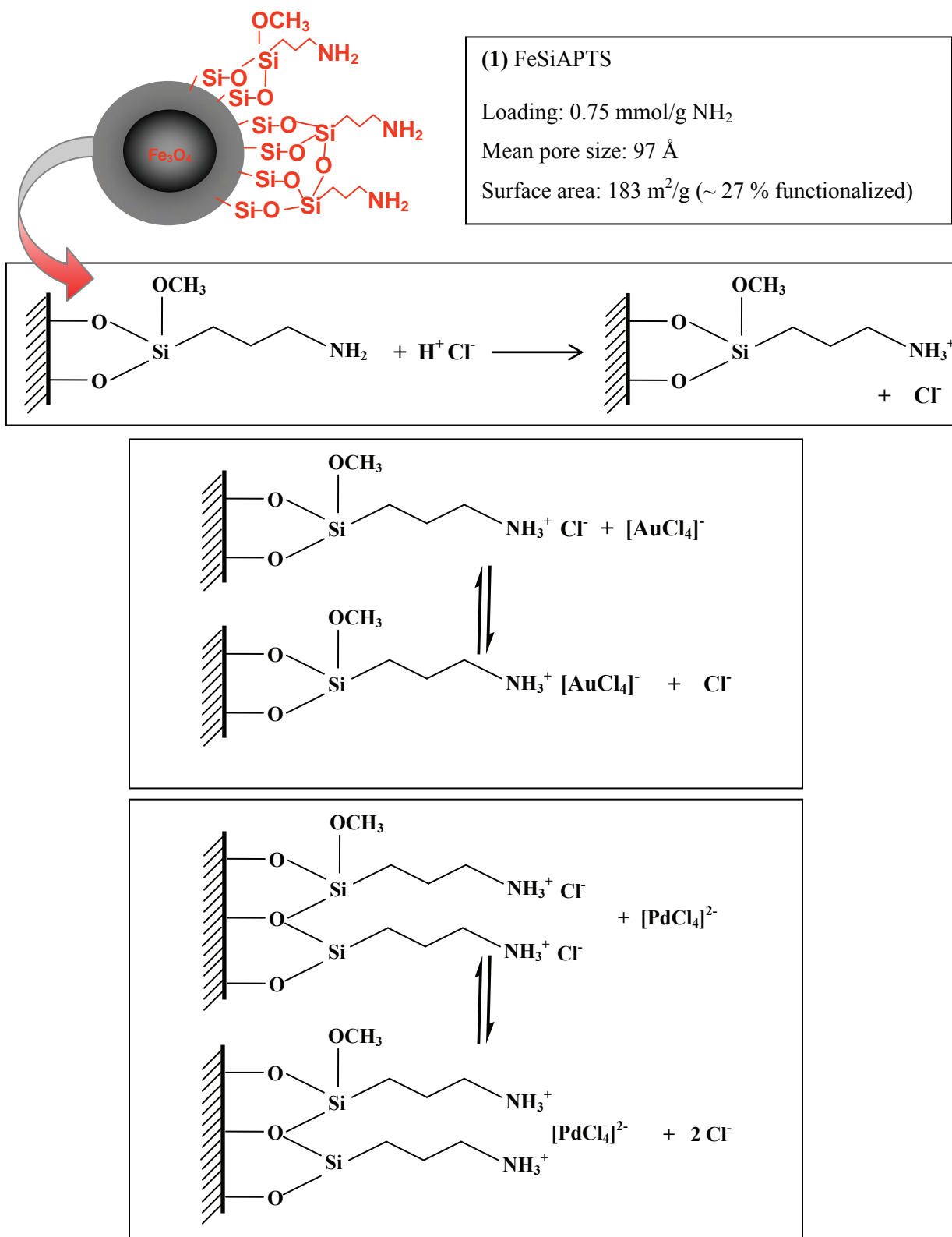
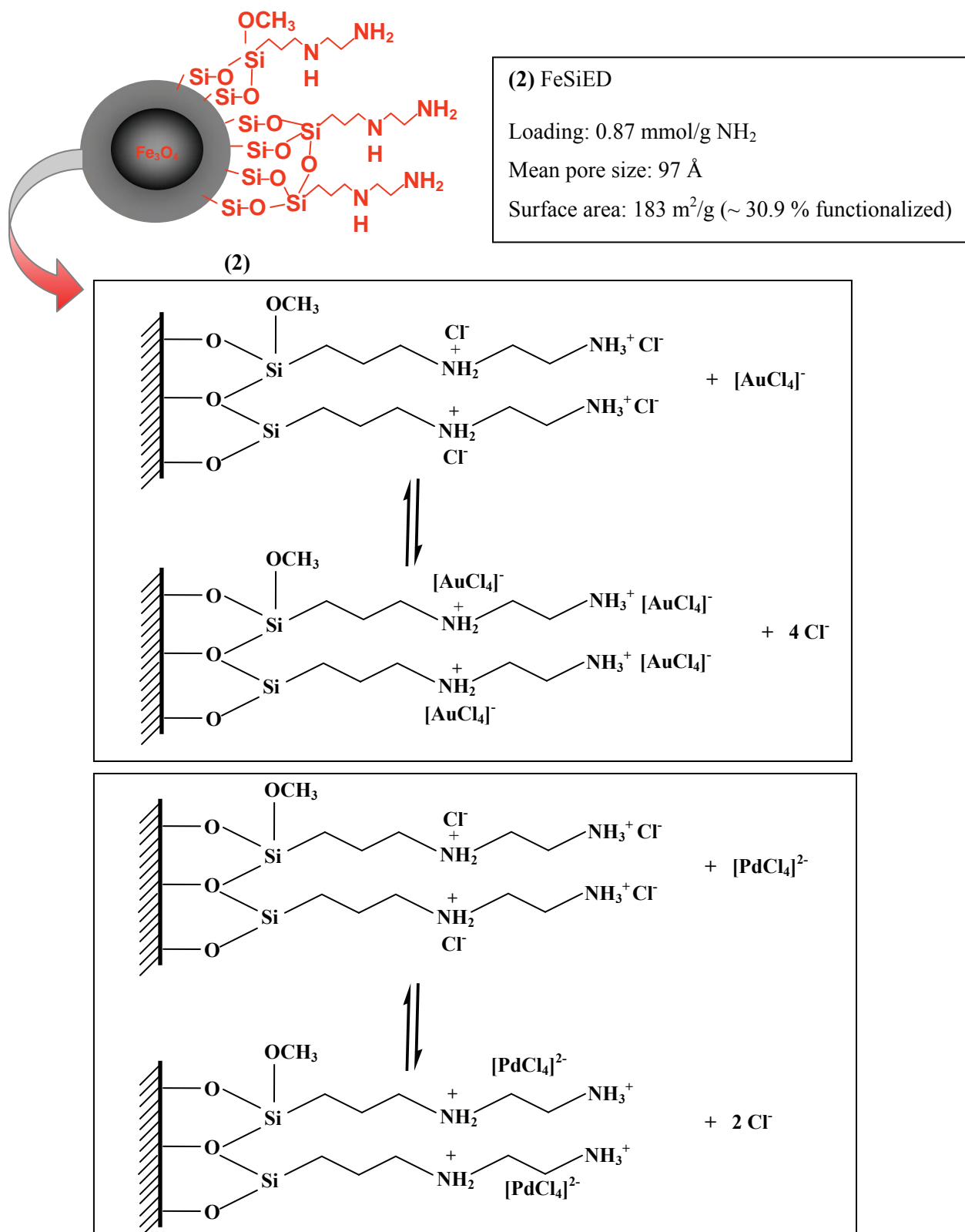


Figure 22. The effect of chloride ion concentration on the adsorption of Au(III) from aqueous acidic solutions onto (1) FeSiAPTS and (2) FeSiED. Experimental conditions: mass FeSiAPTS and FeSiED used: 50 mg; Au(III) concentration used: 26 mg/L in 0.5 M HCl. Total metal aqueous phase: 10 mL; additional chloride ion aqueous phase: 10 mL; Temperature: 21 ± 1 °C.



Scheme 10. Mechanism of [AuCl₄]⁻ and [PdCl₄]²⁻ removal from acidic solutions by FeSiAPTS.

Scheme 11. Mechanism of $[\text{AuCl}_4]^-$ and $[\text{PdCl}_4]^{2-}$ removal from acidic solutions by FeSiED.

4.1.2 Preliminary study to investigate $[AuCl_4]$, $[PdCl_4]^{2-}$ and $[PtCl_4]^{2-}$ recovery from solution

In a preliminary study as shown by the results in *Figure 23*, it was found that after 24 h contact, $[PdCl_4]^{2-}$ and $[PtCl_4]^{2-}$ was efficiently removed from aqueous acidic solutions by amine functionalized silica-coated SPMNs, FeSiAPTS and FeSiDETA. The good adsorption efficiency are attributed to an ion-exchange mechanism as shown in *Scheme 10 and 11*, since these materials is essentially protonated in solution and would readily facilitate these processes. As can be seen, the adsorption efficiency of $[PdCl_4]^{2-}$ and $[PtCl_4]^{2-}$ by unfunctionalized SPMNs (Fe_3O_4) and silica-coated SPMNs (FeSi) is lower. The mechanism responsible for these adsorption processes most likely entails electrostatic interactions between protonated surface hydroxyl groups and the anionic complexes. Surprisingly, it is found that $[AuCl_4]^-$ was consistently removed not only by the amine-functionalized silica-coated SPMNs but also the unfunctionalized SPMNs. The $[AuCl_4]^-$ species was quantitatively adsorbed. From these results it is apparent that surface silica coating and amine functionalization is not necessary to efficiently remove $[AuCl_4]^-$ from dilute HCl solutions. For this reason, we became interested in studying the $[AuCl_4]^-$ removal from aqueous acidic solutions by using in particular unfunctionalized SPMNs. The results of these studies are reported in *Chapter 5*.

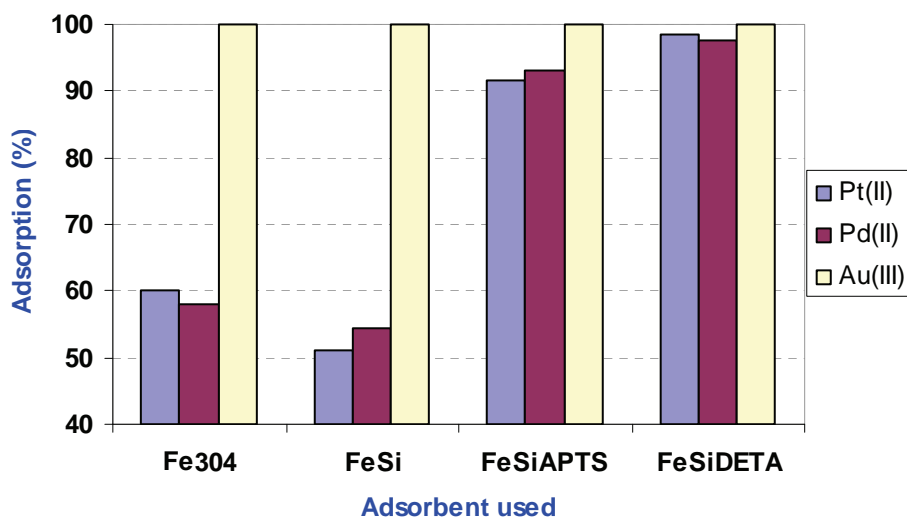


Figure 23. Adsorption of Au(III), Pd(II) and Pt(II) from 0.1 M HCl by various adsorbent materials. Experimental conditions: mass FeSiAPTS used: 50 mg; Au(III) concentration: 19.1 mg/L; Pd(II) concentration used: 10.8 mg/L; Pt(II) concentration used: 12.2 mg/L; Total metal aqueous phase: 15 mL; Temp: 21 ± 1 °C.

Chapter Five

Adsorption and potential removal of Au(III), Pd(II) and Pt(II) from acidic chloride-rich solutions using unfunctionalized SPMNs

5.1 Results and Discussions

In this study, we focused on the removal and adsorption of $[\text{AuCl}_4]^-$, $[\text{PdCl}_4]^{2-}$ and $[\text{PtCl}_4]^{2-}$ complexes from dilute HCl solutions using only the unfunctionalized SPMNs. These experiments were done in order to compare the adsorption capability and efficiency of the unfunctionalized SPMNs to that of the amine-functionalized silica coated SPMN nanocomposite materials **(1)** and **(2)**, respectively.

5.1.1 Adsorption of $[\text{AuCl}_4]^-$ using unfunctionalized SPMNs

5.1.1.1 Effect of contact time on $[\text{AuCl}_4]^-$ adsorption

The effect of contact time on the adsorption of $[\text{AuCl}_4]^-$ by the SPMNs was studied in order to determine the rate at which these precious metal species are removed from aqueous acidic solutions. The initial feed solutions contained known $[\text{AuCl}_4]^-$ concentrations and adsorption studies were carried out in 0.5 M and 0.01 M HCl media, respectively. Under these conditions, four series of batch experiments were carried out using different masses of SPMNs. One batch refers to one set of experiments using SPMNs of the same mass. In this regard, masses of 10, 30, 50 and 100 mg SPMNs were accurately weighed and contacted with the feed solutions. It is important to point out that all the experiments were carried out with the same batch of SPMNs to exclude variations in SPMN properties. The average particle size of the SPMNs used in these experiments were 10 ± 1.2 nm as estimated by transmission electron microscopy (TEM) and X-ray powder diffraction (XRD).

The results obtained for the adsorption of $[\text{AuCl}_4]^-$ species from 0.5 M HCl solutions by different masses of SPMNs (10, 30, 50, and 100 mg) are shown in *Figure 24 (a – d)*. It is evident that under the experimental conditions, the unfunctionalized SPMNs had a high affinity for the $[\text{AuCl}_4]^-$ species. In contrast to the slow rate of $[\text{AuCl}_4]^-$ adsorption by **(1)** and **(2)** (*Figure 19*), the SPMNs exhibit relatively high sorption rates depending on the SPMNs mass used.

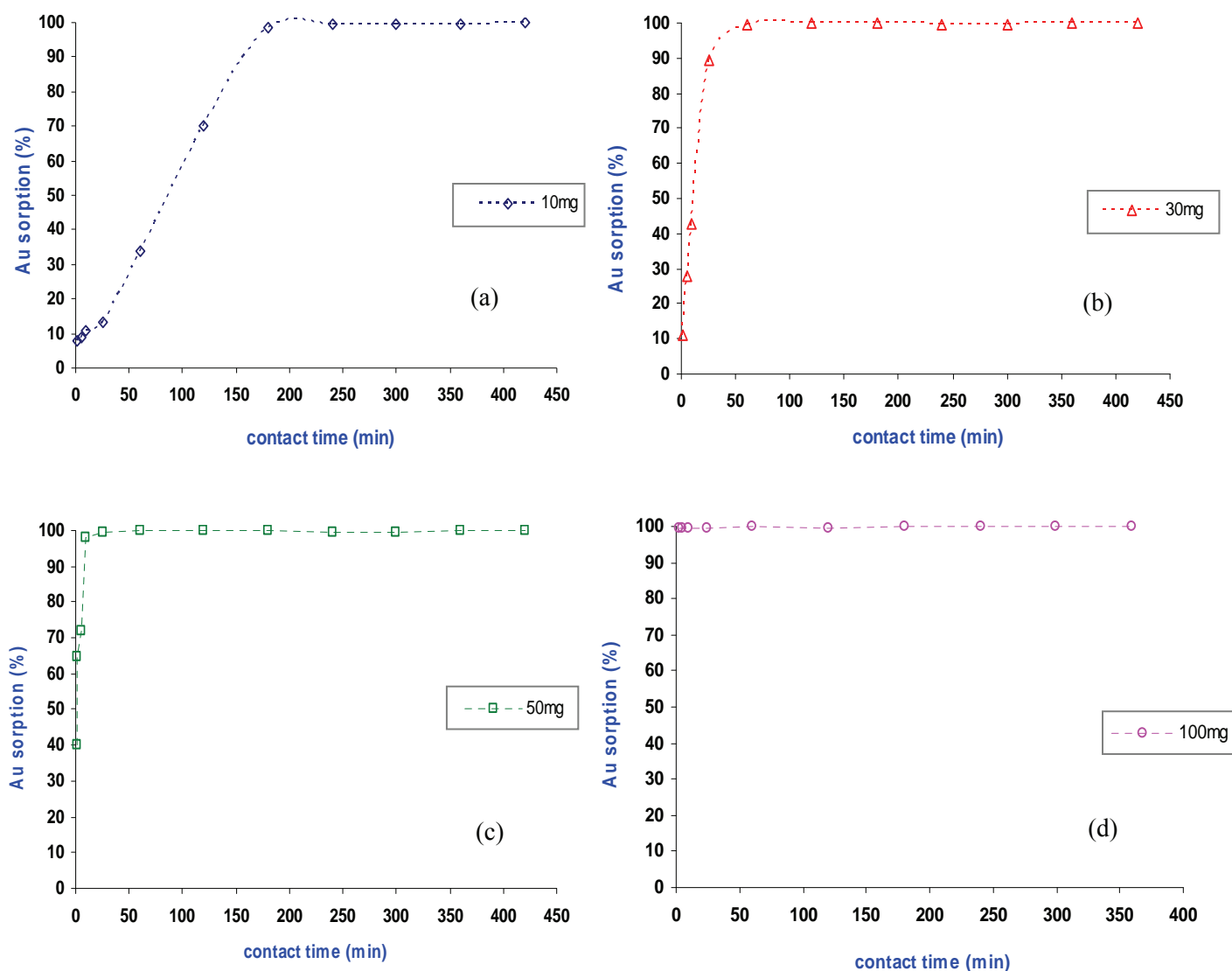


Figure 24. Effect of contact time on the adsorption of Au(III) onto SPMNs. Single-metal solution experiments in 0.5 M HCl. Experimental conditions: mass SPMNs used: (a) 10 mg, (b) 30 mg, (c) 50 mg, (d) 100 mg; Au(III) concentration used: 20.5 mg/L; Total metal aqueous phase: 10 mL; Temperature: $21 \pm 1^\circ\text{C}$. Each experimental data point represents one sorption experiment.

As could be seen from Figure 24 (a – d), with increasing the mass of the SPMNs in the individual batch experiments from 10 to 100 mg samples, the rate of adsorption increased, with 50 % of the total “available” $[\text{AuCl}_4^-]$ in solution ($t_{1/2}$) being reached in less than 90 minutes for the 10 mg batch experiment (Figure 24 a), less than 10 minutes for the 30 mg batch experiment (Figure 24 b) and less than 5 minutes for the 50 mg batch experiments (Figure 24 c). In the case of the 100 mg batch experiment the rate of $[\text{AuCl}_4^-]$ sorption was extremely rapid (Figure 24 d).

Interestingly, quantitative adsorption was attained for all four series of batch sorption experiments. From *Figure 24 (a)*, it could be seen that for the 10 mg batch experiments the total “available” $[\text{AuCl}_4]^-$ in solution is quantitatively removed in 180 minutes at a rate of approximately $1 \mu\text{g}/\text{min}$. Furthermore, from *Figure 24 (b – d)*, the total “available” $[\text{AuCl}_4]^-$ in solution is quantitatively removed in 60, 25, and 2 minutes at rates of approximately 3, 8, and $102 \mu\text{g}/\text{min}$, respectively. These results obtained from *Figure 24 (a – d)* are summarized in *Table 8* and the calculations are shown in *section A2* of the *supplementary section*.

Table 8. Data obtained for the adsorption of $[\text{AuCl}_4]^-$ from 0.5 M HCl by SPMNs

Mass SPMNs (mg)	Ratio of gold to SPMNs ($\mu\text{g gold}/\text{mg SPMN}$)	Approximate rate of gold removal ($\mu\text{g}/\text{min}$)
10	20.50	1.14
30	6.83	3.42
50	4.10	8.20
100	2.05	102.50

This phenomenon of rapid $[\text{AuCl}_4]^-$ depletion and subsequent quantitative $[\text{AuCl}_4]^-$ adsorption using the SPMNs as adsorbent materials can be briefly explained as follows. It is speculated that with increasing mass SPMNs, more surface sites are potentially available for interaction and adsorption, the result being that the sorption rate and the extent of $[\text{AuCl}_4]^-$ adsorption increases. Moreover, the high rate of adsorption can be attributed to the large surface area and high surface reactivity offered by the nano-size of the unfunctionalized SPMNs. Plausible mechanisms responsible for the adsorption under the experimental conditions studied are discussed in *section 5.2* of this chapter.

The rate at which $[\text{AuCl}_4]^-$ is adsorbed by SPMNs from 0.01 M HCl solutions was also investigated. In this regard, a series of $[\text{AuCl}_4]^-$ batch sorption experiments were carried out for different masses (10, 30, 50, 100 mg) following the same experimental methodology as used in the 0.5 M HCl experiments. The results obtained for the adsorption of $[\text{AuCl}_4]^-$ from 0.01 M HCl as a function of contact time are shown in *Figure 25*.

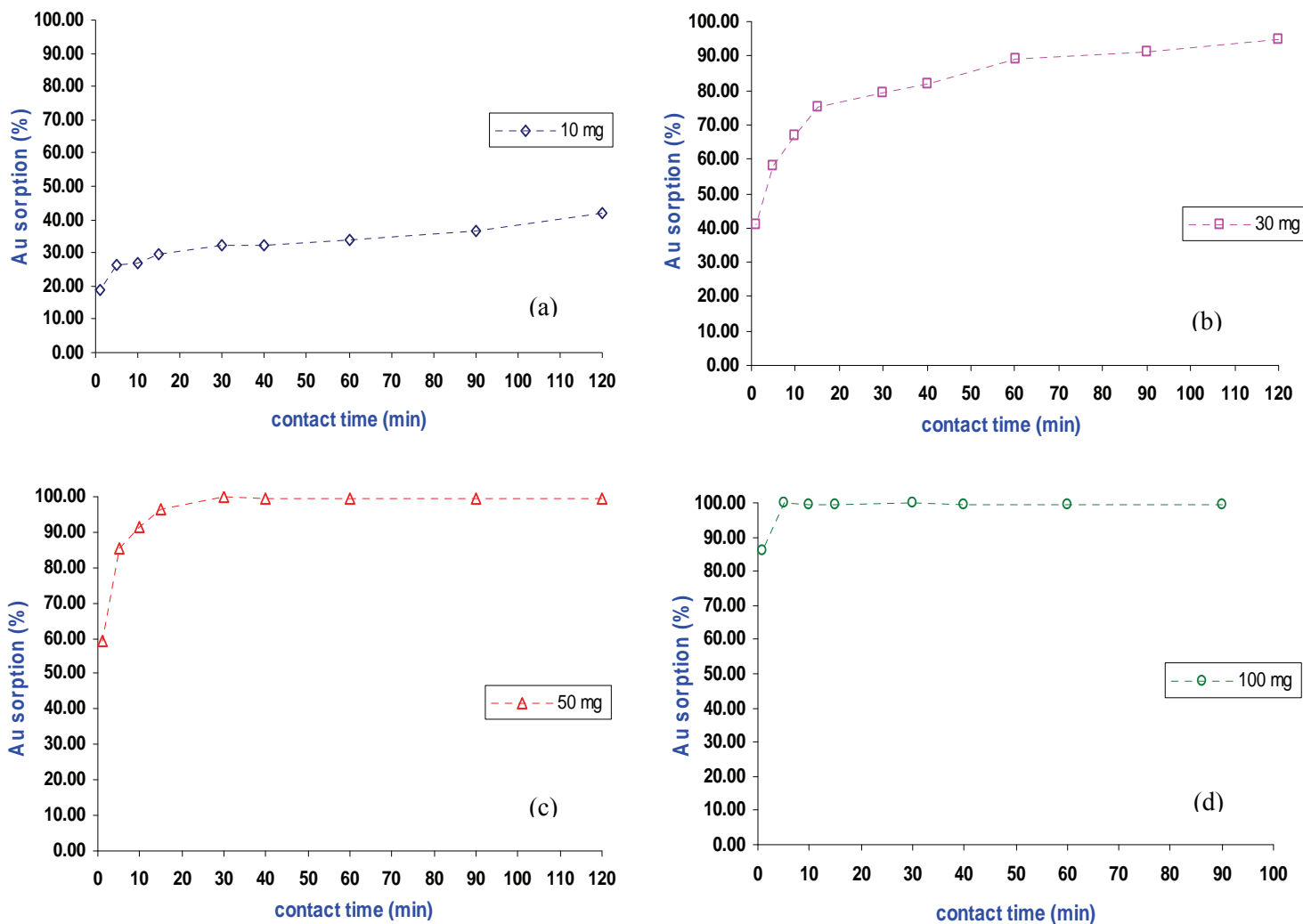


Figure 25. Effect of contact time on the adsorption of Au(III) onto SPMNs. Single-metal solution experiments in 0.01 M HCl. Experimental conditions: mass SPMNs used: (a) 10 mg, (b) 30 mg, (c) 50 mg, (d) 100 mg; Au(III) concentration used: 20.1 mg/L; Total metal aqueous phase: 10 mL; Temperature: $21 \pm 1^\circ\text{C}$. Each experimental data point represents one sorption experiment.

As can be seen from *Figure 25 (a)*, 42 % of the total amount of “available” $[\text{AuCl}_4]^-$ has been removed from the 0.01 M HCl solutions in 120 minutes at a rate of 0.7 $\mu\text{g}/\text{min}$. From *Figure 25 (b)*, there is a drastic improvement in the total amount of “available” $[\text{AuCl}_4]^-$ that has been removed, corresponding to 94 % in 120 minutes at a rate of approximately 1.5 $\mu\text{g}/\text{min}$. From *Figure 25 (c) and (d)*, the total amount of “available” $[\text{AuCl}_4]^-$ has been quantitatively removed in 30 minutes and 5 minutes at rates of approximately 6.7 $\mu\text{g}/\text{min}$ and 40.2 $\mu\text{g}/\text{min}$, respectively. These results obtained from *Figure 25 (a – d)* are summarized in *Table 9* and the corresponding calculations are shown in *section A2* of the *supplementary section*.

Table 9. Data obtained for the adsorption of $[\text{AuCl}_4]^-$ from 0.01 M HCl by SPMNs

Mass SPMNs (mg)	Ratio of gold to SPMNs ($\mu\text{g gold}/\text{mg SPMN}$)	Approximate rate of gold removal ($\mu\text{g}/\text{min}$)
10	20.10	0.70
30	6.70	1.57
50	4.02	6.7
100	2.01	40.2

As can be seen from *Figure 25*, there is a noticeable difference in the adsorption profiles as compared to *Figure 24*, indicating relatively slower sorption rates. Performing the sorption kinetics experiments in a less concentrated HCl media has an effect on the rate at which the $[\text{AuCl}_4]^-$ species are removed from solution and subsequently adsorbed onto the surface of the SPMNs. The effect of the concentration of the aqueous acidic media is therefore believed to have a direct influence on the mechanism governing the adsorption processes. In addition, an increased trend in the efficiency and rate of $[\text{AuCl}_4]^-$ adsorption with increasing SPMNs mass is observed. The mechanisms that govern the removal of the $[\text{AuCl}_4]^-$ species from solution and the subsequent adsorption onto the SPMN materials will be discussed later in this chapter.

5.1.1.2 Effect of initial $[\text{AuCl}_4^-]$ concentration on adsorption by unfunctionalized SPMNs

The effect of various $[\text{AuCl}_4^-]$ concentrations in solution on the adsorption of SPMNs was investigated in order to estimate the maximum loading capacity of the SPMNs. The results of the relationship between the equilibrium $[\text{AuCl}_4^-]$ concentration in the aqueous phase, C_e , and the equilibrium loading capacity, q_e , is shown in *Figure 26*. As seen from the results, the equilibrium load of $[\text{AuCl}_4^-]$ (mmol) per unit mass (g) of material increased almost linearly upon increasing the initial concentration of $[\text{AuCl}_4^-]$ species in solution up to *ca* 0.26 mmol/L and then no significant change was observed as equilibrium was approached. The maximum experimental equilibrium loading capacity was found to be 0.051 mmol $[\text{AuCl}_4^-]$ loaded per gram of SPMN material. As was done previously, the experimental data were fitted to non-competitive *Langmuir* and *Freundlich* models. However, only the experimental data fitted to the Langmuir model is presented here. The data fitted to the *Freundlich* model is omitted. It was found that there was not a good applicability between the data and the latter model. The fitting of the experimental data to the Langmuir model is given in *Figure 26*. As was expected by applying the model, a plot of C_e/q_e against C_e resulted in a straight line from which the Langmuir parameters could be obtained. Using the model, a theoretical value of the maximum equilibrium loading capacity, q_e , was calculated to be 0.071 mmol/g (13.984 mg/g). The experimental data was in reasonable good agreement with the *Langmuir* adsorption model, which indicates monolayer coverage on the SPMN surface.

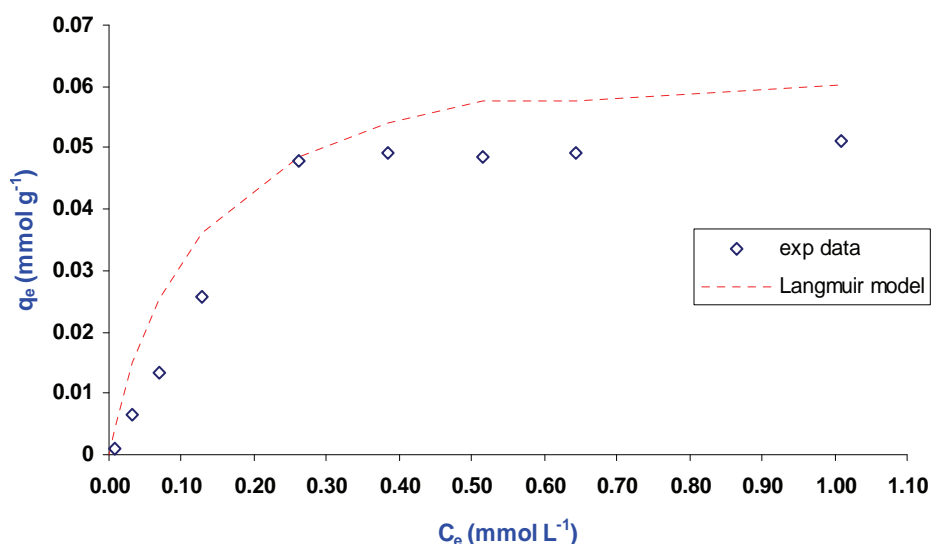


Figure 26. The relationship between the equilibrium loading capacity and the equilibrium gold concentration for SPMNs. Experimental conditions: mass material used: 50 mg; contact time: 60 minutes, total metal aqueous phase: 10 mL, hydrochloric acid concentration: 0.5 M; temperature: $21 \pm 1^\circ\text{C}$.

5.1.2 Adsorption of $[PdCl_4]^{2-}$ and $[PtCl_4]^{2-}$ using unfunctionalized SPMNs

5.1.2.1 Effect of contact time on $[PdCl_4]^{2-}$ and $[PtCl_4]^{2-}$ adsorption

The effect of contact time on the adsorption of $[PdCl_4]^{2-}$ and $[PtCl_4]^{2-}$ species from 0.5 M HCl and 0.01 M HCl using the SPMNs as adsorbent materials was also investigated. Once again, the experimental conditions were similar to those used in the $[AuCl_4]^-$ batch sorption studies. The results obtained from the batch experiments conducted in 0.5 M HCl are presented in *Figure 27*. It was evident that under the experimental conditions, SPMNs show low affinity towards these PGMs. Results indicates that the adsorption was almost negligible, with the sorption percentage not exceeding 6 % for $[PtCl_4]^{2-}$ and 3 % for $[PdCl_4]^{2-}$ species. Increasing the mass of the SPMNs in the batch experiments up to the 100 mg sample had no significant effect on the sorption efficiency. Therefore, only the 50 mg batch experiment results are shown. Similar trends were observed when conducting the same experiments in 0.1 M HCl solutions as shown in *Figure 28*. However, there was an increase in the adsorption efficiency. The results (*Figure 28*) show that sorption percentage did not exceed 13 % for the $[PtCl_4]^{2-}$ and 10 % for the $[PdCl_4]^{2-}$ species.

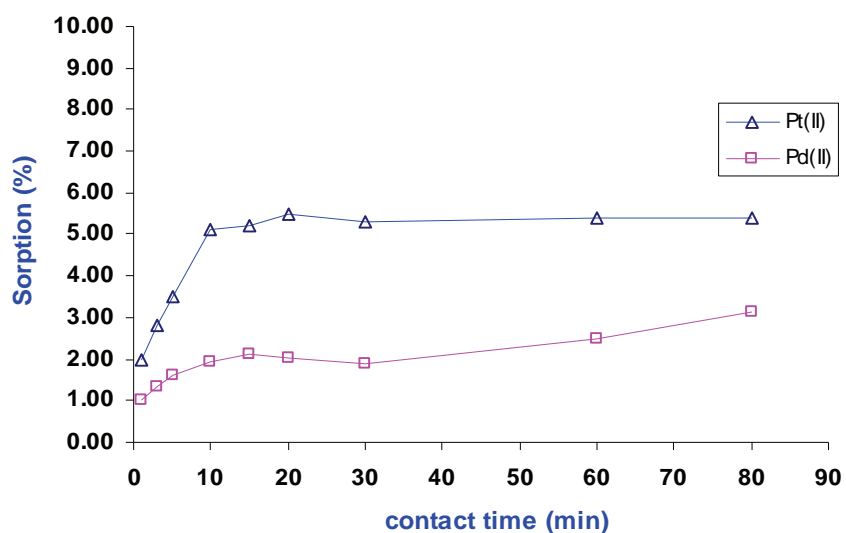


Figure 27. Effect of contact time on the adsorption of Pt(II) and Pd(II) onto SPMNs. Single-metal solution experiments in 0.5 M HCl. Experimental conditions: mass SPMNs used: 50 mg; Pt(II) concentration: 10 mg/L; Pd(II) concentration used: 7.7 mg/L; Total metal aqueous phase: 10 mL; Temperature: $21 \pm 1^\circ\text{C}$. Each experimental data point represents one sorption experiment.

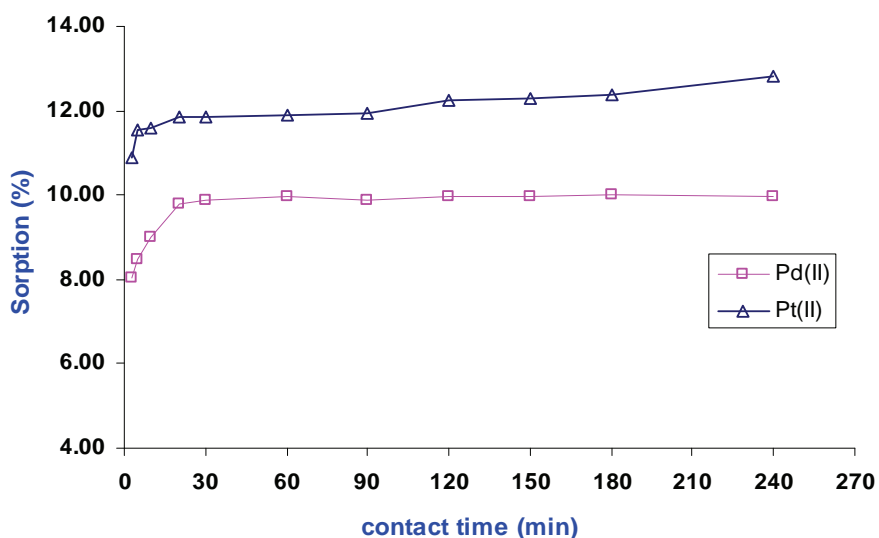


Figure 28. Effect of contact time on the adsorption of Pt(II) and Pd(II) onto SPMNs. Single-metal solution experiments in 0.1 M HCl. Experimental conditions: mass SPMNs used: 50 mg; Pt(II) concentration: 9.70 mg/L; Pd(II) concentration used: 8.90 mg/L; Total metal aqueous phase: 10 mL; Temperature: $21 \pm 1^\circ\text{C}$. Each experimental data point represents one sorption experiment.

Next, the influence of different solution pH on the adsorption processes and the removal of $[\text{PdCl}_4]^{2-}$ and $[\text{PtCl}_4]^{2-}$ species from solution was investigated. The fact that SPMNs are unstable in solutions of high acidic content^[42] was taken into account. Therefore, if the pH of the solutions containing the precious metals is too low, degradation due to iron dissolution might occur (Section 4.3.2). It was suspected that this would have a direct bearing on the adsorption processes, since the surface properties of the SPMNs will be altered. However, if the pH of the aqueous solution was too high, then hydrolysis of the precious metals could also occur. $[\text{PdCl}_4]^{2-}$ and $[\text{PtCl}_4]^{2-}$ are sensitive to hydrolysis and this will influence the distribution of the species in solution, and more specifically the formation of chloro-anionic complexes. In this regard, these experiments were done to determine the optimum pH range in which $[\text{PdCl}_4]^{2-}$ and $[\text{PtCl}_4]^{2-}$ could be most efficiently removed from solution and subsequently adsorbed by the unfunctionalized SPMNs. The aqueous solutions of different HCl concentrations (varying pH) that were used for these batch sorption experiments are as follows: 0.5 M HCl, 0.1 M HCl, 0.01 M HCl and 0.001 M HCl, respectively. In these pH ranges, $[\text{PdCl}_4]^{2-}$ and $[\text{PtCl}_4]^{2-}$ speciation is largely confined to the chloro-anionic complexes and metal cations.^[126,127] The results obtained for the $[\text{PdCl}_4]^{2-}$ and $[\text{PtCl}_4]^{2-}$ adsorption from the different acid media are shown in Figure 29. The results obtained from the various acid media indicate that the adsorption of $[\text{PdCl}_4]^{2-}$ and $[\text{PtCl}_4]^{2-}$ by the SPMNs is strongly affected by solution pH. As can be seen from Figure 29, there is definite improvement

in $[\text{PdCl}_4]^{2-}$ and $[\text{PtCl}_4]^{2-}$ adsorption efficiency with increasing solution pH. Thus, it is evident that the acidic content of the solutions has an influence on the adsorption of $[\text{PdCl}_4]^{2-}$ and $[\text{PtCl}_4]^{2-}$ by the SPMNs. Moreover, from Figure 29 (a) and (b) it can be seen that the sorption efficiency is also dependant on the masses of SPMNs. With an increase in the masses of SPMNs from 10 mg to 100 mg samples, the extent of $[\text{PdCl}_4]^{2-}$ and $[\text{PtCl}_4]^{2-}$ adsorption was drastically enhanced. From these results, it can be concluded that 0.001 M HCl solutions (pH 3) and SPMN mass exceeding 50 mg would suffice for quantitative $[\text{PdCl}_4]^{2-}$ and $[\text{PtCl}_4]^{2-}$ removal and adsorption.

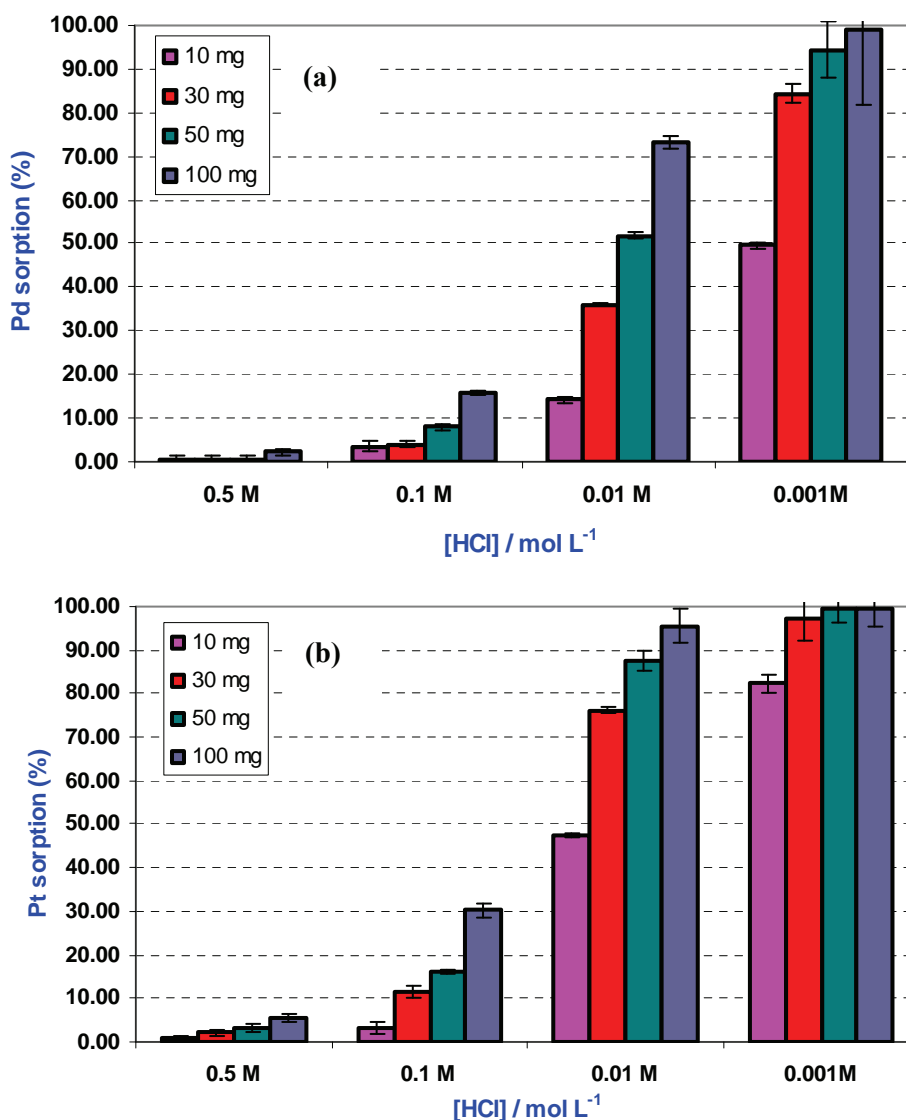


Figure 29. Effect of hydrochloric acid solution concentration (different solution pH) on the adsorption of (a) Pd(II) and (b) Pt(II) onto different quantities of SPMNs. Single-metal solution experiments. Experimental conditions: mass SPMNs used: 10, 30, 50, 100 mg; Pt(II) concentration range: 11.9 – 14.8 mg/L; Pd(II) concentration range: 7.0 – 10.6 mg/L; Total metal aqueous phase: 10 mL; contact time: 45 min. Temperature: $21 \pm 1^\circ\text{C}$.

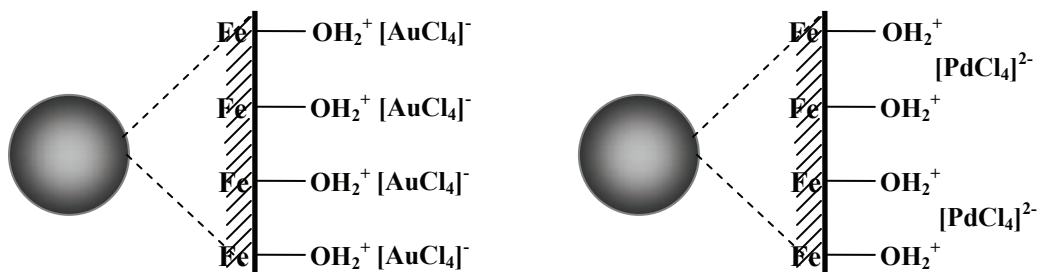
5.2 Investigation into the possible mechanism(s) responsible for the $[\text{AuCl}_4]^-$, $[\text{PdCl}_4]^{2-}$ and $[\text{PtCl}_4]^{2-}$ removal from solution using unfunctionalized SPMNs.

In this section, the possible mechanisms responsible for the removal of $[\text{AuCl}_4]^-$, $[\text{PdCl}_4]^{2-}$ and $[\text{PtCl}_4]^{2-}$ from acidic solutions are discussed. The objective of this study was to investigate whether adsorption was an efficient mechanism for the removal of these precious metals from aqueous acidic solutions. Here we will refer to SPMNs and Fe_3O_4 nanoparticles interchangeably.

5.2.1 Surface properties of SPMNs and the $[\text{AuCl}_4]^-$, $[\text{PdCl}_4]^{2-}$, $[\text{PtCl}_4]^{2-}$ interactions

The iron oxide based SPMN surface have hydroxyl groups that can accept protons and could potentially take part in complexation reactions with certain metal ion species.^[42] For the purpose of this discussion, the surface hydroxyl groups will be symbolized as $\equiv\text{Fe}-\text{OH}$. This convention is a simplification of the local structure at the SPMN surface. However, this relatively simple model of surface hydroxyl groups is assumed to be satisfactory for the modeling description of metal species adsorption.

The point of zero charge (PZC) of SPMNs is a relevant property that influences the adsorption ability of the $[\text{AuCl}_4]^-$, $[\text{PdCl}_4]^{2-}$ and $[\text{PtCl}_4]^{2-}$ species from acidic solutions onto these iron oxide materials. The PZC is the value of pH at which the adsorption of potential-determining ions on the iron oxide is zero.^[42] The PZC for SPMNs has been reported to be in the range of 6.0 to 8.2.^[42,133] At a pH less than the PZC, the $\equiv\text{Fe}-\text{OH}_2^+$ groups on the surface of the SPMNs predominate. Thus, under the experimental conditions used in these studies (solution pH < PZC), the SPMNs surface can be considered to be essentially protonated and positively charged, facilitating the adsorption of anionic metal complexes which is believed to take place *via* electrostatic interaction as illustrated by *Scheme 12*.



Scheme 12. Illustration of $[\text{AuCl}_4]^-$ and $[\text{PdCl}_4]^{2-}$ species interaction with the protonated SPMNs surface sites. Note: only a section (not drawn to scale) of SPMN surface is shown.

In *Scheme 12*, $\equiv\text{Fe-OH}_2^+$ represents a positively charged, singly coordinated hydroxyl group on the SPMN surface. Using this scenario, $[\text{AuCl}_4]^-$ complexes could electrostatically associate with the protonated surfaces of the SPMNs. The $[\text{PdCl}_4]^{2-}$ and $[\text{PtCl}_4]^{2-}$ anionic complexes could also be adsorbed *via* anion pairing as illustrated in *Scheme 12*. The relative number of protonated $\equiv\text{Fe-OH}_2^+$ surface groups could not be determined and is unknown. Therefore, it is important to point out that the stoichiometry and the interpretation thereof in the electrostatic interaction of this adsorption model is only qualitative for the unfunctionalized SPMNs.

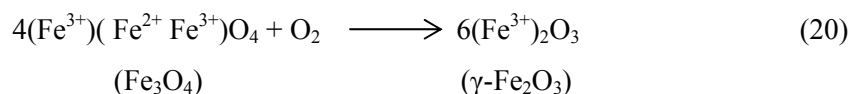
From our previous results, it was found that $[\text{PdCl}_4]^{2-}$ and $[\text{PtCl}_4]^{2-}$ adsorption efficiency strongly depended on solution pH and chloride ion concentration. From 0.5 M HCl solutions, $[\text{PdCl}_4]^{2-}$ and $[\text{PtCl}_4]^{2-}$ adsorption by SPMNs was almost negligible. However, from 0.001 M HCl solutions almost quantitative $[\text{PdCl}_4]^{2-}$ and $[\text{PtCl}_4]^{2-}$ removal and adsorption by SPMNs was achieved. The SPMNs can readily become protonated under these acidic conditions and establish an ideal situation for the anionic complexes to be adsorbed *via* anion pairing (as illustrated in *Scheme 12*). The results obtained would imply that there was competition for the available protonated sites on the surfaces of SPMNs between anionic complexes and free chloride ions in solution. In contrast, it was found that $[\text{AuCl}_4]^-$ was consistently and effectively removed from the feed solutions with molarity of 0.5 M and 0.01 M HCl. Other than the sorption rate, it was obvious that solution pH and free chloride ions have no significant effect on the adsorption efficiency of $[\text{AuCl}_4]^-$ by SPMNs, which would suggest that the mechanism responsible for $[\text{AuCl}_4]^-$ removal from the acidic solutions is different to that of $[\text{PdCl}_4]^{2-}$ and $[\text{PtCl}_4]^{2-}$. These interesting observations led us to investigate the mechanism responsible for the removal of $[\text{AuCl}_4]^-$ from solution using SPMNs as adsorbent materials.

As proposed in *Scheme 12*, it was initially expected that the $[\text{AuCl}_4]^-$ species in the acidic solutions are removed as the $[\text{AuCl}_4]^-$ complex, *i.e.* by electrostatic interaction between the anionic complexes and the protonated surface sites ($\equiv\text{Fe-OH}_2^+$) of the SPMNs. However, another plausible explanation that can govern these adsorption processes is reductive adsorption. This mechanism entails the reduction of $[\text{AuCl}_4]^-$ species at the solid-solution interface of the SPMNs in suspension followed by subsequent adsorption onto the iron oxide based solid phase. Before this is discussed further, it is necessary to first consider the dissolution and transformation of SPMNs as a result of the aqueous acidic solutions in which these experiments were conducted.

5.2.2 Dissolution and transformation of SPMNs in acidic solution

In acidic solutions, the dissolution of SPMNs could readily occur and in the process cause the release of Fe^{2+} cations from the crystal structure. The release of Fe^{2+} is believed to be energetically more favorable than the release of Fe^{3+} from the crystal structure.^[42,67] The extent of dissolution was found to be dependant on the acidic content of the aqueous solutions and the time of contact between solid and aqueous phase during sorption batch experiments. In this process, the release of Fe^{2+} from the crystal structure of SPMNs results in cation deficient sites³.

In addition to the dissolution of the SPMNs, the presence of dissolved oxygen in the aqueous phase is understood to have an affect on the composition of the SPMNs during the sorption batch experiments (*Chapter One*). A transformation process of SPMNs from magnetite (Fe_3O_4) to maghemite ($\gamma\text{-Fe}_2\text{O}_3$) is thought possible. When magnetite ($\text{Fe}^{3+}(\text{Fe}^{2+}\text{Fe}^{3+})\text{O}_4$) becomes progressively oxidized, the Fe^{2+} is converted to Fe^{3+} . The oxidation results in a defective structure ($\gamma\text{-Fe}_2\text{O}_3$) with an average of 2/3 of vacant cation sites per unit cell.^[42] The following equation is proposed to represent the magnetite-maghemite transformation process:



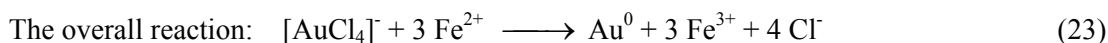
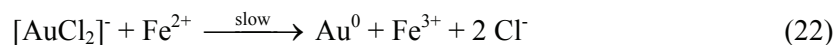
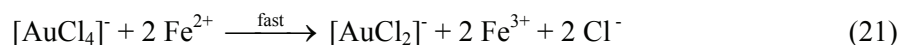
Due to similarities between Fe_3O_4 and $\gamma\text{-Fe}_2\text{O}_3$, their properties are almost identical and therefore it is difficult to distinguish between these two crystalline iron oxide structures with XRD analysis. Also, under these conditions, it is possible for hematite ($\alpha\text{-Fe}_2\text{O}_3$) to form. The latter structure however, forms only under high thermal conditions.^[42] Therefore, in these studies, it was more than likely that the solid iron oxide phase used in the sorption batch experiments were $\gamma\text{-Fe}_2\text{O}_3$ or a mixture of the Fe_3O_4 and $\gamma\text{-Fe}_2\text{O}_3$ crystalline phases.

5.2.3 Proposed mechanism of $[\text{AuCl}_4]$ adsorption and removal from acidic solutions

Other than $[\text{AuCl}_4]^-$ adsorption initiated by electrostatic interactions, another plausible explanation for removal of $[\text{AuCl}_4]^-$ from aqueous acidic solutions and subsequently adsorption by SPMNs could be attributed to reductive adsorption. Previous studies on the adsorption of gold complexes on mineral surfaces have shown that gold species present in solution can be reduced to metallic gold after exposure to oxidizable (*i.e.* electron donating) mineral surfaces.^[134,135]

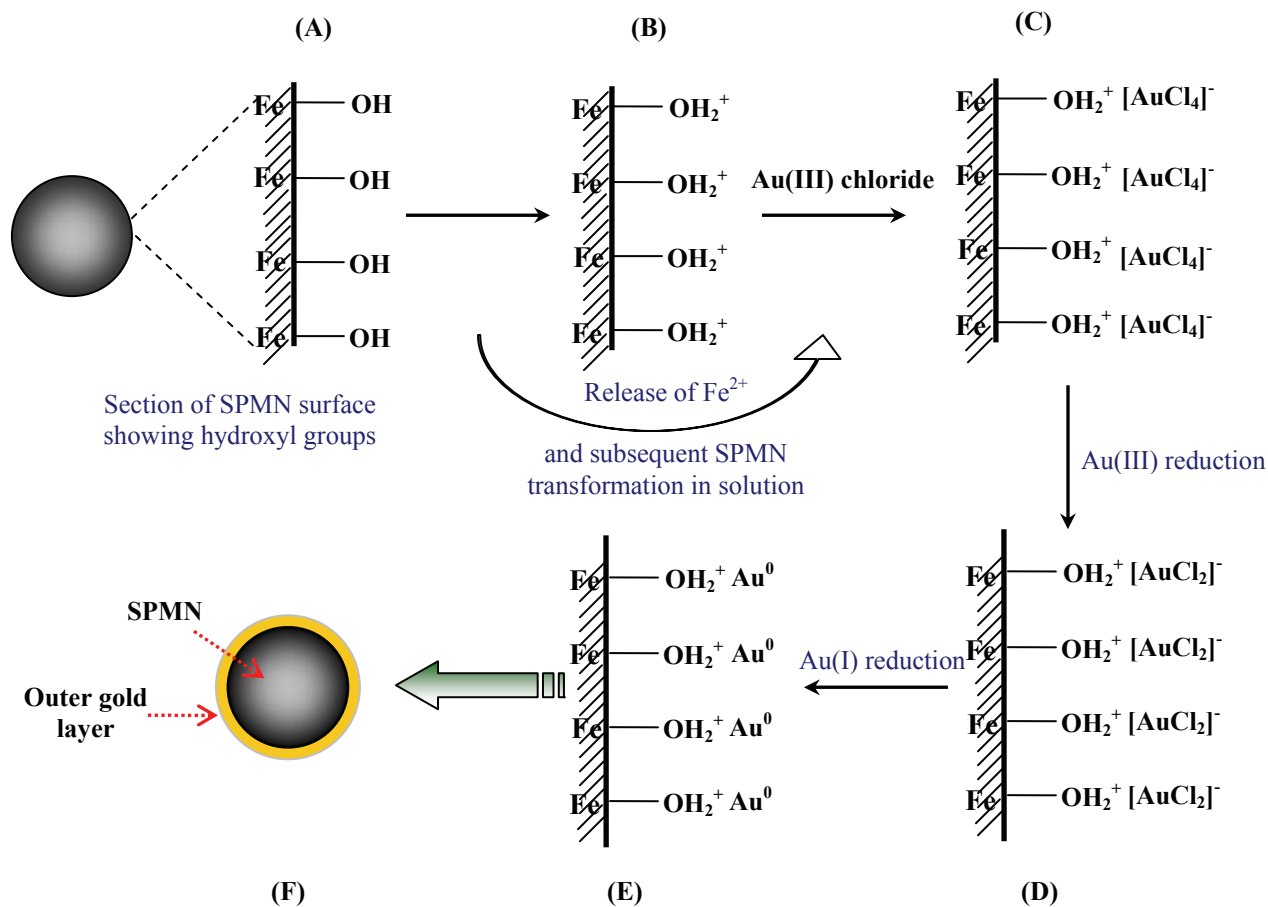
³ For further studies on iron dissolution, refer to the supplementary section A1.

Furthermore, Berrodier *et al.*^[136] has reported that gold species can be reduced and precipitated by reacting with Fe²⁺ bearing minerals or with Fe²⁺ released by the dissolution of such minerals. As already mentioned, in the sorption batch experiments, a certain degree of SPMNs dissolution occurred as a result of the aqueous acidic media in which the experiments were performed, thus causing the release of Fe²⁺ ions during the transformation processes. The release of Fe²⁺ from the crystal structure of SPMNs was energetically more favorable than the release of Fe³⁺.^[42,67] In addition to this information, it was shown in *Chapter One, Scheme 1* that classical refining methods separate gold from PGMs with the use of a mixture of SO₂/FeSO₄ as reducing agents. The Fe²⁺ species could provide electrons needed for the reduction of [AuCl₄]⁻. Therefore, in our experiments, oxidation-reduction reactions between Fe²⁺ and Au³⁺ are possible to occur in solution and at the surface of the SPMNs. The following reaction stoichiometry for the reduction of Au(III) to Au(I) and then possibly to Au(0) by Fe²⁺ in solution as a result of the dissolution and transformation of SPMNs or at the surface of the SPMN-iron oxide interface can be expressed by the following equations:



In above equations, [AuCl₄]⁻ species is the oxidant and Fe²⁺ is the reducing agent. It was proposed in *equation 21* that the reduction of Au(III) to Au(I) is associated with rapid kinetics, whereas the reduction shown in *equation 22* is associated with slow kinetics.

A realistic mechanism for the removal of [AuCl₄]⁻ species from acidic solutions would involve simultaneous dissolution, transformation, reduction and adsorption processes as shown in *Scheme 13*. The model assumes that gold migrates as a chloride complex owing to the acid and chloride-rich solutions. The gold complexes could then associate or interact with the iron oxide surfaces (Fe₃O₄/γ-Fe₂O₃) by strong electrostatic interactions. Gold is reduced and precipitates by oxidation-reduction reactions between Fe²⁺/Fe³⁺ and Au³⁺/Au⁰ at the solid-solution interface (*equation 23*). It has been reported that Au⁰ (colloidal gold) has a slight negative surface charge therefore enabling electrostatic interaction.^[137] Therefore favorable electrostatic interactions also exist between negatively surface charged colloidal gold and positively charged iron oxides.



Scheme 13. Simultaneous dissolution, transformation, reduction and adsorption of gold from aqueous acidic solutions onto SPMN-iron oxide interface.

A - small section of SPMN surface illustrating surface hydroxyl groups

B - protonated SPMN surface sites ($\equiv\text{Fe}-\text{OH}_2^+$) as a result of acidic content of aqueous solutions containing the $[\text{AuCl}_4]^-$ anionic complexes. At this stage the dissolution and transformation processes are initiated.

C - electrostatic interaction between $[\text{AuCl}_4]^-$ anionic complexes and $\equiv\text{Fe}-\text{OH}_2^+$

D - electrostatic interaction between $[\text{AuCl}_2]^-$ anionic complexes and $\equiv\text{Fe}-\text{OH}_2^+$

E - electrostatic interaction between colloidal gold (Au^0) and $\equiv\text{Fe}-\text{OH}_2^+$

F - Formation of Au-enriched SPMN-iron oxide nanoparticles illustrating a gold coating around the SPMN-iron oxide nanoparticles.

5.2.4 Effect of iron in solution on removal and adsorption of gold species

The effect of iron in solution (as a result of SPMN dissolution) on the amount of gold removed from aqueous solution and adsorbed by SPMNs was investigated. As for previous experiments, the solid SPMN phase was in contact with the aqueous phase containing a fixed, standard $[\text{AuCl}_4]^-$ concentration in 0.5 M HCl. After contact for the desired time periods ranging from 1 to 450 minutes, the solid phase was separated from the aqueous phase *via* magnetic sedimentation. The supernatant collected was then analyzed for gold as well as iron content by ICP-AES. From the analysis results obtained and using mass balance equations, the amount of gold loaded per gram of SPMN material was determined. The results obtained are shown in *Figure 30*, illustrating the amount of gold loaded as a function of free iron species in solution.

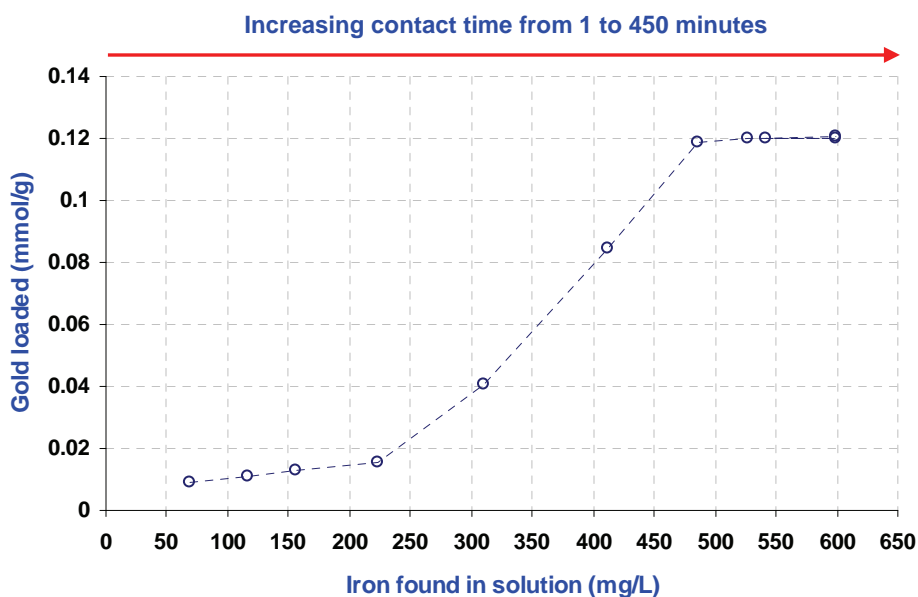


Figure 30. Effect of iron species in solution on the amount of gold loaded onto SPMNs. Single-metal solution experiment in 0.5 M HCl. Experimental conditions – SPMNs used: 10 mg; Au(III) concentration used: 20.5 mg/L; Total metal aqueous phase: 10 mL; Temperature: $21 \pm 1^\circ\text{C}$.

In this study it was assumed that the free iron in solution was mainly Fe^{2+} but it is likely that Fe^{3+} is also present in some quantity depending on the amount of dissolution and subsequent oxidation that occurred. We were not able to determine the oxidation states of these iron species in the solutions. It was only possible to determine the total amount (mg/L) of free iron species in solution as shown in *Figure 01*. As was already mentioned, it is energetically more favorable to release Fe^{2+} from the SPMN structure than the Fe^{3+} species.^[42,67]

As expected, there is more iron present in solution with increasing contact time. Also, with this increasing iron content in solution, the amount of gold adsorbed onto the SPMN-iron oxide surface increased. With increasing iron species content in solution, the amount of gold loaded per gram SPMN material increases periodically. Initially, with an iron concentration up to *ca* 225 mg/L, less than 18×10^{-5} mmol/g gold is adsorbed. This is followed by a steady increase in gold loading up to *ca* 12×10^{-4} mmol/g, after which equilibrium loading is reached at an iron concentration exceeding 485 mg/L. At the point where equilibrium is reached, less than 0.1 mg/L gold was detected by ICP-AES in the effluents, indicating almost quantitative gold adsorption. Moreover, in some cases, the gold concentrations could not be accurately determined by ICP-AES, since it was below the detection limit of the instrument, suggesting that the amount of gold present in the effluents is almost negligible.

This result (*Figure 30*) suggested that the free iron species in solution have an effect on the gold removal and the adsorption processes. It is therefore consistent with our proposed reductive-adsorption mechanism (*equations 21 – 23* and *Scheme 13*), which states that the Fe^{2+} species could reduce the Au^{3+} species. According *equations 21 – 23*, 61.5 mg/L Fe^{2+} was needed to reduce all of the 20.5 mg/L Au^{3+} initially in solution. The amount of free iron species in solution as shown in *Figure 30* is probably a mixture of the two oxidation states of iron, therefore the total concentration could not be attributed to only Fe^{2+} species. Due to lack of information, we could not predict the exact stoichiometry of the possible reduction mechanism.

5.2.5 Gold spectral analysis

The main purpose of this study was to investigate the Au(III) speciation in solution to get some insight into the processes governing the mechanisms of adsorption at the solid-solution interface. In this regard, series of UV-Visible experiments were performed on the effluents collected after the sorption batch experiments conducted in 0.01 M HCl and 0.5 M HCl solutions, respectively.

A complete review of the aqueous speciation of gold is beyond the scope of this thesis. The possible role of hydroxy and hydroxy-chloride complexes must be considered. The stability and bonding characteristics of these species have been investigated and reported elsewhere using Raman, UV-VIS, EXAFS and NMR spectroscopies.^[138] However in acidic chloride-rich solutions, hydroxy and hydroxy-chloride species could be ruled out and gold is essentially in the anionic $[\text{AuCl}_4]^-$ complex form.

5.2.5.1 Results of UV-Visible analysis of Au(III) species in 0.01 M HCl solution

The UV-Vis absorption spectrum of the tetrahedral $[\text{AuCl}_4]^-$ complex in 0.01 M HCl solution was collected and shown in *Figure 31*. The spectrum of this solution exhibits two absorption maxima at $\lambda = 229$ nm and $\lambda = 315$ nm as a result of the presence of $[\text{AuCl}_4]^-$ ions. The presence of these two absorption maxima enabled the recording of their changes with time, *i.e.* the concentration changes in the course of the reaction.

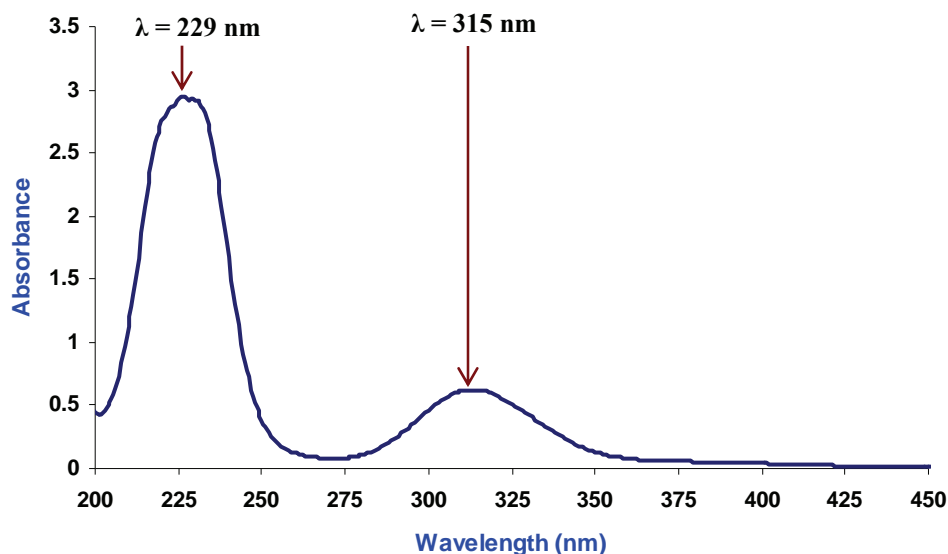


Figure 31. The UV-Vis absorption spectrum of feed solution containing 20 mg/L $[\text{AuCl}_4]^-$ in 0.01 M HCl solution at ambient temperature. The absorption maxima are visible at $\lambda = 229$ nm and $\lambda = 315$ nm as a result of present $[\text{AuCl}_4]^-$ ions. Experimental conditions: pH 0.43; temperature: 21 ± 1 °C.

The absorption spectrum of $[\text{AuCl}_4]^-$ shown in *Figure 31* is essentially that of the feed solutions used during the sorption batch experiments as reported earlier. Spectrophotometric analysis was then also done on the effluents collected after the contact of aqueous phases containing $[\text{AuCl}_4]^-$ species in 0.01 M HCl with solid phases, SPMNs. The contact times in these experiments ranged from 2 – 90 minutes. The changes in the $[\text{AuCl}_4]^-$ absorption maxima with increasing contact times were monitored, taking into consideration that with increasing contact time more Fe^{2+} species are expected to be at the surface of the SPMN-iron oxide interface and also in solution. The results of these studies are shown in *Figure 32*. Each absorption spectrum shown in *Figure 32* represents the changes that occurred after the indicated contact times.

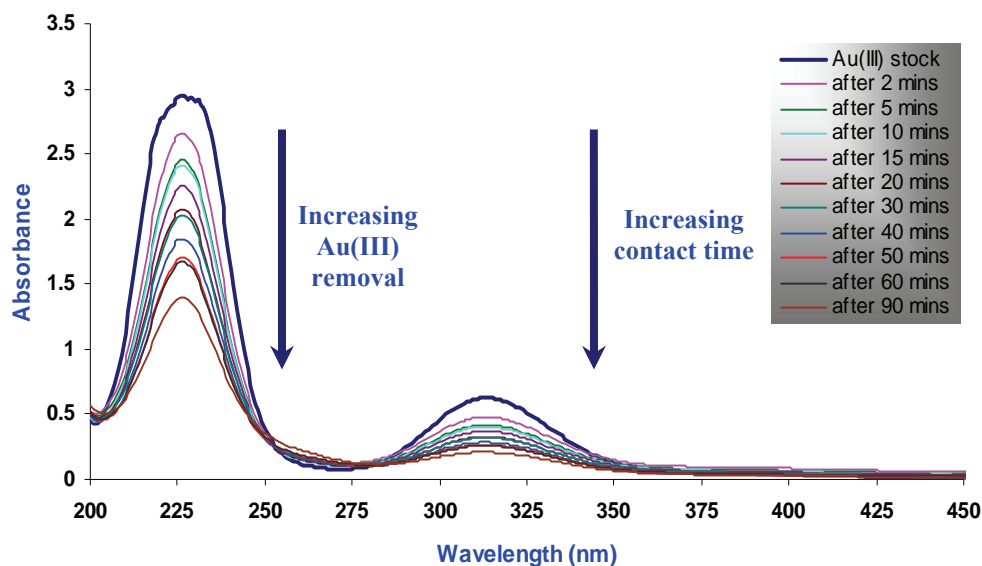


Figure 32. The UV-Vis absorption spectra of gold species in 0.01 M HCl solution after various contact times. Experimental conditions - mass SPMNs used: 10 mg; contact times range: 2 – 90 minutes, total metal aqueous phase: 10 mL, HCl concentration: 0.01 M; temperature: $21 \pm 1^\circ\text{C}$. The “bold” spectrum is that of the standard $[\text{AuCl}_4]^-$ feed solutions.

As can be seen in Figure 32, in all cases the absorbance maxima at $\lambda = 229 \text{ nm}$ and $\lambda = 315 \text{ nm}$ decreased as a function of contact time, and this fact indicated decreasing $[\text{AuCl}_4]^-$ concentration in solution. This result was confirmed by ICP-AES as shown in Figure 33, demonstrating decreasing gold concentration in solution with increasing contact time.

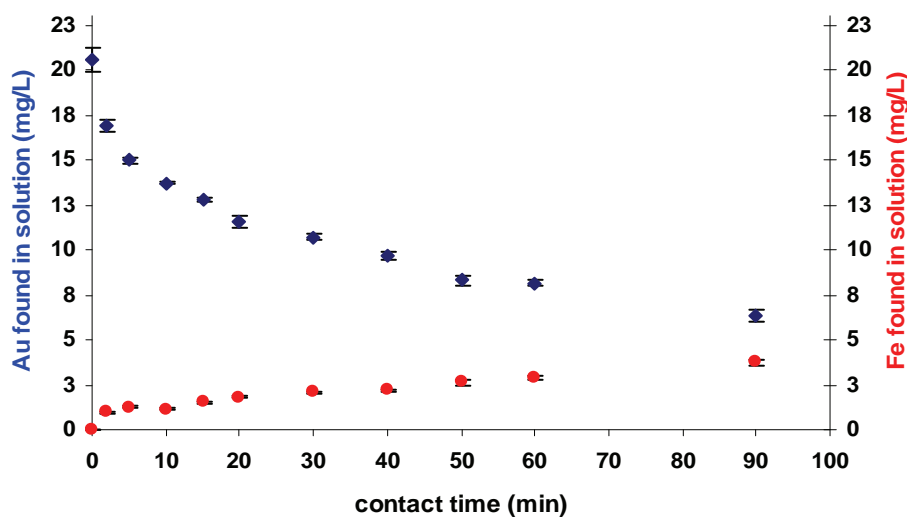


Figure 33. Amount of gold and iron left in solution with increasing contact time as determined from ICP-AES. The experimental conditions were same as for Figure 30.

As can be seen from *Figure 33*, the effluents collected after sorption batch experiments contained certain amounts of free iron species as a result of the SPMN dissolution and transformation processes (*Scheme 13*). As discussed in *section 5.2.3* and shown in *equation 23*, the presence of Fe^{2+} ions in solution could in principle function as a reducing agent and thus reduce the Au^{3+} to Au^+ species. As was found, with increasing contact time, there were more iron species in solution.

The absorption maxima intensity changes (*Figure 32*) which are normally associated with ligand-to-metal charge transfer transitions (LMCT) are a result of the release of chloride ligands in the first coordination sphere of four-coordinated $[\text{AuCl}_4]^-$ complex. Therefore, the changes in the intensity and positions of LMCT bands in the UV-Vis spectra of the $[\text{AuCl}_4]^-$ species with increasing contact time are consistent with the reduction of $[\text{AuCl}_4]^-$ to $[\text{AuCl}_2]^-$ or even complete reduction to colloidal gold as proposed in *equation 22*. Furthermore, the spectra displayed two isobestic points, indicating the occurrence of at least two predominant species in solution which suggested the presence of only $[\text{AuCl}_4]^-$ and $[\text{AuCl}_2]^-$ in solution.

5.2.5.2 Results of UV-Visible analysis of Au(III) species in 0.5 M HCl solution

To conclusively prove that reduction of $[\text{AuCl}_4]^-$ to $[\text{AuCl}_2]^-$ occurred in solution, we conducted similar experiments but in HCl solutions of 0.5 M and monitored spectrophotometrically the changes in the absorption maxima. The higher HCl concentration should ensure the presence of more iron species in solution, which was expected to have an effect on the reduction and consequently adsorption mechanisms.

As was done previously, sorption batch experiments were conducted under similar experimental conditions as described in *section 5.2.5.1*, except that the $[\text{AuCl}_4]^-$ feed solution was in 0.5 M HCl solution. An identical $[\text{AuCl}_4]^-$ UV-Vis absorption spectrum was obtained as shown in *Figure 31*. The effluents collected after certain contact times were analyzed and measured with UV-Vis and the absorption maxima (at $\lambda = 229$ and $\lambda = 315$ nm) intensity changes were monitored. The results of these studies are shown in *Figure 34*.

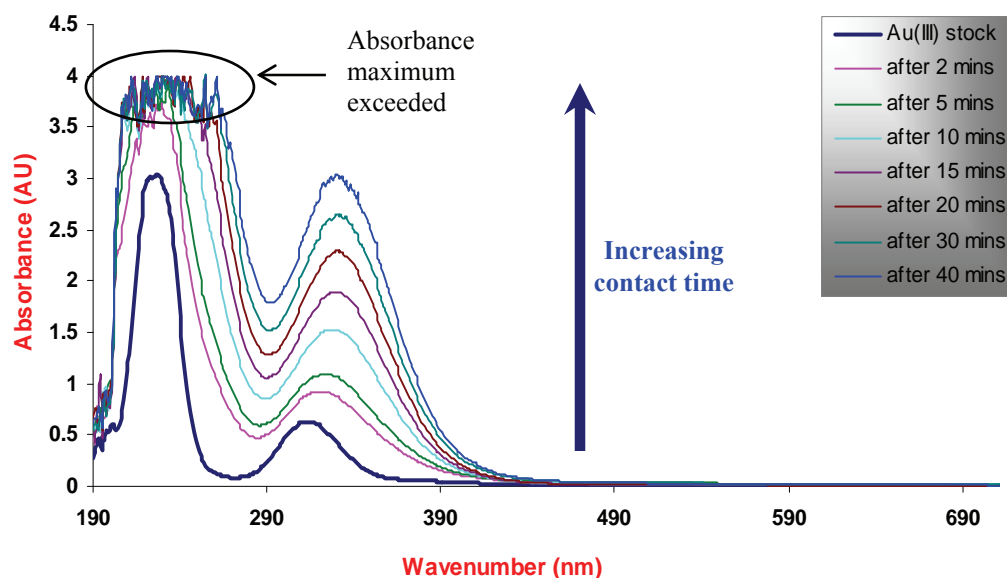


Figure 34. UV-Vis absorption spectra of Au(III) in 0.5 M HCl solution after various contact times illustrating a shift in the absorption peaks. Experimental conditions - mass SPMNs used: 10 mg; contact times range: 2 – 40 minutes, total metal aqueous phase: 10 mL, HCl concentration: 0.5 M; temperature: $21 \pm 1^\circ\text{C}$. The “bold” spectrum is that of the standard $[\text{AuCl}_4]^-$ feed solutions.

In 0.5 M HCl there is a significant difference in the absorption spectra as compared to the absorption spectra in 0.01 M HCl (Figure 32). As can be seen in Figure 34, with increasing contact time there is an increase in the absorption maxima at $\lambda = 229$ and $\lambda = 315$ migrates to a higher wavelength at $\lambda = 334$, suggesting the formation of new species with higher molar absorptivity than $[\text{AuCl}_4]^-$ species. The increase and shift in absorbance in the UV-Vis can most likely be attributed to the formation of $\text{Fe}^{\text{III}}\text{Cl}_n^{(3-n)}$ species (for $n = 3, 4, 5, 6$) as a result of increasing reduction of Au^{3+} to Au^+ with simultaneous oxidation of Fe^{2+} to Fe^{3+} species. Since there are excess amounts of Fe^{3+} and chloride ions in the solution, this was favorable for the formation of the iron(III) complex.

To confirm this, a series of UV-Vis experiments were performed to monitor the changes in the absorption maxima of a standard Fe^{3+} stock solution with similar concentrations as found in the effluents of the samples. The absorption spectrum of the Fe^{3+} stock solution is shown in Figure 35. The Fe^{3+} stock solution was prepared from the ferric salt, $\text{FeCl}_3 \cdot 6\text{H}_2\text{O}$. Moreover, the same quantities of SPMNs were contacted for the same amount of time in 0.5 M HCl solutions (without the presence of gold in these solutions) and the changes in the absorption maxima intensity were monitored spectrophotometrically.

The UV-Vis spectrum of the Fe^{3+} stock solution is shown in Figure 35 and the changes in the absorption maxima for the SPMNs with time is shown in Figure 36.

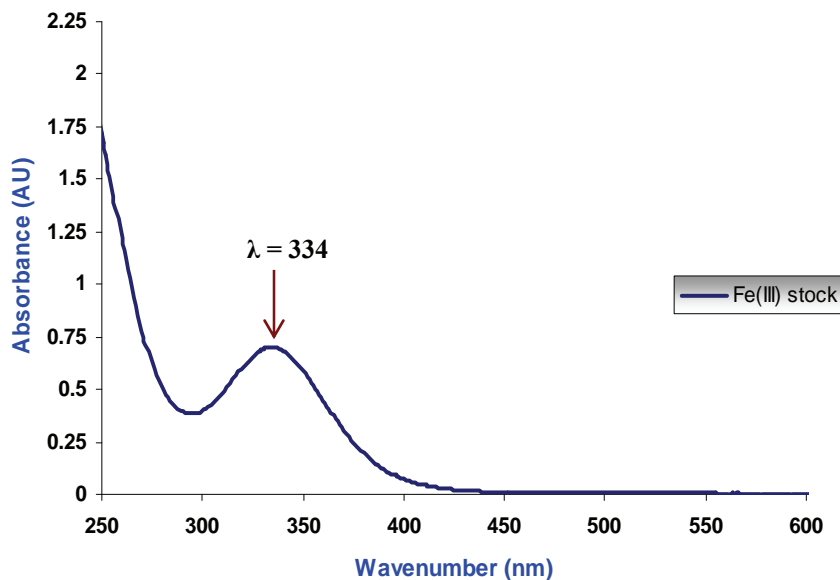


Figure 35. The UV-Vis absorption spectrum of Fe(III) stock solution in 0.5 M HCl solution. The absorption maxima is observed at $\lambda = 334$ nm.

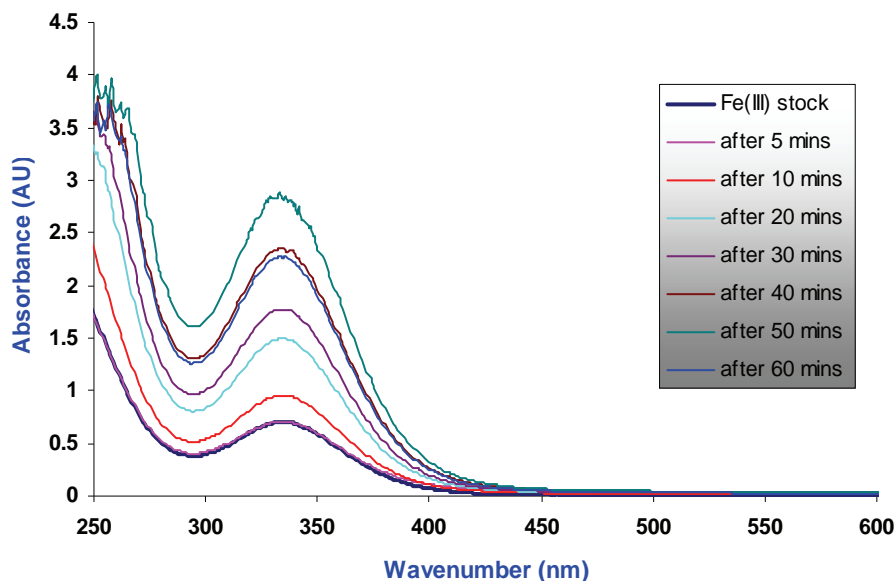


Figure 36. The UV-Vis absorption spectra of the formation of iron species in 0.5 M HCl solution after various contact times. Experimental conditions- mass SPMNs used: 10 mg; contact times range: as shown in figure legend, HCl concentration: 0.5 M; temperature: $21 \pm 1^\circ\text{C}$. The “bold” spectrum is that of the standard iron solutions.

As can be seen from *Figure 36*, there is a significant increase in the absorption maxima at $\lambda = 334$ nm, which indicates the increasing formation of $\text{Fe}^{\text{II}}\text{Cl}_n^{(3-n)}$ species. This is in accordance with what was expected, since with increasing contact time more iron is present in solution. Therefore, from this result can be concluded that the increase in the absorption maxima intensity is due to the formation of $\text{Fe}^{\text{III}}\text{Cl}_n^{(3-n)}$ species, which in turn confirms the reduction mechanism as illustrated in *equations 21 – 23*.

5.2.6 Physical characterization of gold coated SPMNs.

Transmission electron microscopy (TEM) analysis was performed after a single preliminary sorption experiment to investigate whether gold was adsorbed onto the surface of SPMNs and to evaluate the gold-enriched SPMN morphology and size. In this regard, a known volume of a 23 mg/L $[\text{AuCl}_4]^-$ solution in 0.5 M HCl was in contact with the solid phase by agitation for 50 minutes. The solid phase was then separated from the aqueous phase by magnetic decantation and the effluent analyzed with TEM. It was found that gold was efficiently removed from the solution and almost quantitatively adsorbed by SPMNs. In *Figure 37* is shown the TEM micrograph depicting pseudo-trigonal shaped particles with average diameter of 12 ± 1.7 nm. The pseudo-trigonal particles are characteristic of colloidal gold.^[139] These findings support the hypothesis of Au(III) reduction by the SPMNs to Au(0). However, since this was only a preliminary experiment it is necessary to conduct a more systematic study to conclusively proof the hypothesis by taking into account that poorly ordered iron oxide-SPMNs have a high affinity for gold species.

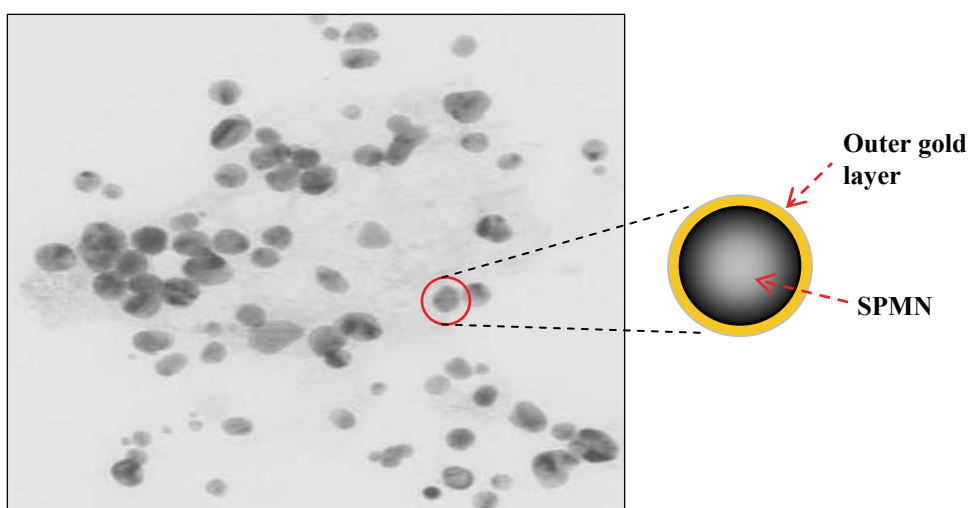


Figure 37. TEM images of the SPMNs after sorption of gold.

The solid iron oxide – SPMN phase collected after the preliminary gold sorption experiment was dried under ambient conditions after separation from aqueous phase. Elemental composition analysis by energy Dispersive X-ray spectroscopy (EDX) was then done on this dried sample. The result is shown in *Figure 38* below.

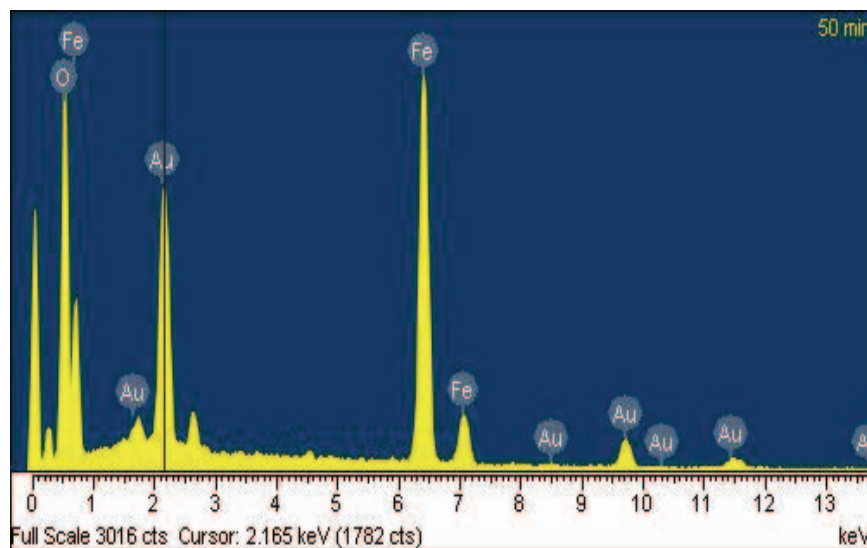


Figure 38. EDX analysis of gold-enriched SPMN materials.

EDX analysis shows that the main composition of the material is iron, oxygen and gold. The presence of iron and oxygen confirms that the material is an iron oxide and the presence of gold confirms the adsorption of gold species by the SPMNs. As illustrated in *Figure 38*, we propose that the gold adsorbed was coated as an outer layer onto the surface of the SPMNs. However, we still need to investigate this hypothesis. Since the SPMNs before the gold adsorption was approximately 10 nm in diameter and from the result of the pseudo-trigonal shaped particles obtained (*Figure 37*), we can conclude that the gold coating onto the SPMNs is approximately 2 – 3 nm in width. This is still the topic of much research and worth looking at further.

Chapter Six

Conclusions and Recommendations

In this study a simple, cost-effective method for superparamagnetic magnetite (Fe_3O_4) nanoparticles (SPMNs) synthesis were presented. The SPMNs were produced *via* chemical coprecipitation of ferrous (Fe^{2+}) and ferric (Fe^{3+}) ions by a base ($\text{NH}_3\cdot\text{H}_2\text{O}$), in aqueous solutions under aerobic and anaerobic conditions. The results showed that performing the experiments under inert conditions not only protects the formed SPMNs from critical oxidation but also reduced the nanoparticle size. From TEM analysis, it was found that the SPMN size was reduced from about 9 nm (when synthesis was performed under aerobic conditions) to about 5 nm (when synthesis was performed under anaerobic conditions). Furthermore, it was found that most of the SPMNs was spherical in shape and were monodispersed. The formation of relatively pure and crystalline SPMNs was proven by XRD analysis, but an even more important result in this work is the fact that the final black products exhibited strong magnetization when exposed to an external magnetic field. Indeed, the superparamagnetic behavior was confirmed by VSM analysis, which illustrated zero coercivity and zero remanance on the magnetization curve with a saturation magnetization of 28×10^3 A/m. The surface area analysis results illustrated that the SPMNs was porous with average pore diameters of 61 ± 12 Å. The BET surface area of the SPMNs was reported to be 160 ± 0.77 m²/g.

The synthesized SPMNs were then coated with silica to enhance their stability in aqueous solution and also endowed them with surface properties which enabled surface functionalization. The synthesis of silica coated SPMNs were found to be challenging. From TEM analysis, it was observed that the morphology varied from spherical to irregular shape with clear evidence of SPMN cluster formation and silica aggregation. These could be attributed to the synthetic parameters such as the type of alcohol used, amount of catalyst (ammonia aqueous), amount of silica precursor (TEOS), and the pH of the solution. However, the best results showing more or less core-shell structure (SPMN-silica composite) as evidenced by TEM analysis was used for further studies which included the surface functionalization of the silica coated SPMNs. From FT-IR analysis it was stated that the silica was adsorbed on the SPMNs by Fe-O-Si bonds. Sharp

absorption bands at 1100 cm^{-1} in the FT-IR spectrum proved the formation of the silica network on the SPMNs. The absorption bands between $3200 - 3600\text{ cm}^{-1}$ revealed the presence of surface silanol (Si-OH) groups on the silica layer coated onto the SPMNs. The surface area analysis results showed that the silica coated SPMNs were also porous with average pore sizes of 97.16 \AA . The BET surface area of the silica coated SPMNs was reported as $183 \pm 0.53\text{ m}^2/\text{g}$.

Due to the existence of these abundant silanol groups on the silica layer, silica-coated SPMNs could easily be activated to provide the surface of silica-coated SPMNs with functional groups of choice. Herein, the surface of the silica-coated particles was functionalized with free amine methoxysilane ligands. The surfaces of these silica-coated SPMNs were functionalized with (3-aminopropyl)trimethoxysilane and N-[3-(trimethoxysilyl)propyl]-ethylene diamine by a silanization reaction in order to obtain potential ion-exchanger materials with **(1)** monoamine and **(2)** ethylenediamine functionalities. Elemental analysis confirmed that the amine-methoxysilane ligands were grafted on average onto the surface of the silica coated SPMNs *via* two methoxy groups. The average ligand concentrations were calculated from the weight percentage of nitrogen and found to 0.76 mmol/g and 0.87 mmol/g for material **(1)** and **(2)**, respectively. FT-IR analysis showed the presence of amino as well as anchored propyl groups on the silica coated SPMNs, which was attributed to that of the amine methoxysilane ligands, thus confirming the successful surface functionalization. No surface area analysis was done on these modified materials.

The performance of the synthesized bare SPMNs and modified materials for Au(III), Pd(II), and Pt(II) removal from diluted chloride-rich HCl solutions were tested for magnetic nano-adsorbent and ion exchanger materials, respectively. Batch laboratory experiments were carried out to investigate the effect of various parameters such as initial metal ion concentration, effect of contact time, acidic content of the aqueous solutions, and chloride ion concentration on the adsorption ability using these adsorbent materials. In these solutions, the precious metals were in the anionic metals complex forms $[\text{AuCl}_4]^-$, $[\text{PdCl}_4]^{2-}$, $[\text{PtCl}_4]^{2-}$ and the surface sites of materials **(1)** and **(2)** was essentially protonated. It was postulated that the mechanism responsible for the removal of these precious metals from aqueous solution and subsequent adsorption was due to electrostatic interaction and ion exchange. It was observed that removal and adsorption efficiency was directly related to the HCl solution concentration as well as the quantity of adsorbent material used during sorption batch experiments.

Adsorption data of $[\text{AuCl}_4]^-$ sorption onto **(1)** and **(2)** were analyzed in terms of the Langmuir and Freundlich isotherm models. The results showed that the Freundlich model is not adequate

for modeling the adsorption of $[\text{AuCl}_4]^-$ for both materials **(1)** and **(2)**. In contrast, it was found that the adsorption data obtained were in reasonably good agreement with the Langmuir model, thus indicating monolayer coverage. Applying the Langmuir model, a maximum $[\text{AuCl}_4]^-$ loading capacity of 0.072 mmol/g (14.182 mg/g) and 0.111 mmol/g (21.863 mg/g) for **(1)** and **(2)**, respectively was determined.

Time dependant studies conducted in 0.5 M HCl showed that the rate of $[\text{AuCl}_4]^-$, $[\text{PdCl}_4]^{2-}$ and $[\text{PtCl}_4]^{2-}$ removal using materials **(1)** and **(2)** were very slow. This phenomenon was attributed to the porous structure of the materials, suggesting that diffusion into and out of pores where responsible for the observed slow sorption kinetics. However, results obtained of similar studies conducted in an even more diluted media of 0.01 M HCl indicated improved sorption kinetics and higher loading capacities. Generally, the efficiency and the rate of complex ion removal by material **(2)** was found to be faster than that of material **(1)**, owing to the higher relative amine ligand capacity as determined by elemental analysis. Therefore, this result suggested that chloride ion content in solution had a significant effect on the sorption efficiency of these precious metals from aqueous acidic solution. In these acidic aqueous solution conditions, the materials should be efficiently protonated and therefore competition exist between the anionic chloro-complexes, $[\text{AuCl}_4]^-$, $[\text{PdCl}_4]^{2-}$, $[\text{PtCl}_4]^{2-}$ and the free chloride ions in solution for the protonated binding sites in the backbone of the materials **(1)** and **(2)**.

Studies were therefore conducted to determine the effect of free chloride ion concentration in solution on the removal efficiency of $[\text{AuCl}_4]^-$ using materials **(1)** and **(2)**. As expected it was found that increasing chloride ions in solution was accompanied with a decrease in $[\text{AuCl}_4]^-$ loading capacity and distribution coefficients, which suggested competition for binding sites and confirmed that the likely mechanism responsible was ion-exchange.

From our investigations involving the use of unfunctionalized SPMNs, it was found that $[\text{PdCl}_4]^{2-}$ and $[\text{PtCl}_4]^{2-}$ adsorption efficiency strongly depended on the HCl and chloride ion concentration in solution. From a 0.5 M HCl solution, $[\text{PdCl}_4]^{2-}$ and $[\text{PtCl}_4]^{2-}$ removal was almost negligible. However, from a 0.001 M HCl solution almost quantitative adsorption was achieved. The results obtained implied that there was competition for the available protonated sites on the surface of SPMNs between anionic complexes and free unbound chloride in solution. The SPMNs are essentially protonated under these acidic conditions as a result of their PZC and establish an ideal situation for the anionic complexes to be adsorbed *via* anion pairing. On the contrary, it was found that $[\text{AuCl}_4]^-$ was almost consistently and effectively removed from the feed solutions of 0.5 M and 0.01 M HCl, with fast a relatively fast rate of removal. The

maximum loading capacity of $[\text{AuCl}_4]^-$ onto SPMNs predicted by the Langmuir model was 0.071 mmol/g (13.984 mg/g). These interesting observations led us to investigate the mechanism responsible for in particular the removal of $[\text{AuCl}_4]^-$ species from solution using SPMNs as adsorbent materials. How these precious metal species are removed from aqueous acidic solutions is not yet well resolved, but it was suspected that the removal of $[\text{AuCl}_4]^-$ from aqueous acidic solutions and the subsequent adsorption was due to mainly electrostatic interaction between the protonated, positively charged surface sites on the SPMNs and the anionic metal complexes *via* an ion exchange mechanism.

In order to learn about the mechanism of adsorption of $[\text{AuCl}_4]^-$ from aqueous acidic solutions onto SPMNs, the speciation of these metals in solution was investigated. In this regard, a series of sorption batch experiments were conducted, whereby the amount of gold adsorbed as a function of contact time was determined. The effluents collected *via* magnetic decantation after each contact time was analyzed with UV/Visible spectroscopy as is, without any dilution. The UV/Vis studies indicated that $[\text{AuCl}_4]^-$ in aqueous solution was reduced spontaneously on the SPMN surfaces, with accompanying oxidation of SPMNs in solution. Spectral shifts, absorption maxima intensity changes, and the presence of an isobestic point furnished information on changes in the speciation of dissolved gold initially present in solution. The decrease in the absorption maxima intensity, *i.e.* ligand-to-metal charge transfer (LMCT) bands was consistent with a “loss” of chloride ligands in the first coordination sphere of gold suggesting reduction. It was believed that prior to reduction, gold species were associated to the SPMN surfaces *via* an electrostatic interaction. The reductant was the free Fe^{2+} species in solution and at the surface of SPMN-iron oxide interface caused by the dissolution and transformation processes of SPMNs in acidic solutions. In our experiments, oxidation-reduction reactions between Fe^{2+} and Au^{3+} are believed to occur in solution and at the surface of the SPMNs, causing the adsorption of gold in the form of an unknown oxidation state. It could either be three, one or even colloidal gold. Our results suggested that poorly ordered iron oxides are highly efficient in trapping gold from solutions thanks to high surface area and surface reactivity, due to the small size of the SPMNs.

The objectives of this study as given in *Chapter 1, page 20*, have mainly been met. Therefore, in this thesis, the feasibility of using SPMNs and amine functionalized silica-coated SPMNs for the removal and adsorption of $[\text{AuCl}_4]^-$, $[\text{PdCl}_4]^{2-}$ and $[\text{PtCl}_4]^{2-}$ from dilute chloride-rich HCl solutions has been demonstrated.

Future work:

- Acid-base titrations of SPMN dispersions can be carried out to estimate the number of surface sites of $-\text{FeOH}$, $-\text{FeOH}_2^+$ and $-\text{FeO}^-$ types as a function of pH. This would enable us to get a better understanding of the surface properties of the SPMNs.
- More in depth mechanistic studies which would include the investigation of the interaction between $[\text{AuCl}_4]^-$, $[\text{PdCl}_4]^{2-}$ and $[\text{PtCl}_4]^{2-}$ and the active surface sites.
- A more detailed investigation of various parameters on the removal of $[\text{AuCl}_4]^-$, $[\text{PdCl}_4]^{2-}$ and $[\text{PtCl}_4]^{2-}$ from dilute chloride-rich HCl solutions.
- UV-Vis spectroscopy studies on the effluents collected after the sorption batch experiments in a wider range of HCl solution concentrations. This would give us a better understanding of the speciation of the metal species in solution and in the process the mechanism responsible for the removal of the anionic metal complexes.

References:

- [1] H. Wolf, *Metall (Berlin, 1914-34)* **1958**, 12, 585.
- [2] C.-H. Kim, S. I. Woo, S. H. Jeon, *Industrial & Engineering Chemistry Research* **2000**, 39, 1185.
- [3] B. K. Miremadi, R. C. Singh, Z. Chen, S. R. Morrison, K. Colbow, *Precious Metals* **1992**, 16th, 169.
- [4] M. J. Abrams, *Precious Metals* **1992**, 16th, 165.
- [5] A. H. Neal, *Precious Met., Proc. Int. Precious Met. Inst. Conf., 10th* **1986**, 455.
- [6] World Gold Council, 2001. Gold Demand Trends, February, 23, pp. 34.
- [7] M. J. Viljoen, *South African Journal of Geology* **1999**, 102, 221.
- [8] H. Renner, *Ullmann's Encyclopedia of Industrial Chemistry, Vol. A21*, fifth ed., VCH Publishers, **1992**.
- [9] R. I. Edwards, W. A. M. t. Riele, G. J. Bernfield, *Recovery of the platinum-group metals (technology of the Platinum-group metals), Vol. A1*, Springer, Berlin, **1986**.
- [10] M. J. Cleare, R. A. Grant, P. Charlesworth, *Separation of the platinum-group metals by use of selective solvent extraction techniques, in: Extraction Metallurgy '81, IMM*, London, **1981**.
- [11] M. Cox, *Solvent extraction in hydrometallurgy. Principles and Practices of Solvent Extraction*, Marcel Dekker, New York, **1992**.
- [12] J. Kramer, W. L. Driessen, K. R. Koch, J. Reedijk, *Hydrometallurgy* **2002**, 64, 59.
- [13] K. D. Topp, M. Grote, *Reactive & Functional Polymers* **1996**, 31, 117.
- [14] E. R. Els, L. Lorenzen, C. Aldrich, *Minerals Engineering* **2000**, 13, 401.
- [15] J. M. Sanchez, M. Hidalgo, V. Salvado, *Reactive & Functional Polymers* **2001**, 46, 283.
- [16] Y. Baba, H. Hiraakawa, Y. Kawano, *Chemistry Letters* **1994**, 117.
- [17] C. Kantipuly, S. Katragadda, A. Chow, H. D. Gesser, *Talanta* **1990**, 37, 491.
- [18] J. E. Huheey, E. A. Keiter, R. L. Keiter, *Inorganic Chemistry: Principles of Structure and Reactivity*, Fourth Edition, HarperCollins College Publishers, New York, **1993**.
- [19] E. Antico, A. Masana, V. Salvado, M. Hidalgo, M. Valiente, *Analytica Chimica Acta* **1994**, 296, 325.

- [20] J. Polakovicova, J. Medved, V. Stresko, J. Kubova, A. Celkova, *Analytica Chimica Acta* **1996**, 320, 145.
- [21] S. Siddhanta, H. R. Das, *Talanta* **1985**, 32, 457.
- [22] K. M. Dingman, K.M. Gloss, E. A. Milano, S. Siggia, *Analytical Chemistry* **1974**, 46, 145.
- [23] M. Grote, A. Kettrup, *Analytica Chimica Acta* **1985**, 175, 239.
- [24] M. Grote, A. Kettrup, *Analytica Chimica Acta* **1987**, 201, 95.
- [25] M. A. Congost, D. Salvatierra, G. Marques, J. L. Bourdelande, J. Font, M. Valiente, *Reactive & Functional Polymers* **1996**, 28, 191.
- [26] Y. B. Qu, *Analyst (Cambridge, United Kingdom)* **1996**, 121, 139.
- [27] L. L. Vatta, J. Kramer, K. R. Koch, *Separation Science and Technology* **2007**, 42, 1985.
- [28] J. Kramer, N. E. Dhladhla, K. R. Koch, *Separation and Purification Technology* **2006**, 49, 181.
- [29] R. X. Grimshaw, C. E. Harland, *Ion-exchange: Introduction to theory and practice*, London: Chemical Society, **1975**.
- [30] J. X. Khym, *Analytical Ion-exchange Procedures in Chemistry and Biology: Theory, Equipment, Techniques*, Prentice-Hall, Inc., Englewood Cliffs, New Jersey, **1974**.
- [31] J. A. Kitchener, *Ion-exchange resins*, Methuen, London, **1957**.
- [32] K. Dorfner, *Ion-exchangers: properties and applications*, 2 ed., Ann Arbor Science Publishers Inc., Michigan, U.S.A, **1973**.
- [33] I. Kobal, P. Hesleitner, E. Matijevic, *Colloids and Surfaces* **1988**, 33, 167.
- [34] H. Tamura, N. Katayama, R. Furuichi, *Journal of Colloid and Interface Science* **1997**, 195, 192.
- [35] H. Tamura, E. Matijevic, L. Meites, *Journal of Colloid and Interface Science* **1983**, 92, 303.
- [36] M. Todorovic, S. K. Milonjic, J. J. Comor, I. J. Gal, *Separation Science and Technology* **1992**, 27, 671.
- [37] L. L. Vatta, R. D. Sanderson, K. R. Koch, *Pure and Applied Chemistry* **2006**, 78, 1793.
- [38] L. L. Vatta, J. Kramer, K. R. Koch, *Separation Science and Technology* **2007**, 42, 1985.
- [39] J. Hu, I. M. C. Lo, G. Chen, *Water Science and Technology* **2004**, 50, 139.

- [40] M. M. Hyland, G. M. Bancroft, *Geochimica et Cosmochimica Acta* **1989**, 53, 367.
- [41] M. L. Machesky, W. O. Andrade, A. W. Rose, *Geochimica et Cosmochimica Acta* **1990**, 55, 769.
- [42] R. M. Cornell, U. Schwertmann, *The Iron Oxides: Structure, Properties, Reactions, Occurrences and Uses*, Wiley-VCH, Weinheim, **1996**.
- [43] G. F. Goya, T. S. Berquo, F. C. Fonseca, M. P. Morales, *Journal of Applied Physics* **2003**, 94, 3520.
- [44] Y. Koseoglu, H. Kavas, B. Aktas, *Physica Status Solidi A: Applications and Materials Science* **2006**, 203, 1595.
- [45] A. K. Gupta, M. Gupta, *Biomaterials* **2005**, 26, 3995.
- [46] A. G. Roca, J. F. Marco, M. d. P. Morales, C. J. Serna, *Journal of Physical Chemistry C* **2007**, 111, 18577.
- [47] G. P. Hatch, R. E. Stelter, *Journal of Magnetism and Magnetic Materials* **2001**, 225, 262.
- [48] M. Zborowski, *Scientific and Clinical Applications of Magnetic Carriers*, Plenum, New York, **1997**.
- [49] D. E. Speliotis, *Journal of Magnetism and Magnetic Materials* **1999**, 193, 29.
- [50] J. Philip, T. Jaykumar, P. Kalyanasundaram, B. Raj, *Measurement Science and Technology* **2003**, 14, 1289.
- [51] D. Chiba, M. Yamanouchi, F. Matsukura, H. Ohno, *Science (Washington, DC, United States)* **2003**, 301, 943.
- [52] T. Black, K. Raj, S. Tsuda, *Journal of Magnetism and Magnetic Materials* **2002**, 252, 39.
- [53] K. Raj, B. Moskowitz, R. Casciari, *Journal of Magnetism and Magnetic Materials* **1995**, 149, 174.
- [54] E. Blums, A. Cebers, M. M. Maiorov, *Magnetic fluids*, Berlin: De Gruyter, **1997**.
- [55] A. S. Lubbe, C. Alexiou, C. Bergemann, *Journal of Surgical Research* **2001**, 95, 200.
- [56] A. Tanimoto, *Microspheres, Microcapsules and Liposomes*, Citus Book, London, **2001**.
- [57] A.L Paul, G.R. Chandra, *Journal of Magnetism and Magnetic Materials* **2001**, 225, 301.
- [58] M. Mary, *Scientific and Clinical Applications of Magnetic Carriers*, Plenum Press, New York, **1997**.
- [59] K. J. Klabunde, *Nanoscale materials in Chemistry*, Wiley-Interscience, New York, **2007**.
- [60] M. Manchester, N. F. Steinmetz, *Viruses and Nanotechnology*, Berlin: Springer, **2008**.

- [61] R. S. Molday, D. MacKenzie, *Journal of Immunological Methods* **1982**, 52, 353.
- [62] C. H. Ahn, J. W. Choi, H. J. Cho, *In Encyclopedia of Nanoscience and Nanotechnology*, American Scientific Publishers, Stevenson Ranch, CA, **2004**.
- [63] R. M. Cornell, U. Schwertmann, *Iron Oxides in the Laboratory*, VCH Verlagsgesellschaft, Weinheim, Germany, **1991**.
- [64] J. P. Jakubovics, *Magnetism and Magnetic Materials*, Second ed., Cambridge University Press, Cambridge, **1994**.
- [65] B. D. Cullity, *Introduction to Magnetic Materials*, Addison-Wesley Publishing Company, San Francisco, CA, **1972**.
- [66] D. Craik, *Magnetism: Principles and Applications*, John Wiley and Sons Ltd, Chichester, **1995**.
- [67] H. Bonneman, K. S. Nagabhushana, *In Encyclopedia of Nanoscience and Nanotechnology, Vol. 1*, American Scientific Publishers, Stevenson Ranch, CA, **2004**.
- [68] D. L. Leslie-Pelecky, R. D. Rieke, *Chemistry of Materials* **1996**, 8, 1770.
- [69] M. A. Willard, L. K. Kurihara, E. E. Carpenter, S. Calvin, V. G. Harris, *In Encyclopedia of Nanoscience and Nanotechnology, Vol. 1*, Stevenson Ranch, CA, **2004**.
- [70] G. F. Goya, *Solid State Communications* **2004**, 130, 783.
- [71] A. M. Schmidt, *Journal of Magnetism and Magnetic Materials* **2005**, 289, 5.
- [72] J.-P. Jolivet, C. Froidefond, A. Pottier, C. Chaneac, S. Cassaignon, E. Tronc, P. Euzen, *Journal of Materials Chemistry* **2004**, 14, 3281.
- [73] P. A. Dresco, V. S. Zaitsev, R. J. Gambino, B. Chu, *Langmuir* **1999**, 15, 1945.
- [74] M. Mikhaylova, D. K. Kim, N. Bobrysheva, M. Osmolowsky, V. Semenov, T. Tsakalakos, M. Muhammed, *Langmuir* **2004**, 20, 2472.
- [75] K. Woo, J. Hong, S. Choi, H.-W. Lee, J.-P. Ahn, C. S. Kim, S. W. Lee, *Chemistry of Materials* **2004**, 16, 2814.
- [76] R. Vijayakumar, Y. Koltypin, I. Felner, A. Gedanken, *Materials Science & Engineering, A: Structural Materials: Properties, Microstructure and Processing* **2000**, A286, 101.
- [77] A. P. Alivisatos, M. L. Geier, I. Gur, *Science (Washington, DC, United States)* **2005**, 310, 462.
- [78] O. Tegus, E. Brick, K. H. J. Buschow, F. R. de Boer, *Nature (London, United Kingdom)* **2002**, 415, 150.

- [79] C. N. R. Rao, A. Muller, A. K. Cheetava, *The Chemistry of Nanomaterials, Vol. Vol. 1*, Wiley-VCH, Weinheim, Germany, **2004**.
- [80] R. Massart, V. Cabuil, *Journal de Chimie Physique et de Physico-Chimie Biologique* **1987**, *84*, 967.
- [81] L. Vayssieres, C. Chaneac, E. Tronc, J. P. Jolivet, *Journal of Colloid and Interface Science* **1998**, *205*, 205.
- [82] G. A. Van Ewijk, G. J. Vroege, A. P. Philipse, *Journal of Magnetism and Magnetic Materials* **1999**, *201*, 31.
- [83] N. Buske, H. Sonntag, T. Goetze, *Colloids and Surfaces* **1984**, *12*, 195.
- [84] Y. Lu, Y. Yin, B. T. Mayers, Y. Xia, *Nano Letters* **2002**, *2*, 183.
- [85] M. D. Butterworth, L. Illum, S. S. Davis, *Colloids and Surfaces, A: Physicochemical and Engineering Aspects* **2001**, *179*, 93.
- [86] X. B. Ding, Z. H. Sun, G. X. Wan, Y. Y. Jiang, *Reactive & Functional Polymers* **1998**, *38*, 11.
- [87] Q. Liu, Z. Xu, J. A. Finch, R. Egerton, *Chemistry of Materials* **1998**, *10*, 3936.
- [88] M. Klotz, A. Ayrat, C. Guizard, C. Menager, V. Cabuil, *Journal of Colloid and Interface Science* **1999**, *220*, 357.
- [89] R. K. Iler, *The Chemistry of Silica*, Wiley-Interscience, New York, **1979**.
- [90] M. Ma, Y. Zhang, W. Yu, H.-y. Shen, H.-q. Zhang, N. Gu, *Colloids and Surfaces, A: Physicochemical and Engineering Aspects* **2003**, *212*, 219.
- [91] F. C. Meldrum, B. R. Heywood, S. Mann, *Science (Washington, DC, United States)* **1992**, *257*, 522.
- [92] C. R. Vestal, Z. J. Zhang, *Nano Letters* **2003**, *3*, 1739.
- [93] G.-M. Chow, K. E. Gonsalves, Editors, *Nanotechnology: Molecularly Designed Materials. (Symposium held at the 210th National Meeting of the American Chemical Society, Chicago, Illinois, August 20-24, 1995.) [In: ACS Symp. Ser., 1996; 622]*, **1996**.
- [94] P. Tartaj, T. Gonzalez-Carreno, C. J. Serna, *Advanced Materials (Weinheim, Germany)* **2001**, *13*, 1620.
- [95] L. Zang, *Nanostruct. Mater.* **1997**, *9*, 185.
- [96] A. P. Philipse, M. P. B. van Bruggen, C. Pathmamanoharan, *Langmuir* **1994**, *10*, 92.
- [97] W. Stober, *Journal Colloid Interface Science* **1968**, *26*, 62.
- [98] H. Wang, H. Nakamura, K. Yao, H. Maeda, E. Abe, *Chemistry Letters* **2001**, 1168.

- [99] I. J. Bruce, J. Taylor, M. Todd, M. J. Davies, E. Borioni, C. Sangregorio, T. Sen, *Journal of Magnetism and Magnetic Materials* **2004**, 284, 145.
- [100] A. K. Gupta, M. Gupta, *Biomaterials* **2005**, 26, 3995.
- [101] J. Kramer, A. R. Garcia, W. L. Driessen, J. Reedijk, *Chemical Communications (Cambridge, United Kingdom)* **2001**, 2420.
- [102] A. A. Golub, A. I. Zubenko, B. V. Zhmud, *Journal of Colloid and Interface Science* **1996**, 179, 482.
- [103] P. Tartaj, M. P. Morales, T. Gonzalez-Carreno, S. Veintemillas-Verdaguer, C. J. Serna, *Journal of Magnetism and Magnetic Materials* **2005**, 290-291, 28.
- [104] D. K. Kim, Y. Zhang, W. Voit, K. V. Rao, M. Muhammed, *Journal of Magnetism and Magnetic Materials* **2001**, 225, 30.
- [105] L. Shen, P. E. Laibinis, T. A. Hatton, *Langmuir* **1999**, 15, 447.
- [106] T. Sugimoto, E. Matijevic, *Journal of Colloid and Interface Science* **1980**, 74, 227.
- [107] T. Fried, G. Shemer, G. Markovich, *Advanced Materials (Weinheim, Germany)* **2001**, 13, 1158.
- [108] Y. S. Kang, S. Risbud, J. F. Rabolt, P. Stroeve, *Chemistry of Materials* **1996**, 8, 2209.
- [109] W. Rasband, *In Image J: Image processing and analysis in Java* <http://rsb.info.nih.gov/ij/>, 2006.
- [110] H. P. Klug, L. E. Alexander, *X-Ray Diffraction Procedures for Polycrystalline and Amorphous Materials*, Wiley, New York, **1974**.
- [111] S. Lowell, J. E. Shields, *Powder Surface Area and Porosity*, Chapman and Hall, London, **1984**.
- [112] P. A. Webb, C. Orr, *Analytical Methods in Fine Particle Technology*, Micromeritics Instrument Corp., **1997**.
- [113] A. Warshawsky, M. M. B. Fieberg, P. Mihalik, T. G. Murphy, Y. B. Ras, *Separation and Purification Methods* **1980**, 9, 209.
- [114] J. L. Cortina, E. Meinhardt, O. Roijals, V. Marti, *Reactive & Functional Polymers* **1998**, 36, 149.
- [115] D. A. Skoog, D. M. West, F. J. Holler, S. R. Crouch, *Analytical Chemistry: An Introduction*, Seventh ed., Brooks/Cole publishers, **2000**.
- [116] F. Zhang, Z. Su, F. Wen, F. Li, *Colloid Polymer Science* **2008**, 286, 837.
- [117] *EVA 11 DIFFRAC^{plus} BASIC Evaluation Package: XRD processing*, 2006.

- [118] R. J. Hunter, *Zeta Potential in Colloid Science: Principles and Applications*, Academic Press, London, **1981**.
- [119] F. Montagne, O. Mondain-Monval, C. Pichot, H. Mozzanega, A. Elaissari, *Journal of Magnetism and Magnetic Materials* **2002**, *250*, 302.
- [120] K. Woo, J. Hong, J.-P. Ahn, *J. Magn. Magn. Mater.* **2005**, *293*, 177.
- [121] C. J. Brinker, G. W. Scherer, *Sol-Gel Science, the Physics and Chemistry of Sol-Gel Processing*, Academic Press, San Diego, **1990**.
- [122] D. L. Pavia, G. M. Lampman, G. S. Kriz, *Introduction to Spectroscopy*, 3rd edition ed., Harcourt College Publishers, New York, U.S.A, **2001**.
- [123] T. J. Daou, G. Pourroy, G. Rogez, *Chemistry Materials* **2006**, *18*, 4399.
- [124] W. Zhong, Y. Du, *Magnetic Liquids: Handbook of Nanophase and Nanostructured Materials, Vol. 4*, Kluwer Academic/Plenum, New York, **2002**.
- [125] G. Q. Lu, X. S. Zhao, *Nanoporous Materials: Science and Engineering, Vol. 4*, Imperial College Press, London, **2004**.
- [126] E. Guibal, A. Larkin, T. Vincent, J. M. Tobin, *Industrial & Engineering Chemistry Research* **1999**, *38*, 4011.
- [127] M. Ruiz, A. M. Sastre, E. Guibal, *Reactive & Functional Polymers* **2000**, *45*, 155.
- [128] E. Guibal, M. Ruiz, T. Vincent, A. Sastre, R. Navarro-Mendoza, *Separation Science and Technology* **2001**, *36*, 1017.
- [129] W. Ngeontae, W. Aeungmaitrepirom, T. Tuntulani, *Talanta* **2007**, *71*, 1075.
- [130] F. Veglio, F. Beolchini, *Hydrometallurgy* **1997**, *44*, 301.
- [131] Y.-C. Cheng, D.-H. Chen, *Gold Bulletin (London, United Kingdom)* **2006**, *39*, 98.
- [132] K. R. Hall, L. C. Eagleton, A. Acrivos, T. Vermeulen, *Industrial & Engineering Chemistry Fundamentals* **1966**, *5*, 212.
- [133] Z.-X. Sun, F.-W. Su, W. Forsling, P.-O. Samskog, *Journal of Colloid and Interface Science* **1998**, *197*, 151.
- [134] S. K. Milonjic, M. M. Kopečni, Z. E. Ilic, *Journal of Radioanalytical Chemistry* **1983**, *78*, 15.
- [135] M. Kosmulski, *Journal of Colloid and Interface Science* **2004**, *275*, 214.
- [136] I. Berrodier, F. Farges, M. Benedetti, M. Winterer, G. E. Brown, M. Deveughele, *Geochimica et Cosmochimica Acta* **2004**, *68*, 3019.

- [137] J. Enzweiler, I. Joeke, *Journal of Geochemical Exploration* **1991**, 40, 133.
- [138] J. A. Peck, C. D. Tait, B. I. Swanson, G. E. Brown, Jr., *Geochimica et Cosmochimica Acta* **1991**, 55, 671.
- [139] M. K. Chow, C. F. Zukoski, *Journal Colloid Interface Science* **1994**, 165, 97.

Supplementary section:

Section A1 – Elemental analysis calculations

Only one calculation each based on the first set of values given in *Tables 2 and 3 (Chapter Three, section 3.1.3.1)*. The ligand concentrations were based on the nitrogen content and the carbon and hydrogen contents were based on the results of the nitrogen content. All the other values as shown in *Table 2 and 3* were obtained with similar calculations.

From Table 2:

For material **(1)**, the first set of experimental values obtained: % N 1.03; % C 4.44; % H 3.21.

$$\% \text{ N} = 1.03 \times 10 = 10.3 \text{ mg / g material (1)}$$

$$\Rightarrow \text{Ligand concentration: } \left(\frac{10.3 \text{ mg}}{14.007 \text{ g / mol}} \right) / \text{g} = 0.74 \text{ mmol N / g material (1)}$$

$$\Rightarrow \text{Carbon content: } 0.74 \times 4 = (2.94 \text{ mmol C} \times 12.011 \text{ g/mol}) / \text{g} = 35.33 \text{ mg / g} = 3.53 \% \text{ C}$$

$$\Rightarrow \text{Hydrogen content: } 0.74 \times 11 = (8.14 \text{ mmol H} \times 1.0079 \text{ g/mol}) / \text{g} = 8.20 \text{ mg / g} = 0.82 \% \text{ H}$$

From Table 3:

For material **(2)**, the first set of experimental values obtained: % N 2.61; % C 6.84; % H 3.07.

$$\% \text{ N} = 2.61 \times 10 = 26.1 \text{ mg / g material (1)}$$

$$\Rightarrow \text{Ligand concentration: } \left(\frac{26.1 \text{ mg}}{14.007 \text{ g / mol}} \right) / (2 \times \text{g}) = 0.93 \text{ mmol N / g material (1)}$$

$$\Rightarrow \text{Carbon content: } 0.93 \times 6 = (5.59 \text{ mmol C} \times 12.011 \text{ g/mol}) / \text{g} = 67.14 \text{ mg / g} = 6.71 \% \text{ C}$$

$$\Rightarrow \text{Hydrogen content: } 0.93 \times 16 = (14.88 \text{ mmol H} \times 1.0079 \text{ g/mol}) / \text{g} = 15 \text{ mg / g} = 1.50 \% \text{ H}$$

Section A2 – Thermogravimetric analysis calculations

Material **(1)** is the monoamine functionalized silica-coated SPMNs and material **(2)** is the diamine functionalized silica-coated SPMNs. Approximately 5 mg of **(1)** and **(2)** were weighed before insertion into the sample compartment of the TGA instrument.

For material **(1)**, the total weight loss is 10 % (*Figure 12*). The molecular mass of the free amine ligand, 3-(trimethoxysilyl) propylamine (APTS) used for functionalization of the silica-coated SPMNs (FeSi nanoparticles) to yield **(1)**, is 179.29 g/mol. The exact mass of **(1)** used for the TGA experiment was 5.3 mg.

$$10 \% \text{ of } 5.3 \text{ mg} = 0.53 \text{ mg} \text{ (10 \% loss of the total mass of (1))}$$

If assumed that the weight loss is only due to the ligand bound to the surface of **(1)**, then:

$$\begin{aligned} \frac{0.53 \text{ mg}}{179.29 \text{ g/mol}} &= 0.0031 \text{ mmol} \\ \Rightarrow 0.0031 \text{ mmol} &\text{ is due to the loss of APTS} \\ \Rightarrow \frac{0.0031 \text{ mmol}}{0.0053 \text{ g}} &= 0.56 \text{ mmol/g (mmol APTS / g (1))} \end{aligned}$$

The density of APTS is 1.027 g/mL. An APTS volume of 0.017807 mL was used during the functionalization procedure of the silica-coated SPMNs (FeSi) to yield **(1)**.

$$\begin{aligned} \Rightarrow \text{mass APTS used} &= 1.027 \frac{\text{g}}{\text{mL}} \times 0.017807 \text{ mL} = 0.018287 \text{ g} \\ \Rightarrow \text{moles APTS initially used to functionalize FeSi} &= \frac{0.018287 \text{ g}}{179.29 \text{ g/mol}} = 0.102001 \text{ mmol} \end{aligned}$$

From the TGA data, we obtain a value of 0.56 mmol APTS per gram of material **(1)**. 50 mg silica-coated SPMNs was used for the surface functionalization (refer to *Chapter 2*).

$$\begin{aligned} \Rightarrow 0.56 \text{ mmol/g} \times 0.05 \text{ g} &= 0.028 \text{ mmol} \\ \Rightarrow 0.028 \text{ mmol} &\text{ APTS was functionalized on the surface of FeSi nanoparticles} \end{aligned}$$

$$\Rightarrow \% \text{ Functionalized} \approx \frac{0.028 \text{ mmol}}{0.102001 \text{ mmol}} \times 100 \approx 27.45\%$$

The same methodology was used for **(2)**. For material **(2)**, the total weight loss is 14 % (*Figure 12*). The molecular mass of the free amine ligand, N-[3-(trimethoxysilyl) propyl] ethylene-diamine (ED) used for functionalization of the silica-coated SPMNs (FeSi nanoparticles) to yield **(2)**, is 222.36 g/mol. The exact mass of **(2)** used for the TGA experiment was 5.5 mg.

$$14 \% \text{ of } 5.5 \text{ mg} = 0.77 \text{ mg (10 \% loss of the total mass of (1))}$$

If assumed that the weight loss is only due to the ligand bound to the surface of **(1)**, then:

$$\begin{aligned} \frac{0.77 \text{ mg}}{222.36 \text{ g/mol}} &= 0.0035 \text{ mmol} \\ \Rightarrow 0.0035 \text{ mmol} &\text{ is due to the loss of ED} \\ \Rightarrow \frac{0.0035 \text{ mmol}}{0.0055 \text{ g}} &= 0.63 \text{ mmol/g (mmol ED / g (2))} \end{aligned}$$

The density of ED is 1.028 g/mL. A volume of 0.02206 mL was used during the functionalization procedure of the silica-coated SPMNs (FeSi) to yield **(2)**.

$$\begin{aligned} \Rightarrow \text{mass ED used} &= 1.028 \frac{\text{g}}{\text{mL}} \times 0.02206 \text{ mL} = 0.0227 \text{ g} \\ \Rightarrow \text{moles ED initially used to functionalize FeSi} &= \frac{0.0227 \text{ g}}{222.36 \text{ g/mol}} = 0.1019 \text{ mmol} \end{aligned}$$

From the TGA data, we obtain a value of 0.63 mmol ED per gram of **(2)**. Also, 50 mg sample of the silica-coated SPMNs was used for the surface functionalization (refer to *Chapter 2*).

$$\begin{aligned} \Rightarrow 0.63 \text{ mmol/g} \times 0.05 \text{ g} &= 0.0315 \text{ mmol} \\ \Rightarrow 0.0315 \text{ mmol} &\text{ APTS} \\ \Rightarrow \% \text{ Functionalized} &\approx \frac{0.0315 \text{ mmol}}{0.1019 \text{ mmol}} \times 100 = 30.91\% \end{aligned}$$

Therefore, using this methodology, we found that 27.45 % APTS and 30.91 % ED is functionalized onto the surface of the silica-coated SPMNs.

Section A3 – Adsorption of $[AuCl_4]^-$ by unfunctionalized SPMNs

In these experiments (*Figures 24 and 25*), we started with initial stock solutions containing known concentrations of gold (as determined by ICP-AES) in the form of $[AuCl_4]^-$ in 0.5 M and 0.01 M HCl matrices. In the batch sorption experiments, 10 mL aliquots of the stock solutions are used as feed solutions for each individual experiment, hence each data point in *Figures 24 and 25 (a – d)* represents one sorption experiment.

- *Figure 24: Effect of contact time on the adsorption of $[AuCl_4]^-$ from 0.5 M HCl by SPMNs.* Initial $[AuCl_4]^-$ in stock solution was determined to be 20.5 mg/L. Therefore, the total amount of “available” $[AuCl_4]^-$ in each 10 mL of feed solution is:

$$\frac{20.5mg}{1000mL} \times \frac{10mL}{1} = 0.205mg [AuCl_4]^- \text{ in total}$$

or 205 μg $[AuCl_4]^-$ in total

From *Figure 24 (a)*, the rate of $[AuCl_4]^-$ removal from 0.5 M HCl was calculated as follows. The $[AuCl_4]^-$ is quantitatively removed in 180 minutes at a rate of about

$$\frac{205\mu g}{180 \text{ min}} \cong 1.14\mu g / \text{min}$$

Similarly, $[AuCl_4]^-$ was quantitatively removed as shown in *Figure 24 (b – d)* and the sorption rate was calculated as done above and the values are given in *Table 8*.

- *Figure 25: Effect of contact time on adsorption of $[AuCl_4]^-$ from 0.01 M HCl by SPMNs.* Initial $[AuCl_4]^-$ in stock solution was determined to be 20.1 mg/L. Therefore, the total amount of “available” $[AuCl_4]^-$ in each 10 mL of feed solution is:

$$\frac{20.1mg}{1000mL} \times \frac{10mL}{1} = 0.201mg [AuCl_4]^- \text{ in total}$$

or 201 μg $[AuCl_4]^-$ in total

From *Figure 25 (a)*, the total amount of “available” $[AuCl_4]^-$ removed from 0.01 M HCl using 10 mg samples is about ~ 42 %.

$\Rightarrow 201 \mu g [AuCl_4]^- \times 0.42 \cong 84.42 \mu g$ of “available” $[AuCl_4]^-$ removed.

⇒ ~ 84 μg of “available” [AuCl₄]⁻ removed in 120 minutes at a rate of about

$$\frac{84\mu\text{g}}{120\text{ min}} \cong 0.70\mu\text{g} / \text{min}$$

From *Figure 25 (b)*, the total amount of “available” [AuCl₄]⁻ removed from 0.01 M HCl using 30 mg samples is about ~ 94 %.

⇒ 201 μg [AuCl₄]⁻ × 0.94 ≅ 188.94 μg of “available” [AuCl₄]⁻ removed.

⇒ ~ 188 μg of “available” [AuCl₄]⁻ removed in 120 minutes at a rate of about

$$\frac{188\mu\text{g}}{120\text{ min}} \cong 1.57\mu\text{g} / \text{min}$$

From *Figure 25 (c)*, the total amount of “available” [AuCl₄]⁻ is quantitatively removed from 0.01 M HCl using 50 mg samples in 30 minutes at a rate of about

$$\frac{201\mu\text{g}}{30\text{ min}} \cong 6.7\mu\text{g} / \text{min}$$

From *Figure 25 (d)*, the total amount of “available” [AuCl₄]⁻ is quantitatively removed from 0.01 M HCl using 100 mg samples in 5 minutes at a rate of about

$$\frac{201\mu\text{g}}{5\text{ min}} \cong 40.2\mu\text{g} / \text{min}$$

The values obtained from *Figure 25 (a – d)* is summarized in *Table 9*.

Section A4 – The extent of iron dissolution

The aqueous solutions can play an important role on the dissolution of iron oxide materials.^[42] Magnetite usually dissolves faster than other iron oxides due to both Fe(II) and Fe(III) content in their crystal structure. Experiments were therefore designed to investigate the effect of various aqueous acidic solution conditions on the iron dissolution of the magnetite based nanoparticle materials. The amount of resin degradation over time caused by magnetite that dissolved as a result of the acidic content of the aqueous solutions in which the sorption batch experiments have been performed, were investigated. In this regard, the iron dissolution (as mass %) for magnetite (Fe_3O_4), silica-coated SPMNs (FeSi) and the amine-functionalized magnetite nanomaterials (FeSiAPTS and FeSiED), were studied to determine the robustness of these resin materials. A constant mass of the nano-sized materials were contacted for a certain amount of time with hydrochloric acid solutions consisting of concentrations ranging from 0.5 M – 3.0 M HCl and in the pH range 3 – 6. The supernatant were collected *via* magnetic sedimentation by applying an external magnetic field. The amount of iron in solution was detected by ICP-AES and using mass balance equations the amount of iron dissolution could be calculated. The results of these findings are given in *Figure 39* and a visual characterization showing the amount of iron dissolution (corresponding to this result) of only the Fe_3O_4 nanoparticles can be seen in *Scheme 14*.

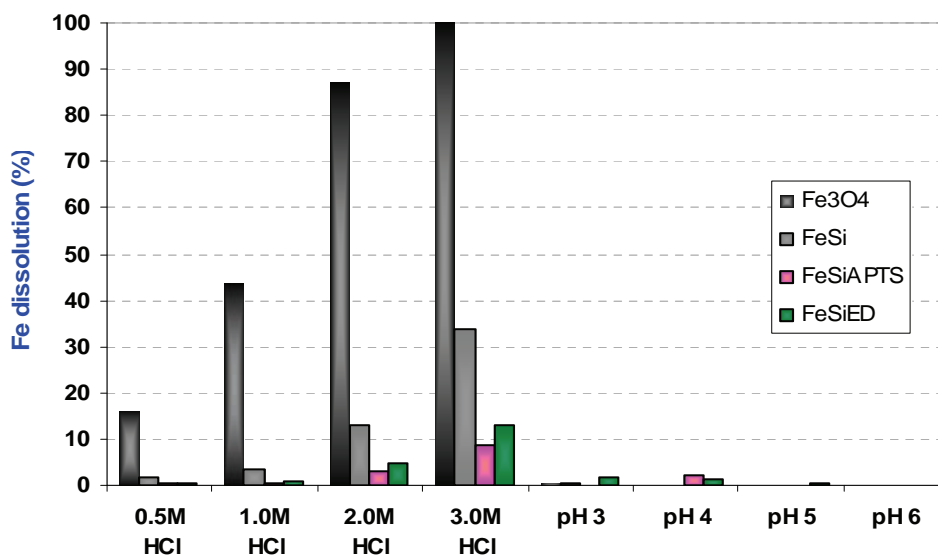
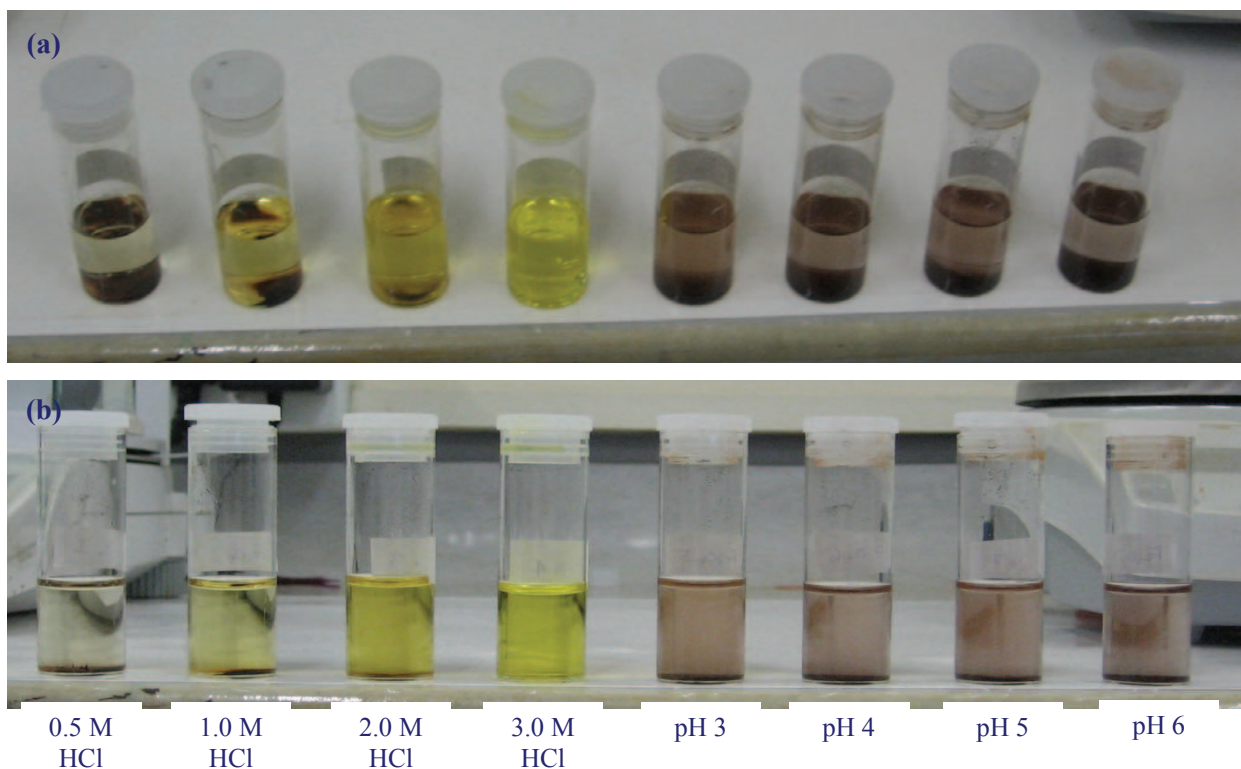


Figure 39. The amount of iron dissolution as a function of pH of the aqueous acidic solutions. Experimental conditions – mass material used: 50 mg; Total metal aqueous phase: 15 mL; Contact time: 150 minutes; Temperature: $21 \pm 1^\circ\text{C}$.

As can be seen in *Figure 39* and *Scheme 14*, there is an increase in iron dissolution as one proceeds from 0.5 M HCl to 3.0 M HCl. As expected, the highest percentage dissolution was found for bare magnetite as compared to the relatively low dissolution of the silica-coated amine-functionalized magnetite nanocomposite materials. In particular, for bare magnetite, *ca* 17 % dissolution occurred for the 0.5 M HCl solution experiments and 100 % dissolution was found for the 3.0 M HCl solution experiments. As indicated by the results obtained for the silica-coated magnetite nanoparticles, the silica layer indeed provides a protective layer against acidic conditions, with less than 2 % dissolution in the 0.5 M HCl solution experiments. However, a similar trend is observed, with increasing dissolution as the molarity of the solutions increases. To illustrate the protective mechanism that the silica layer offers, for the 3.0 M HCl solution experiment about 34 % dissolution was found to occur as compared to the 100 % dissolution for bare magnetite. Moreover, it was found that upon functionalizing the silica coated materials, the resistance against acidic conditions improved even more. Also, the iron dissolution of the materials was investigated in pH 3 – 6 ranges. In these studies, the amount of dissolution was almost negligible as shown in *Figure 39*.



Scheme 14. Visual illustration of the amount of iron dissolution for Fe_3O_4 nanoparticles in various acidic solutions corresponding to result in Fig. 39; (a) top view and (b) side view.